

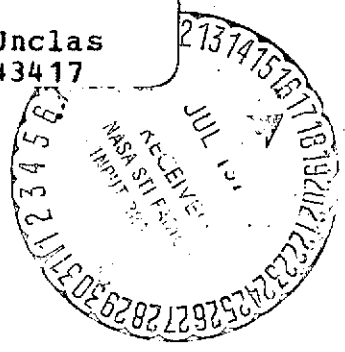
2-P (with X)

CR 137514

AVAILABLE TO THE PUBLIC

(NASA-CR-137514) DEVELOPMENT OF TRACE GAS DETECTION INSTRUMENTATION (Andros, Inc., Berkeley, Calif.) 99 p HC \$8.00 N74-27889

CSSL 14B G3/14 Unclass 43417



DEVELOPMENT OF TRACE GAS DETECTION INSTRUMENTATION

ARFR-24

April 1973

Distribution of this report is provided in the interest of information exchange. Responsibility for the contents resides in the organization that prepared it.

Reproduced by
**NATIONAL TECHNICAL
 INFORMATION SERVICE**
 U.S. Department of Commerce
 Springfield, VA. 22151

Prepared under Contract No. NAS2-6358 by

ANDROS INCORPORATED
 2332 Fourth Street
 Berkeley, California 94710

for

AMES RESEARCH CENTER
 NATIONAL AERONAUTICS AND SPACE ADMINISTRATION

N O T I C E

THIS DOCUMENT HAS BEEN REPRODUCED FROM THE BEST COPY FURNISHED US BY THE SPONSORING AGENCY. ALTHOUGH IT IS RECOGNIZED THAT CERTAIN PORTIONS ARE ILLEGIBLE, IT IS BEING RELEASED IN THE INTEREST OF MAKING AVAILABLE AS MUCH INFORMATION AS POSSIBLE.

ANDROS INCORPORATED

DEVELOPMENT OF TRACE GAS DETECTION INSTRUMENTATION

ARFR-24

April 1973

Distribution of this report is provided in the interest of information exchange. Responsibility for the contents resides in the organization that prepared it.

Prepared under Contract No. NAS2-6358 by

ANDROS INCORPORATED
2332 Fourth Street
Berkeley, California 94710

for

AMES RESEARCH CENTER
NATIONAL AERONAUTICS AND SPACE ADMINISTRATION

TABLE OF CONTENTS

<u>Section</u>	<u>Title</u>	<u>Page</u>
	PREFACE	
1	EXPERIMENTAL EVALUATION OF THE HETERODYNE PRINCIPLE	1-1
	1.1 Introduction	1-1
	1.2 Characteristics of Pressure Modulators	1-1
	1.3 Heterodyne Detection of CO ₂ and N ₂ O	1-8
2	CALIBRATION AND EVALUATION OF THE AMES HETERODYNE GAS ANALYZER	2-1
	2.1 Brief Description of the Ames Analyzer	2-1
	2.2 Debugging the Ames Analyzer	2-13
	2.3 Gas Measurements with the Prototype Analyzer	2-14
3	DESCRIPTION OF FINAL HARDWARE	3-1
	Introduction	3-1
	3.1 Low Noise Preamp	3-3
	3.2 Differential Line Receiver	3-3
	3.3 Low-Pass Filter (LPF)	3-6
	3.4 Range Amplifier	3-6
	3.5 ω - β PSD	3-10
	3.6 Analog Divider	3-19
	3.7 Output Filter	3-19
	3.8 ω PSD	3-23
	3.9 Modulator	3-23
	3.10 ω - β Synthesizer	3-27
	3.11 β Carrier Suppression Servo	3-30
	3.12 ω and β Reference Channel	3-32
	3.13	3-32
	3.14 Cooler Servo	3-32
	3.15 Filter Wheel Controller	3-35
	3.16 Power and Grounding	3-37
4	PERFORMANCE CHARACTERISTICS OF THE MULTIGAS ANALYZER	4-1
	4.1 Instrument Controls	4-1
	4.2 Gas Flow Rate	4-2
	4.3 Instrument Noise and Sensitivity	4-2
	4.4 Instrument Stability	4-9
	4.5 Rejection Ratios	4-9
APPENDICES		
A	HETERODYNE METHOD OF HIGH SPECIFICITY GAS DETECTION	
B	MINIATURE HELMHOLTZ RESONATOR STUDY	

TABLE OF CONTENTS (Cont'd)

List of Figures

Section	Figure	Title	Page
1	1.1	Schematic of resonator study arrangement	1-2
	1.2	Schematic of the two types of resonator cavities	1-4
	1.3	Configuration of the Standing Wave and Helmholtz resonators	1-6
	1.4	Experimental arrangement of initial heterodyne apparatus	1-9
	1.5	Variation of the N ₂ O rejection ratio of a heterodyne CO Analyzer with concentration of N ₂ O in the sample cell	1-14
	1.6	Envelopes of the absorption bands of CO and N ₂ O which shows the significant overlap	1-14
2	2.1	Optical System	2-2
	2.2	System Block Diagram	2-3
	2.3	Pressure Amplitude Control Circuit	2-4
	2.4	$\omega_1 - \omega_2$ Reference Signal Generator Circuit	2-5
	2.5	Phase Sensitive Detector Circuit	2-6
	2.6	Low Pass Filter Circuit	2-7
	2.7	Output Divider Circuit	2-8
	2.8	Thermoelectric Cooler Control Circuit	2-9
	2.9	0-180° Constant Amplitude Phase Shifter Circuit	2-10
	2.10	Constant Amplitude 90° Phase Shift Circuit	2-11
	2.11	Preamplifier Circuit	2-12

TABLE OF CONTENTS (Cont'd)

List of Figures

Section	Figure	Title	Page
3		System Block Diagram - Heterodyne Multigas Analyzer	3-2
	3.1	Low Noise Preamplifier	3-4
	3.2	Differential Line Receiver (ω - β) Signal Channel	3-5
	3.3	Low Pass Filter	3-7
	3.4a	Range Amplifier	3-8
	3.4b	(ω - β) Signal Channel	3-9
	3.5a	ω - β PSD	3-11
	3.5b	Simplified schematic, left half-stack, PSD (original configuration)	3-16
	3.6	Analog Divider	3-20
	3.7	Output Filter	3-21
	3.8	ω PSD	3-24
	3.9	Modulator	3-25
	3.10a	ω - β Synthesizer	3-28
	3.10b	ω - β Synthesizer	3-29
	3.11	β Carrier Suppression Servo	3-31
	3.12 3.13	ω and β Reference Channel	3-33
	3.14	Cooler Servo	3-34
	3.15	Filter Wheel Controller	3-36

TABLE OF CONTENTS (Cont'd)

List of Figures

Section	Figure	Title	Page
4	4.1	Flow rate vs flushing time	4-3
	4.2	Spectral frequency distribution of detector noise for black body source on and off	4-5
	4.3	Dependence of signal and noise on source voltage	4-6
	4.4	Dependence of signal and noise on driver voltage for CO and CO ₂	4-8
	4.5	Instrument zero stability and offsets	4-10
	4.6	Instrument span stability	4-11

List of Tables

Section	Table	Title	Page
1	1-1	Summary of Experimental Results for a Number of Resonator Configurations	1-5
	1-2	Summary of Basic Sensitivity and Rejection Ratios Obtained	1-11
2	2-1	Measured Transmission Efficiency of the Ames Prototype Analyzer	2-14
4	4-1	Rejection Ratios	4-13
	4-2	Filters Used in the Heterodyne Analyzer	4-15

PREFACE

The "heterodyne" method of high specificity trace gas analysis was first suggested by Mr. J. Dimeff of NASA, Ames Research Center. The principle encompasses the density modulation of a reference and a sample gas in two chambers sequentially spaced along an optical pathlength. The density modulation is accomplished at different frequencies, f_1 and f_2 , in the chambers. Means are provided to observe the absorption of a beam of infrared radiation which passes sequentially through both chambers to a radiation detector. Under contract NAS2-6358, Andros Incorporated performed experimental investigations to determine the working parameters of a "heterodyne" gas analyzer. At the conclusion of the contract, an experimental prototype three-gas (CO , CO_2 , CH_4) "heterodyne" infrared gas analyzer was constructed.

The work performed under contract NAS2-6358 fell into three naturally separable phases as follows:

PHASE I.

Andros constructed breadboard hardware to demonstrate detection of a gaseous species by the "heterodyne" principle. The characteristics of many of the component parts which had to be developed were investigated. Preliminary measurements were conducted which established the sensitivity and selectivity of this method of gas analysis for the gases CO , CO_2 and N_2O . After the conclusion of this phase, a prototype "heterodyne" gas analyzer was designed and built by NASA, Ames Research Center, personnel.

PHASE II.

The prototype heterodyne gas analyzer built by Ames Research was debugged and brought into operational condition. Performance parameters of the prototype analyzer were then explored

and its sensitivity to CO₂ was measured. At the conclusion of this phase it was apparent that a major redesign, based on the results of Phase I and Phase II would yield a "second generation" prototype instrument with substantially improved performance and flexibility.

PHASE III.

Further component development was undertaken in both the optical bench and the electronic processor of a heterodyne gas analyzer. A three-gas prototype analyzer, capable of measuring the gases CO, CO₂ and CH₄ was constructed and tested.

Detailed descriptions of the work conducted under Phases I, II, and III form Sections 1, 2 and 3 of this report. The final performance data obtained from the three-gas prototype heterodyne analyzer are presented in Section 4 of the report.

Appendix A consists of a technical paper on the heterodyne gas analysis principle which was presented at the AIAA Joint Conference on Sensing of Environmental Pollutants by Andros and Ames Research Center personnel. Appendix B summarizes the efforts devoted to the development of miniature Helmholtz resonators, a key component of a heterodyne analyzer. Although miniature resonators were not used in the final prototype analyzer constructed under the present contract, it is felt that they probably would be used if a commercial version of the instrument were developed, and so their development is included in this report in the interests of completeness and to provide guidance to others who may wish to make use of their properties.

1. EXPERIMENTAL EVALUATION OF THE HETERODYNE PRINCIPLE

1.1 Introduction

The initial phase of this contract was concerned with both investigating the feasibility of detecting trace quantities of gases using a pressure-modulated heterodyne technique, and the construction of certain crucial elements of an instrument that would employ this technique.

1.2 Characteristics of Pressure Modulators

It is possible to generate large pressure excursions using either of two distinct types of acoustical resonators. The most common type is the distributed resonator using open or closed tubes of uniform cross section. The second type of acoustical resonator is the lumped, or Helmholtz, resonator, in which gas surges back and forth through a connecting pipe or aperture between two volumes. An expression for the Helmholtz frequency, f_H , is

$$f_H = \frac{c}{2\pi} \left[\frac{S}{l} \left(\frac{1}{V_1} + \frac{1}{V_2} \right) \right]^{1/2}$$

where c is the velocity of sound, S and l are the areas and length of the connecting pipe, and V_1 and V_2 are the volumes at either end of the connecting pipe. Both types of resonating cavities have been investigated.

A limited initial effort was made to investigate the best geometry for producing acoustic resonances by using microphones as the pressure transducer. However, it quickly became apparent that unambiguous interpretation of the signals obtained is very difficult, due to microphonics and non-linear response of the pressure transducer as well as mechanical vibrations of the system. Therefore, pressure excursions in the initial experiments have been estimated by observing the modulation of black body radiation by an infrared active gas inside the resonating pressure system. Using this technique, the very effect sought (i.e., modulation of radiation) provides the method of estimating the gas pressure excursion.

The general experimental arrangement is shown in Figure 1.1.

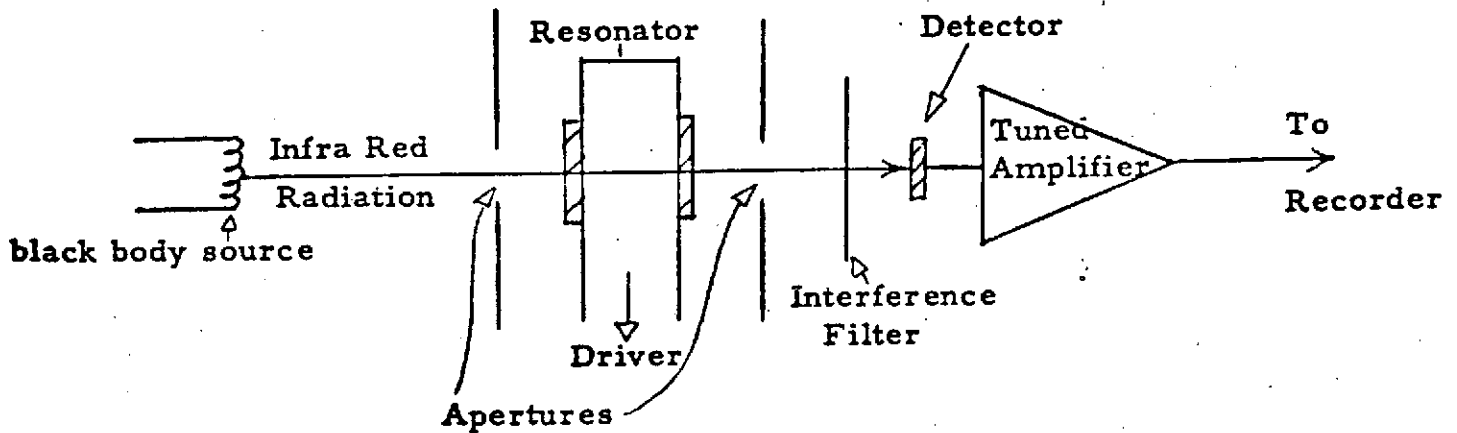


Figure 1.1. Schematic of resonator study arrangement.

Signals from the infrared detector have been observed at the driving frequency which may be ascribed to one or more of the following sources:

- a. Modulation of the absorption of black body radiation by the $4.3\mu\text{m}$ band of CO_2 .
- b. Temperature fluctuation of the vessel walls due to heat transfer to and from the gas (at the resonant frequency).
- c. Thermally induced emission of CO_2 at $4.3\mu\text{m}$.
- d. Microphonics of the detector.
- e. Modulation of the transmitted radiation in both resonators by its reflection from mechanically vibrating surfaces and beam-defining apertures.
- f. Detector noise.
- g. Pressure modulation due to wide-band noise of the driver power supply.

It was expected that signals arising from sources (b) and (c) will not present problems at the heterodyne (side band) frequencies of an actual gas analyzer. All experiments performed used a driver designed

for use with horns. Among the advantages of this source of audio power as against other types are that they a) are designed to operate at high input electrical power levels, b) have a compact size, c) produce the largest sound level intensities, and d) are contained in a housing which is convenient for incorporating into an experimental system.

These initial experiments used the University Sound driver type ID-60 (capable of consuming 60 W of power) as the source of acoustic energy and either pure CO_2 or 1/4% CO_2 mixture in N_2 as the gas filling. Carbon dioxide was used rather than CO for these investigations because more care would be required in the construction of the test systems if CO were used due to the toxic nature of CO. Approximate values for the change in absorbing thickness for unit change in pressure have been derived as a function of the mean absorbing thickness, from the curves of growth for CO_2 (neglecting temperature variation of the gas) and used to estimate the pressure fluctuation from the modulated infrared signal. In all calculations, the absorption of radiation by CO_2 in the air has not been included. While the error this contributes to any particular measurement may not be negligible, it is expected that the calibration technique used reduced this error to a second order effect and, in any case, should not affect the use of the results of the calculations to determine the relative performance of the various resonators examined.

The general shape of the Standing Wave and Helmholtz resonators used are shown in Figure 1.2.

A summary of the experimental results obtained so far for a number of resonator configurations is given in Table 1.1

As a figure of merit for comparing resonators, the percentage pressure fluctuation at one atmosphere mean pressure per watt of ohmic power loss in the coil at the resonant frequency is included in the table. For a mixture of 1/4% CO_2 in N_2 , the highest figure

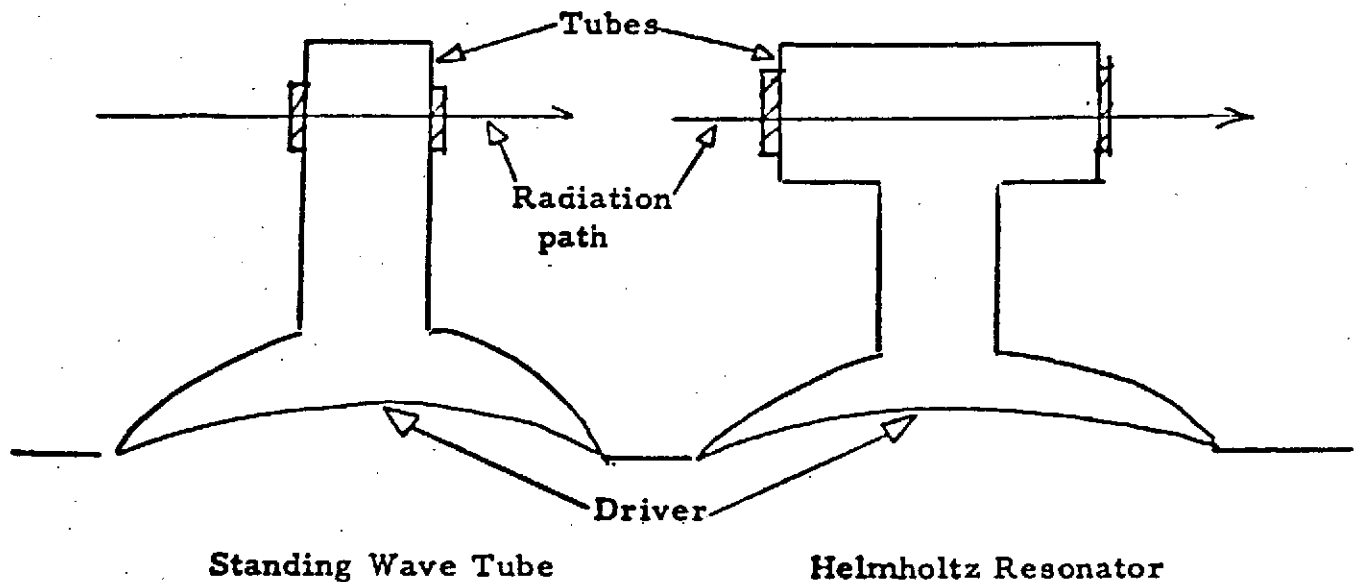


Figure 1.2. Schematic of the two types of resonator cavities.

of merit obtained to date is 2.2% of an atmosphere per watt dissipation with the Mk II Helmholtz resonator for which the pressure excursion for a total input power of 14 watts is estimated to be about 10% of an atmosphere. It is unlikely that the pressure fluctuation derived deviates from the correct value by more than a factor of 2. The value listed for the Q of each system has been derived from the shape of the graph of modulated signal vs. frequency. The resonator configurations used to obtain the results of Table 1.1 are shown diagrammatically in Figure 1.3.

In the following paragraphs, a brief account of the various unwanted signals is given:

A signal at the driving frequency is observed when CO_2 is present in the resonator and no black body radiation is incident on the resonator. If this modulation were all thermally induced emission, then for a gas filling of 1/4% CO_2 and N_2 , the magnitude of this emission would be about 10% of the modulated absorption black body signal (for the same pressure excursion). However,

TABLE 1.1

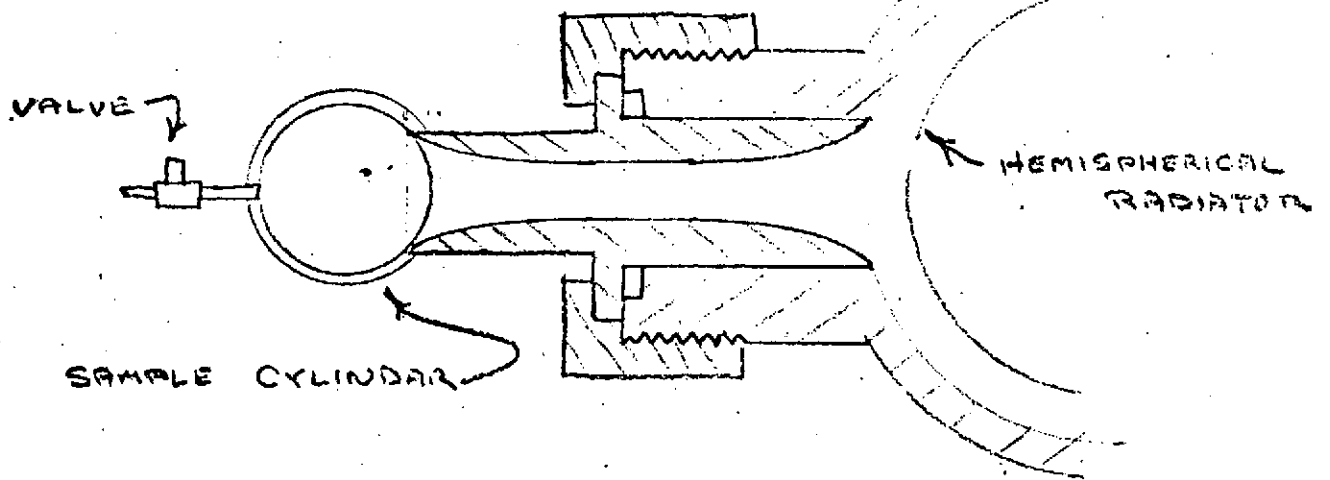
SUMMARY OF EXPERIMENTAL RESULTS FOR
A NUMBER OF RESONATOR CONFIGURATIONS

	Standing Wave Tube	Helmholtz Resonator		Units
	MkI	MkI	MkII	
Frequency for max. modulation of radiation	1890	350	550	Hertz
Input power	11	17	14	watts
Ohmic power loss	3.7	11	4.5	watts
% of CO ₂ in gas sample	1/4%	1/4%	1/4%	Remainder is N ₂
Absorption path length in resonator	2	2.4	2.4	cms
$\frac{\text{Peak modulated signal}}{\text{DC black body signal}}$	$\frac{1}{200}$	$\frac{1}{250}$	$\frac{1}{120}$	--
*Estimated Pressure fluctuation (p-p value)	7%	5%	10%	%
$\frac{\% \text{ Pressure fluctuation}}{\text{Ohmic power loss}}$	1.9	0.5	2.2	% atmosphere per watt
[**Q	30	10	5	--]

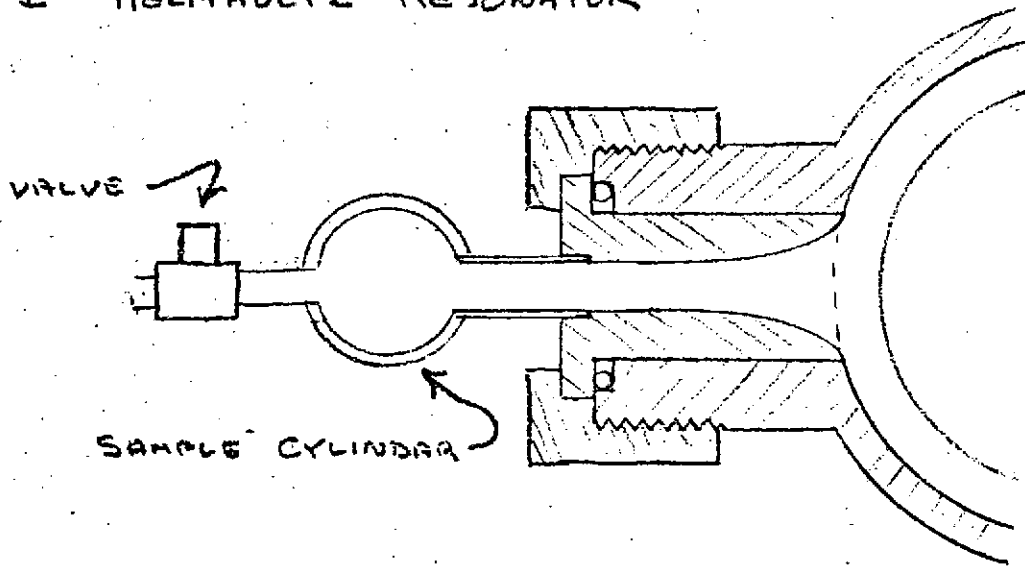
* This is probably correct to within a factor of 2.

** Definition following Terman, Radio Engineering, p. 41. (See text.)

MARK II HELMHOLTZ RESONATOR



MARK I HELMHOLTZ RESONATOR



MARK I STANDING WAVE TUBE

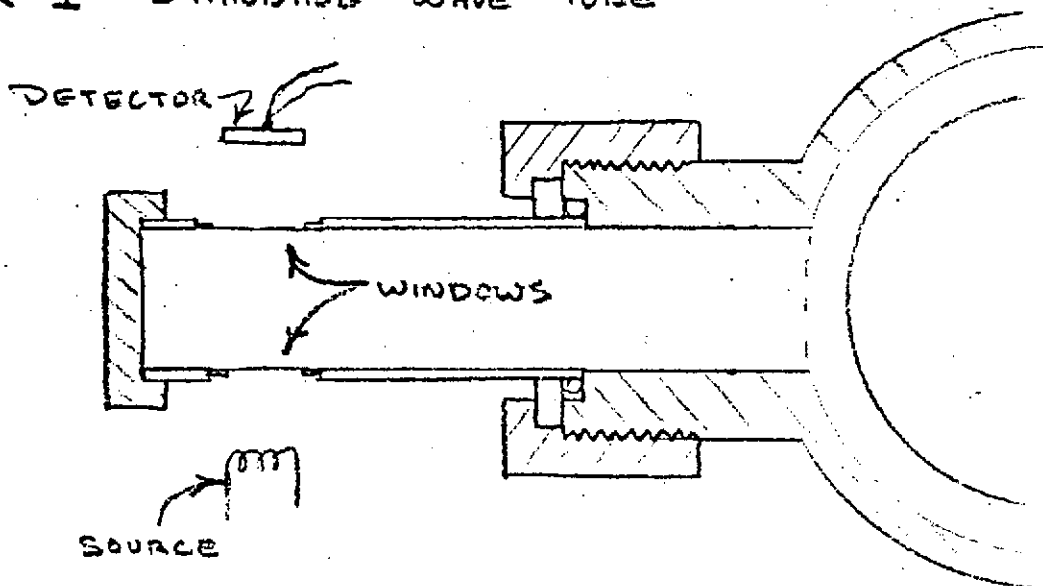


Figure 1.3. Configuration of the Standing Wave and Helmholtz resonators.

some of this apparent thermally induced emission signal is not due to CO_2 since a signal (though much smaller) is also observed using interference filters centered on other gases (4.6 and $5.3\mu\text{m}$). Impurities contributed by the gas handling system as well as non-metallic materials in the construction of the driver might account for the apparent thermally induced emission observed at the wavelengths other than CO_2 . It is interesting to note that the modulation of black body radiation by CO_2 and the effects ascribed to thermally induced emission are quite clearly of opposite phase-- which is consistent with the explanation proposed.

When pure N_2 is used in the resonator and no black body radiation is incident on the resonator, a signal is still observed at the driving frequency whose dependence on the frequency is similar to that of CO_2 . However, the magnitude of this signal is small compared with that observed when CO_2 is present. This signal is observed at wavelengths other than the $4.3\mu\text{m}$ band of CO_2 . There are at least two possible processes contributing to the signal:

- a. Thermally induced emission of infrared active gas impurities.
- b. A more likely cause, however, is suggested by a calculation which indicates that a signal could arise from changes of the black body emission of the walls of the resonator as the temperature of the vessel attempts to follow the pressure induced gas temperature variations. (Note that a 10% pressure change in N_2 is accompanied by about a 10°C temperature change.)

By modifying the geometry so as to prevent the detector from seeing the metal walls of the resonator, the observed signal (which can be as large as 10% of the CO_2 absorption modulation) is drastically reduced.

A small microphonic signal due to vibratory motion of the cavity walls and the detector itself is also observed. The magnitude of this signal can be substantially reduced by using a rigid optical structure and by taking steps to prevent the direct reflection of black body radiation from vibrating surfaces.

1.3 Heterodyne Detection of CO₂ and N₂O

Initial studies of the detection of CO₂ at the heterodyne frequencies were first observed using a liquid nitrogen-cooled indium antimonide detector. Using a 5 cm long sample cell and 10 second integration time, low concentrations of CO₂ (for example 10 - 20 ppm) were measured with an RMS noise level of approximately 0.3 ppm.

A schematic diagram of the experimental arrangement is shown in Figure 1.4. The average total pressure in both gas cells is 1 atmosphere, with CO₂ being the infrared active gas studied and N₂ providing the balance of pressure. The optimum partial pressure of CO₂ in the reference cell to produce highest sensitivity has been found experimentally to be about 4% of an atmosphere (i.e., an absorption path length of 0.1 atm cm). Low partial pressures of CO₂ are introduced into the 5 cm long sample cell. Typical driving frequencies of the reference and sample cells are 500 and 800 hertz respectively. Modulated black body signals at both driving frequencies and sideband frequencies are amplified and then passed through a high pass filter to reduce the very large (e.g., 2 volt p-p) reference cell signal while only slightly attenuating the 1300 hertz heterodyne signal. A permanent record of the wave analyzer output is obtained by plotting its output on a chart recorder. University Sound ID-60 drivers were used as the source of acoustic energy.

Contributions to the signal at the heterodyne frequency have been identified corresponding to the following sources:

- a. Absorption of radiation by CO₂ in both cells (i.e., the desired signal).

- b. Reflection of radiation from the vibrating walls of the gas cells.
- c. Noise present in the reference driving voltage at high power levels resulted in the presence of pressure waves at the heterodyne frequency and hence direct modulation of the black body radiation at this frequency by the CO₂ in this cell.
- d. Noise in the infrared radiation detector.
- e. The local oscillator in the wave-analyzer beats with the heterodyne frequency signal resulting in an output whose magnitude oscillates about the true value.

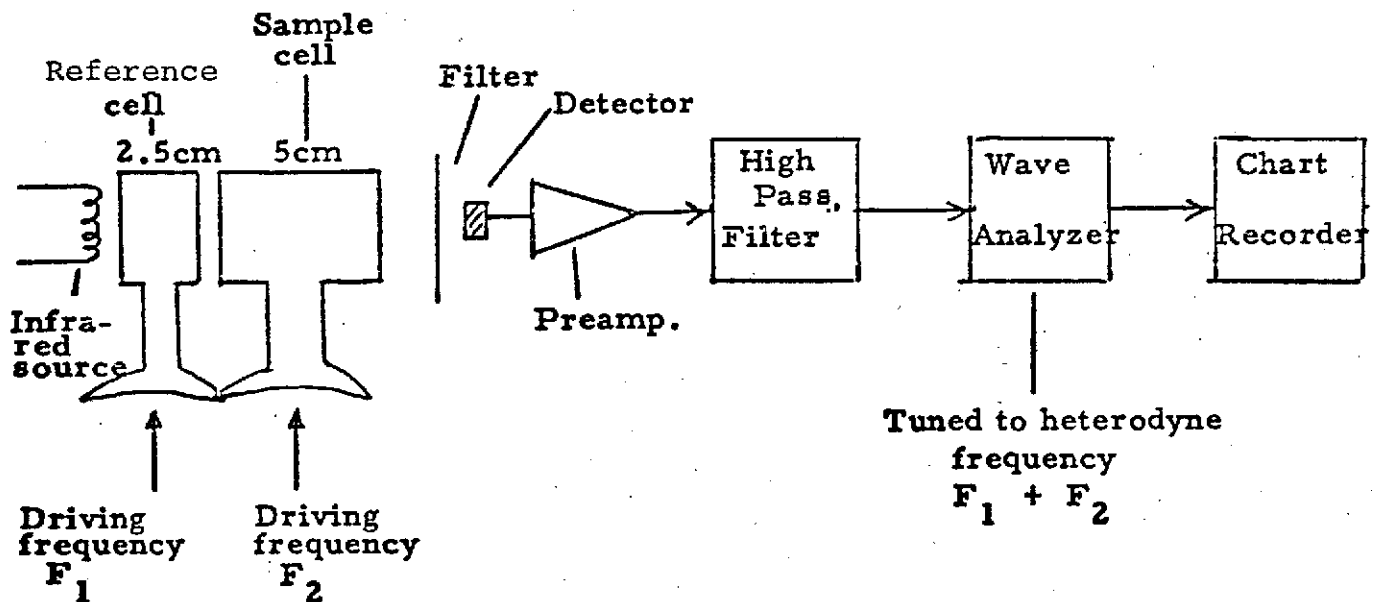


Figure 1.4. Experimental arrangement of initial heterodyne apparatus.

The reflection signal, (b), is out of phase with the CO₂ absorption heterodyne signal. Hence if a coherent detector were used, the effect of this signal would be to depress the zero ppm of CO₂ level. However, experience suggests that it is possible to reduce this source of systematic error until it is no longer significant by using high Q gas resonators and careful mechanical arrangement.

The heterodyne signal source, (c), can be removed by using a high Q gas resonator and its associated lower input power requirements.

Finally, the use of phase sensitive detection techniques whose reference is derived from pressure transducers in the gas resonators will eliminate the beat character (e) of the heterodyne signal.

Subsequent studies using a thermoelectrically cooled PbSe detector and an optical system specifically designed to reduce mechanical vibration, produced threshold sensitivities for CO₂, CO and N₂O of 0.2, 4 and 0.4 ppm respectively. In addition, lower limits to the cross-sensitivity of each of these gases for the other 2 gases have been established, as well as verifying that large improvements in the rejection ratio can be gained with the use of negative gas filters, for the case where a given pair of gases have strong interfering absorption bands.

A summary of the results is given in Table 1.2.

The experimental conditions under which these results have been obtained are:

- a. 2 cm long sample and chopper cells.
- b. Total pressure excursions of 20% atm and 30% atm in the sample and reference cells respectively.
- c. Operation of the black body source (a cigarette lighter) at a power level of less than a quarter of the maximum at which it can be operated.
- d. High pass and band pass filters have been used to reduce the signals generated at the fundamental and third harmonics of the modulating frequencies, to within the dynamic range of the Quantec RMS voltmeter that is used to measure the heterodyne signal.

TABLE 1.2

SUMMARY OF BASIC SENSITIVITY
AND REJECTION RATIOS OBTAINED

Gas	**Threshold Sensitivity	Gas filter	Rejection Ratios (lower Limit)	
			CO	N ₂ O
CO ₂	0.2 ppm	--	>500*:1	>500*:1
	0.2 ppm	1 atm cm of CO	>1500*:1 (Probably >15,000:1	--
	0.2 ppm	1 atm cm of N ₂ O	--	>15,000:1
CO	4 ppm	--	N ₂ O	CO ₂
		--	15:1 for 2% N ₂ O 2.5:1 for 0.04%	
	7 ppm	1 atm cm of N ₂ O	70:1 for 2% 50:1 for 0.04%	-- --
	4 ppm	1 atm cm of CO ₂	--	>5,000*:1
N ₂ O***	0.4 ppm	--	CO	CO ₂
		1 atm cm of CO	50:1* for 0.12% CO >500*:1 for 0.12% CO	--
	0.4 ppm	1 atm cm of CO ₂	--	>5,000*:1

* These values actually represent heterodyning of the radiation in the detector and preamplifier due to their non-linearities.

** Threshold sensitivity is here defined as the number of ppm of gas which produces a heterodyne signal equal to the RMS value of the variation of the detector/preamplifier's noise, at the heterodyne frequency.

*** Note that the filter used in these measurements transmits only one branch of N₂O

- e. An integrating time constant of 10 seconds has been used in the determination of threshold sensitivity.
- f. Measurements were performed at the sum heterodyne frequency since the detector noise is a factor of 3 less at the sum than at the difference frequency.

A serious limitation of the apparatus used has been found to be non-linearity of the thermoelectrically cooled PbSe detector and its preamplifier (Andros design). For example, this non-linearity results in a large heterodyne signal when the sample and reference cells are filled with CO₂ and N₂O, respectively (since both these gases produce large modulation of the infrared radiation), which corresponds to an apparent rejection ratio of 500:1, when, in fact, the absorption spectra of these two gases near 4.3 μ m have only a very small overlap and the rejection ratio must be quite large. This emphasizes the need to have extremely linear data handling electronics if an instrument is to be insensitive to the presence of large quantities of gases having absorption bands within the pass band of the interference filter. This problem is more acute in an instrument which is designed to measure simultaneously the concentration of a number of gases, because of the much wider pass band required by the interference filter.

A related problem is the large decrease in responsivity of the present detector as the light flux is increased. For example, by raising the temperature of the black body source above that currently used, the radiation intensity can be raised fourfold. However, with the present detector biasing arrangement, the responsivity drops by about a factor of four, and the detector becomes considerably more non-linear. Hence the present measurements have been performed at a reduced incident flux level.

Experimental results for the cross sensitivity of N₂O with CO are shown in Figure 1.5. These results were taken with the apparatus shown diagrammatically in Figure 1.4. The N₂O rejection ratio of a CO analyzer is a strong function of the total N₂O

concentration in the sample cell. This is a case of strongly overlapping absorption bands where the use of negative gas filtering can substantially increase a rejection ratio. Figure 1.6 illustrates the CO, N₂O band overlap.

Some attention was given to the possibility that signals at frequencies other than the simple heterodyne frequencies $f_1 \pm f_2$ may also be of interest; for should the cross-sensitivity dependence of these signals differ significantly from that of the $f_1 \pm f_2$ signals, it may be possible to use this information to correct the error contribution produced by other gases to the $f_1 \pm f_2$ signals. In particular, the ratio of second-to-first harmonics of the reference frequency of the modulated infrared radiation signal may be related to the rejection ratio. However, attempts to investigate this correlation were inconclusive due to the presence of second harmonic distortion in the acoustic drivers.

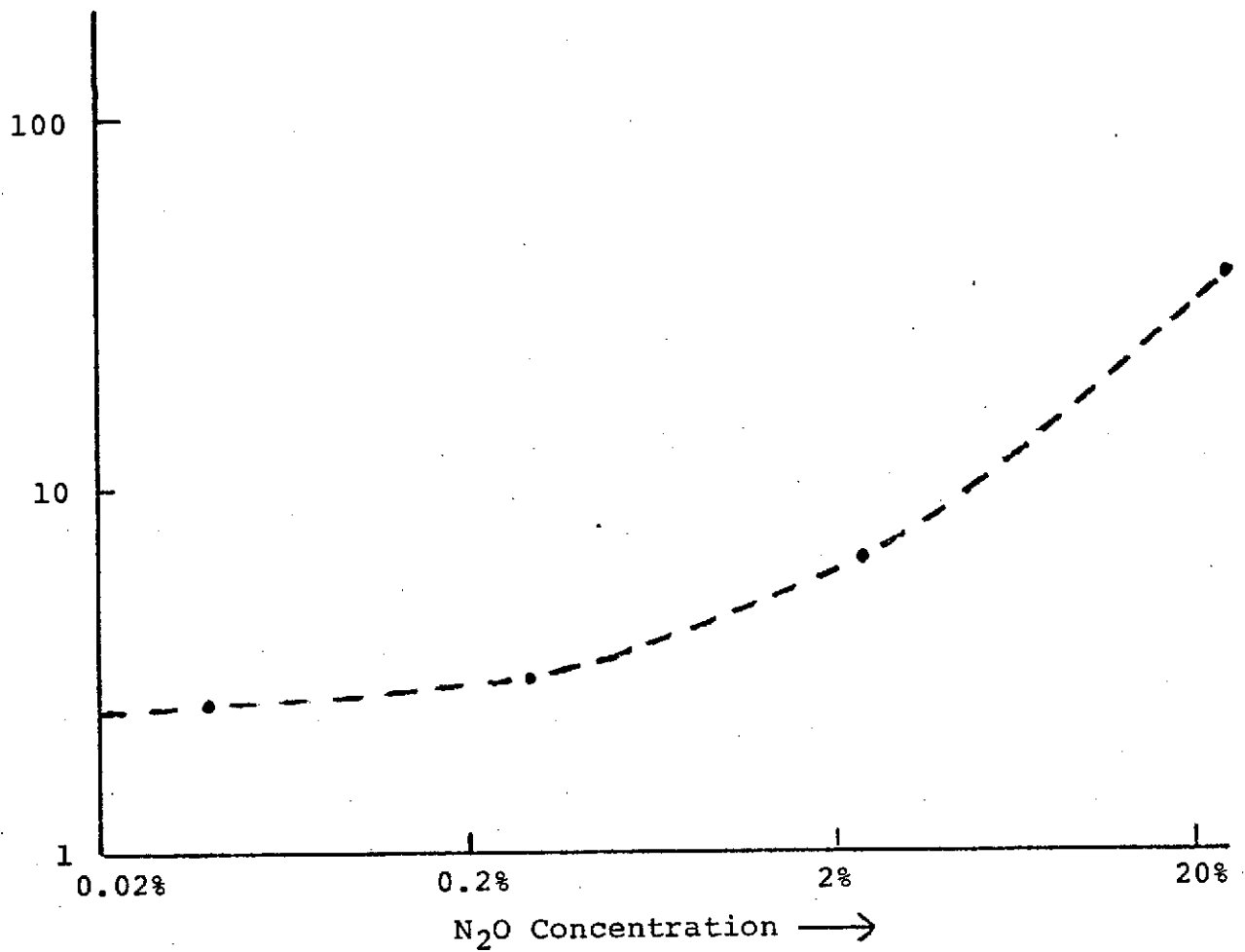


Figure 1.5. Variation of the N₂O rejection ratio of a heterodyne CO Analyzer with concentration of N₂O in the sample cell.

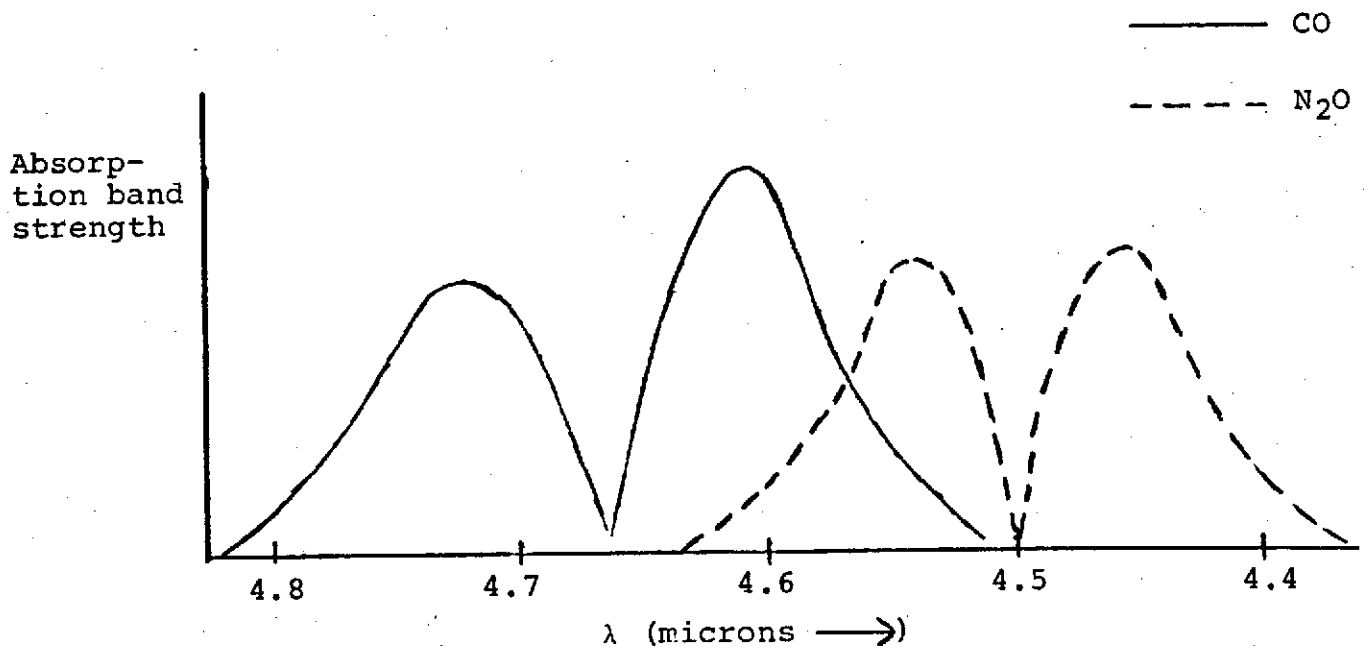


Figure 1.6. Envelopes of the absorption bands of CO and N₂O which shows the significant overlap.

2 CALIBRATION AND EVALUATION OF THE AMES HETERODYNE GAS ANALYZER

2.1 Brief Description of the Ames Analyzer

The prototype heterodyne gas analyzer supplied to Andros by Ames Research Center is shown diagrammatically in Figure 2.1. A block diagram of the electronic circuitry of the analyzer is shown in Figure 2.2. Individual blocks of the processing electronics are shown in Figures 2.3 through 2.11. A complete description of the instrument is included in Appendix A of this report, "Heterodyne Method for High Specificity Gas Detection" presented to the AIAA Joint Conference on the Sensing of Environmental Pollutants.

Three basic changes over the preliminary design study breadboard instrument described in Chapter 1 were considered desirable and were incorporated into the Ames prototype instrument. First, the optical system was modified to incorporate a 10 cm sample cell (five times as long as in the breadboard). The optical system shown in Figure 2.1 also conveniently provides for several static absorption cells to be placed in the beam; such cells can be used as filters to eliminate undesirable sensitivity to unwanted gases in special cases.

The second basic modification was an improvement on the acoustic driver-Helmholtz resonator design which permitted a greater fractional gas density modulation combined with "selfturning" of the driver to the Helmholtz resonant frequency.

Thirdly, the electronic system was designed and constructed to provide phase-sensitive detection of the signal at the heterodyne frequency. The reference signal for the phase-sensitive detector was derived from (and locked to) the variable difference between the drive frequencies of the sample and reference cell modulators.

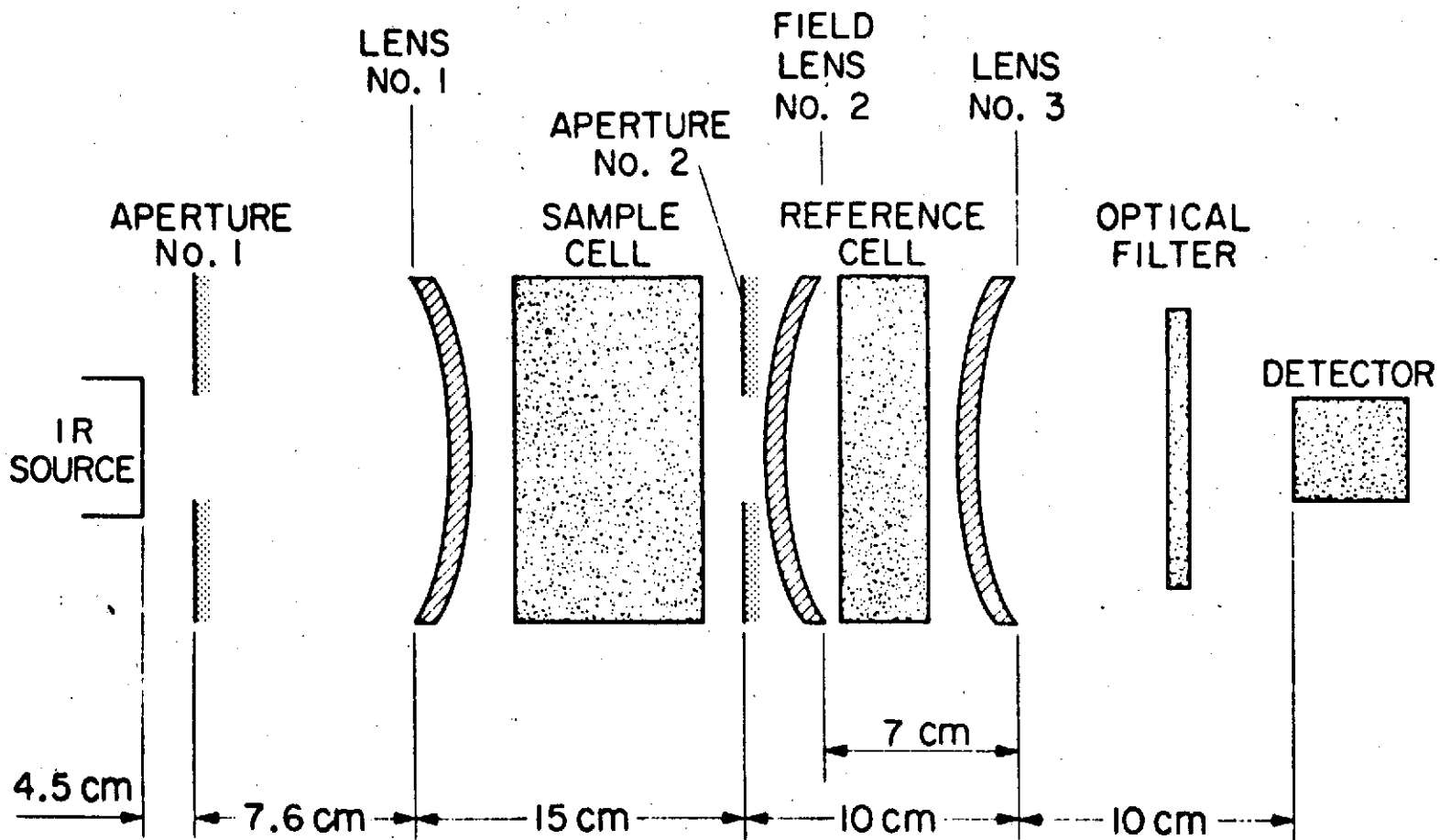


Figure 2.1. Optical System

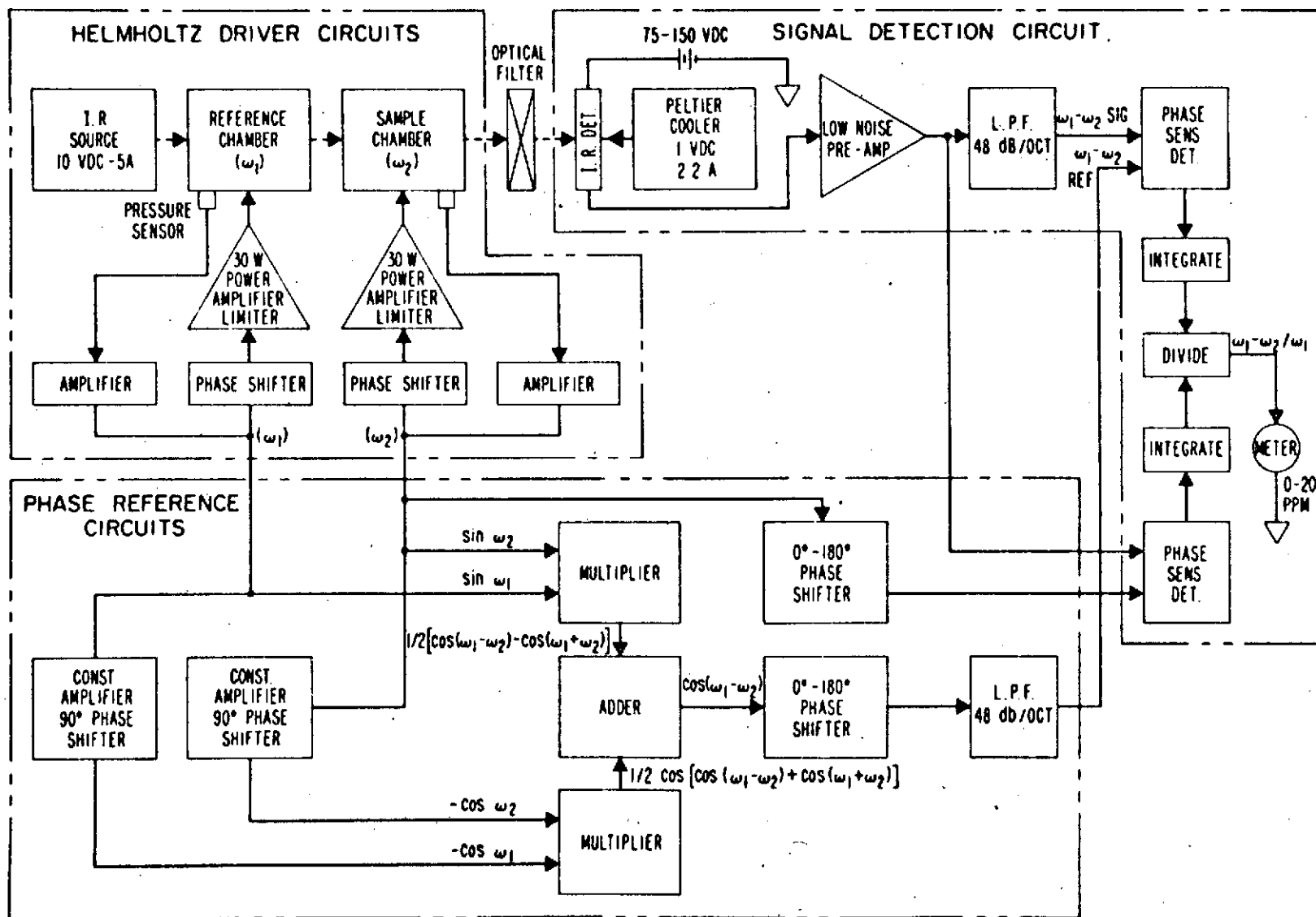


Figure 2.2. System Block Diagram

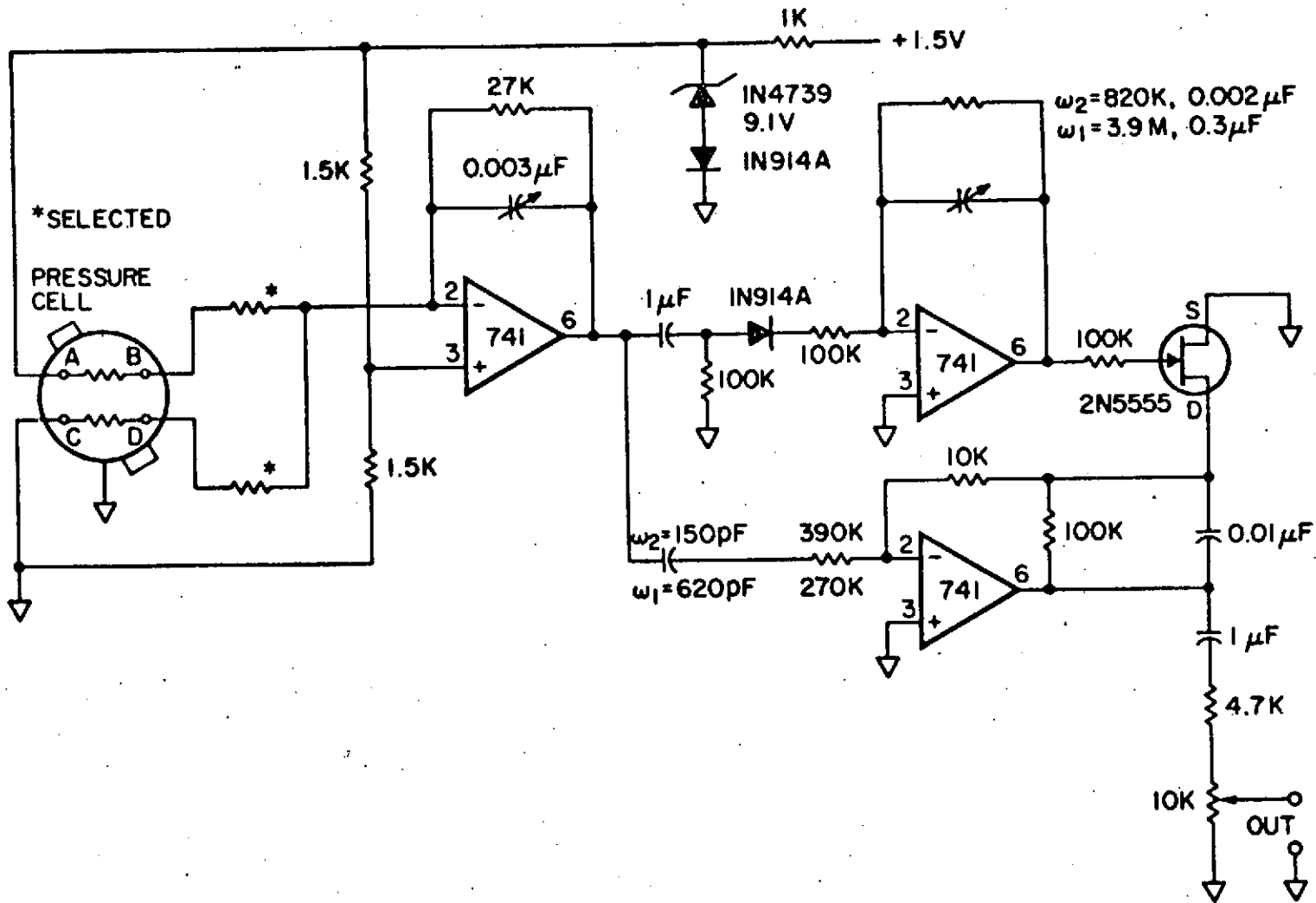


Figure 2.3. Pressure Amplitude Control Circuit

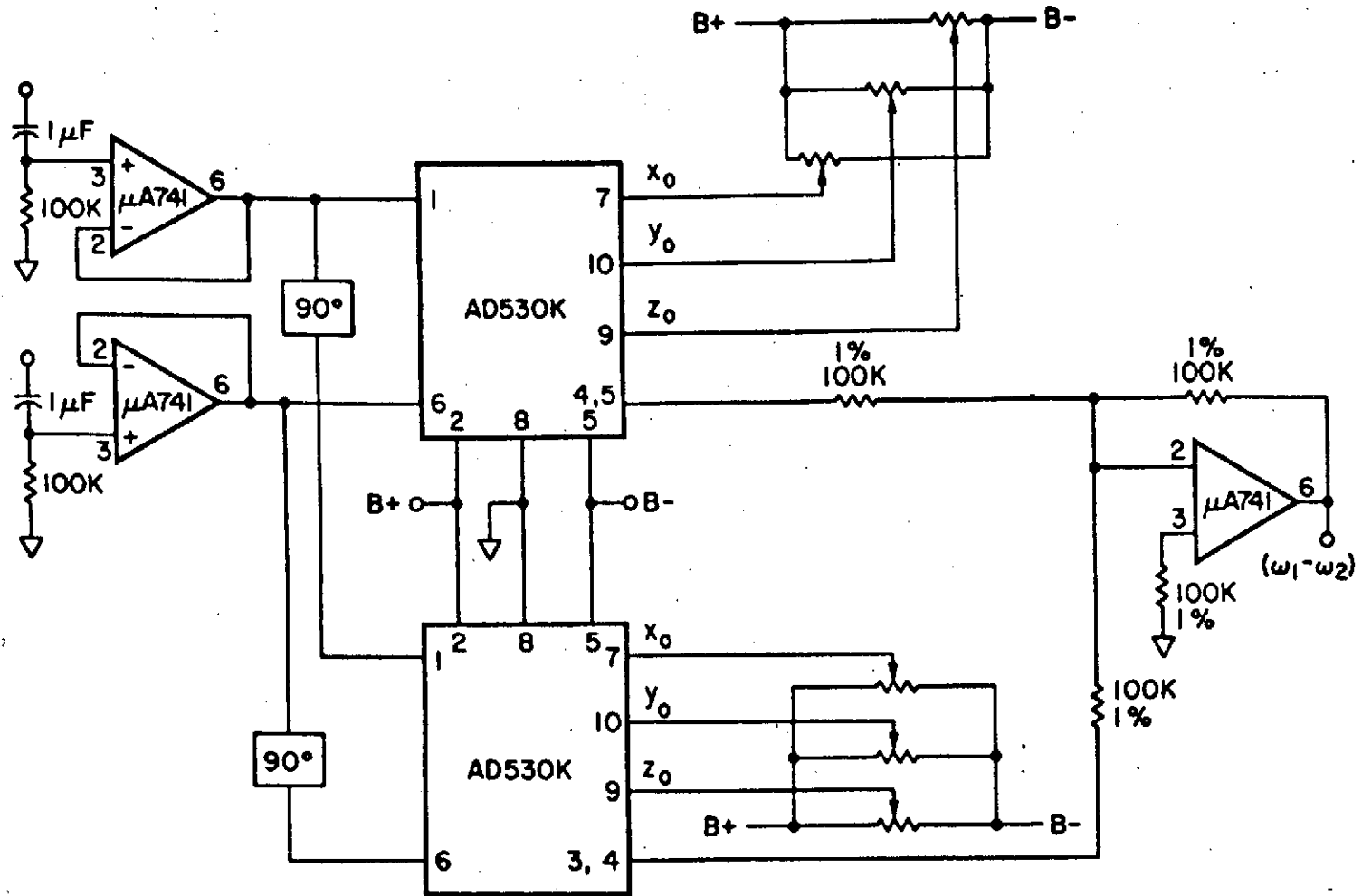


Figure 2.4. $\omega_1 - \omega_2$ Reference Signal Generator Circuit

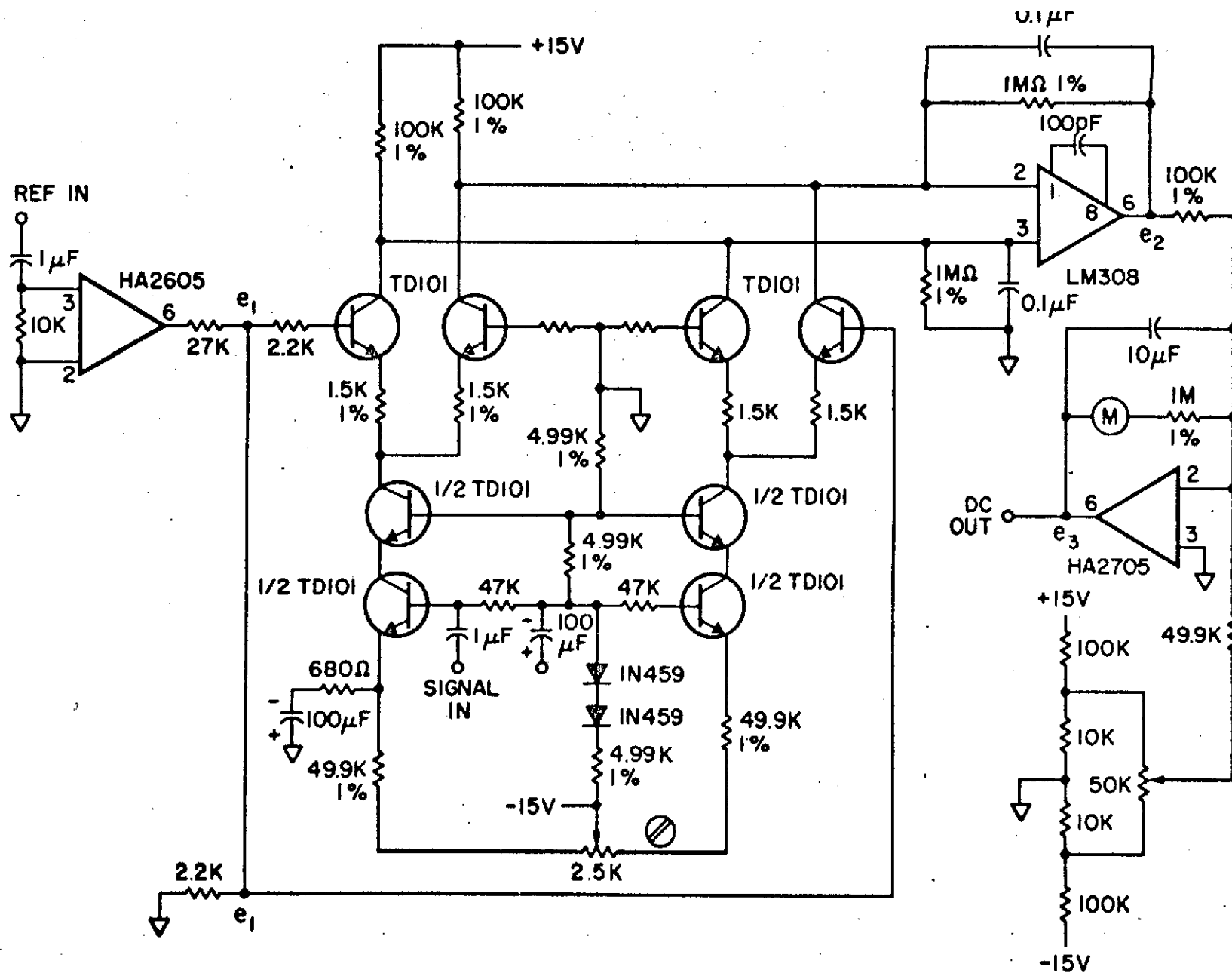


Figure 2.5. Phase Sensitive Detector Circuit

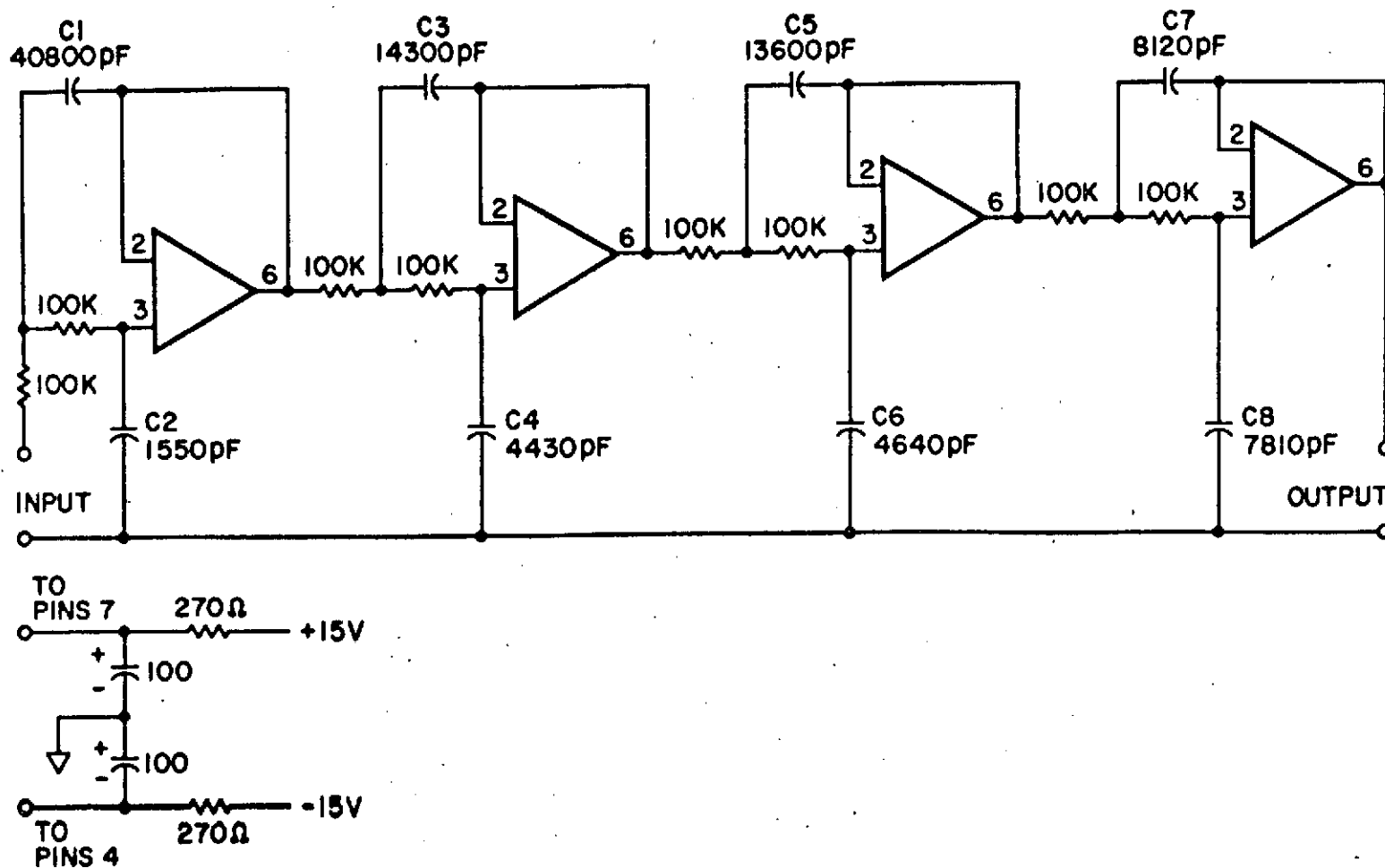


Figure 2.6. Low Pass Filter Circuit

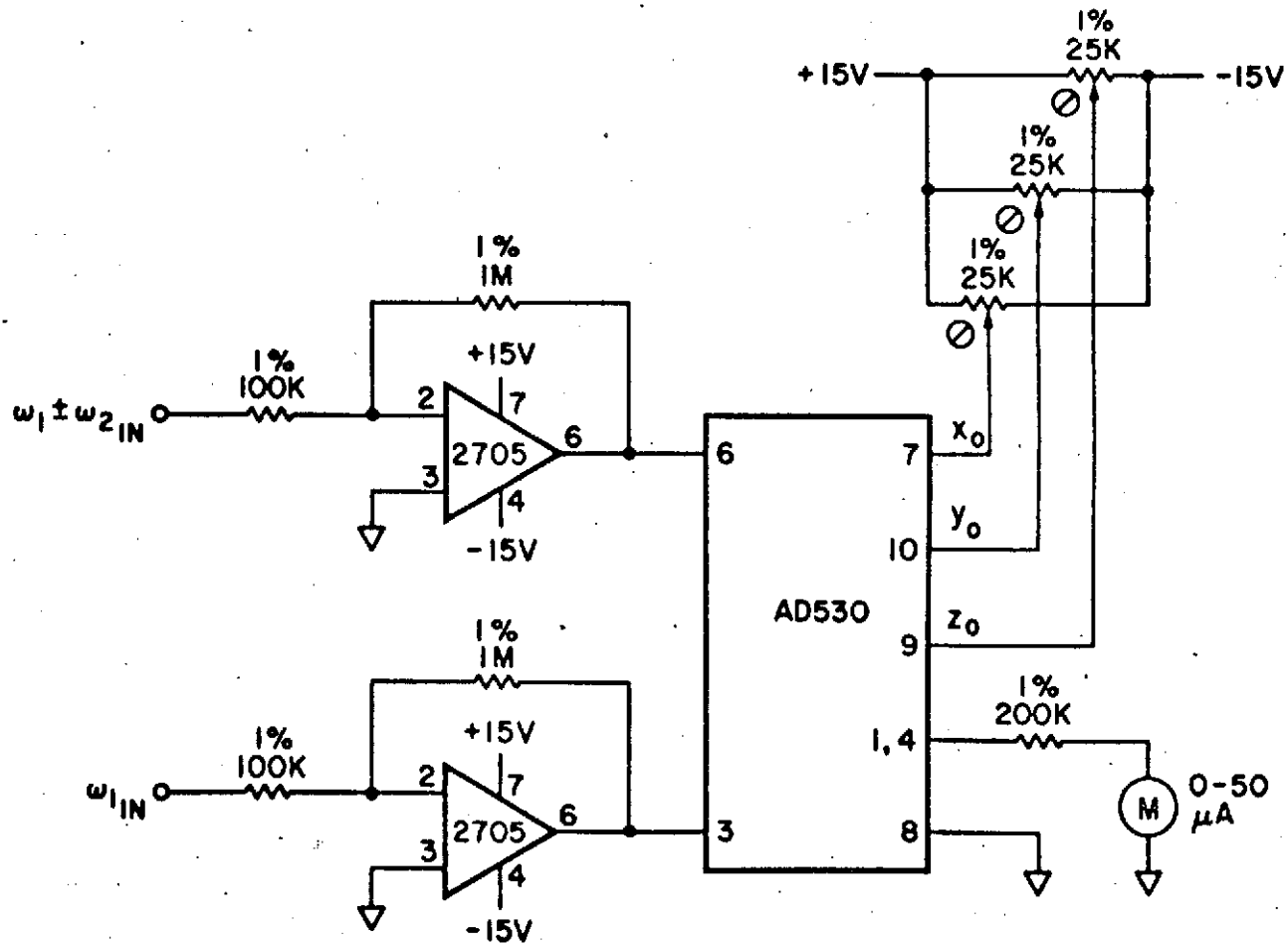


Figure 2.7. Output Divider Circuit

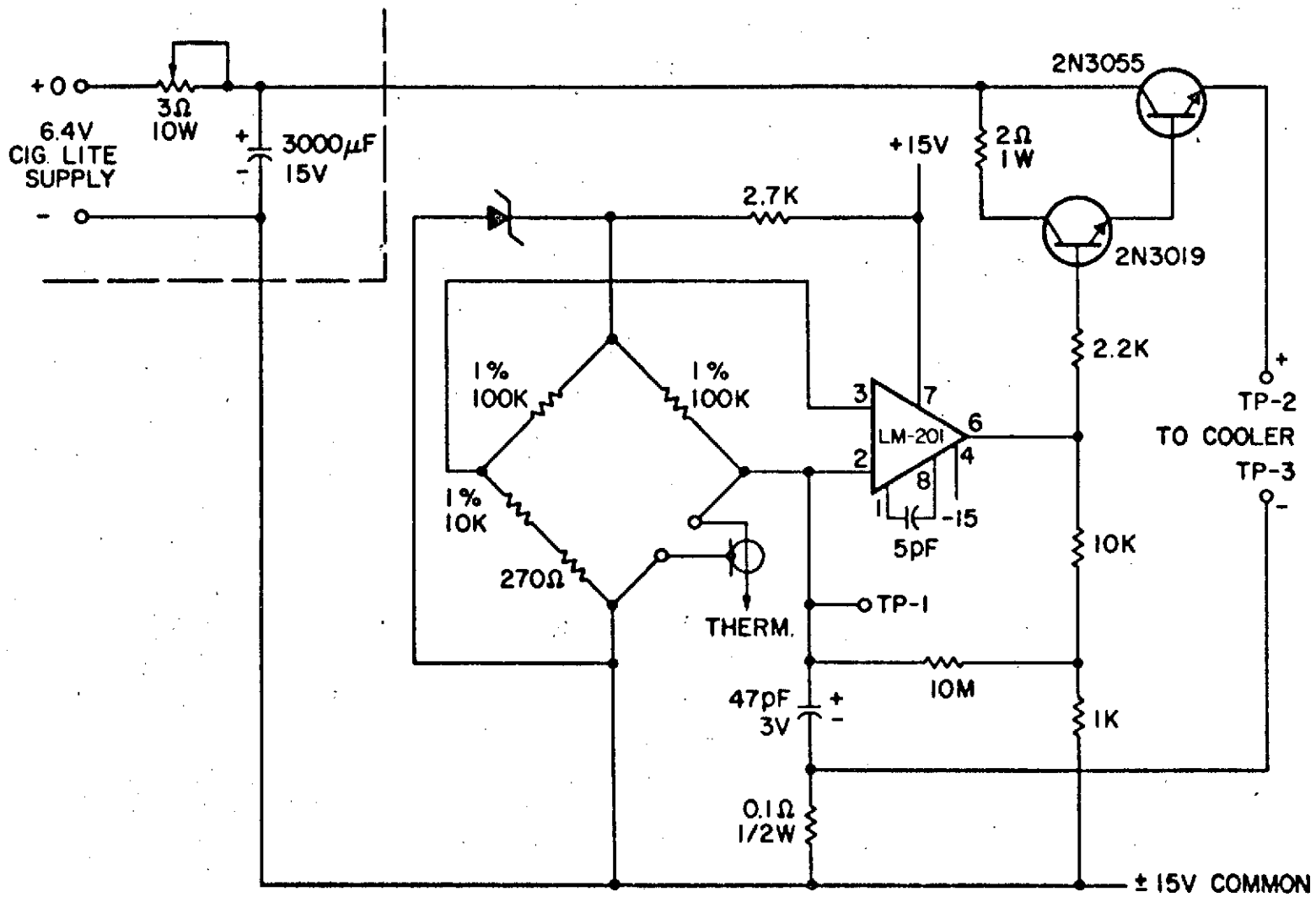


Figure 2.8. Thermoelectric Cooler Control Circuit

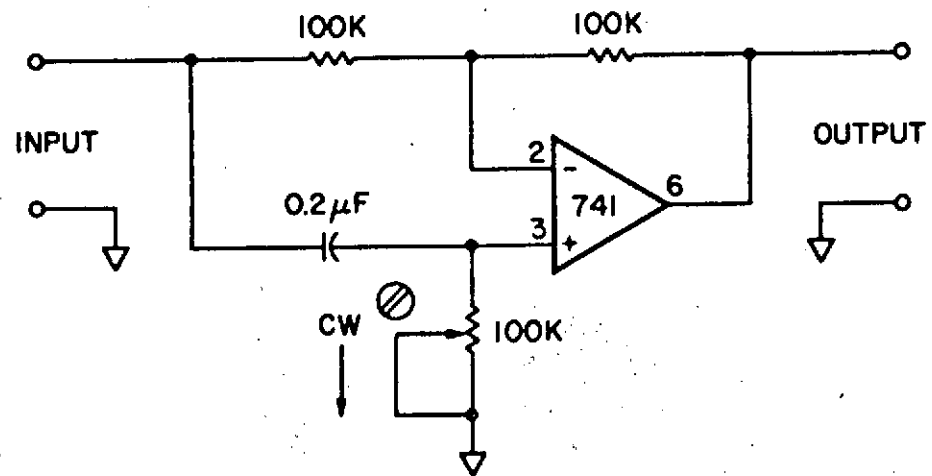


Figure 2.9. 0-180° Constant Amplitude Phase Shifter Circuit

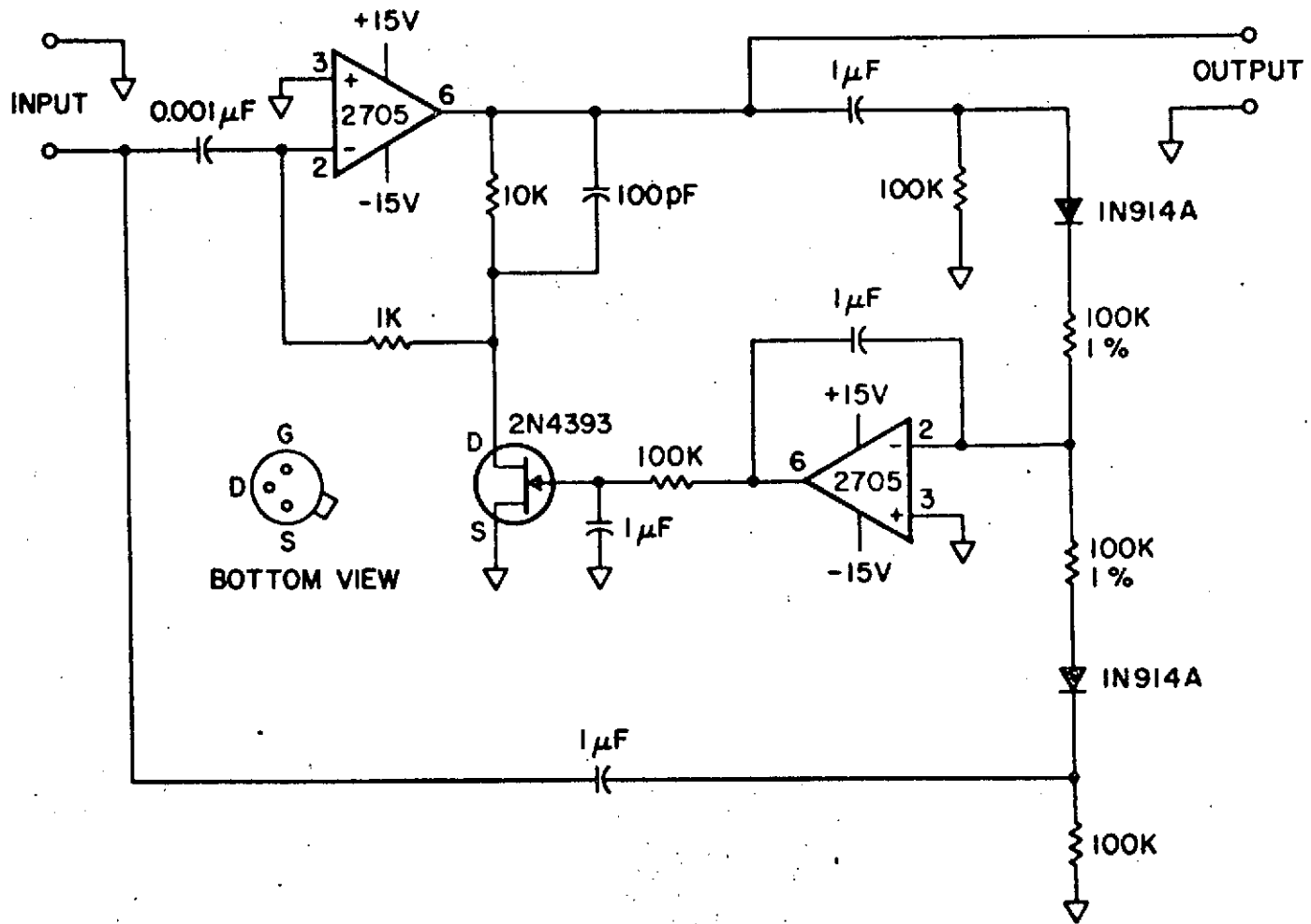
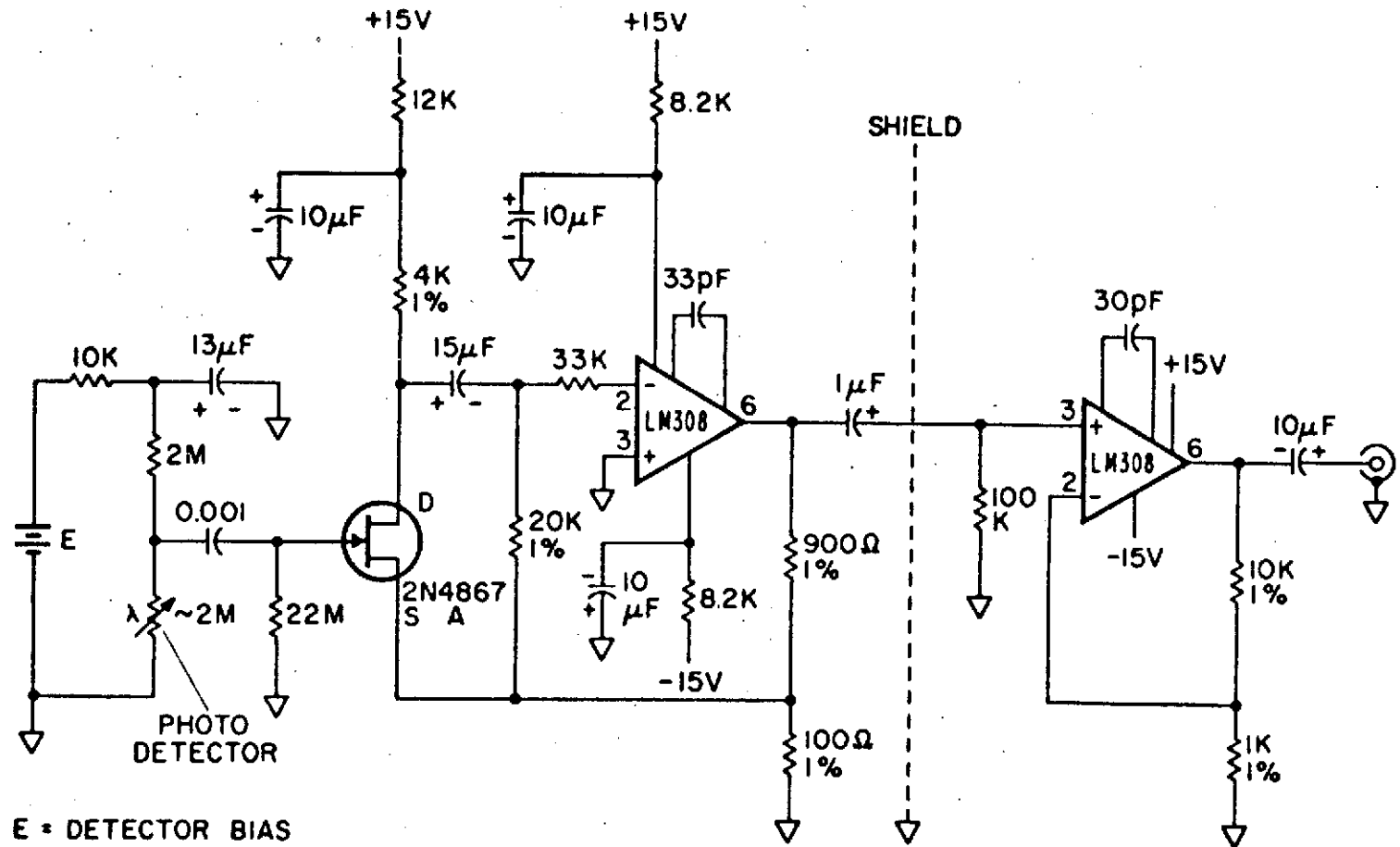


Figure 2.10. Constant Amplitude 90° Phase Shift Circuit



E • DETECTOR BIAS

Figure 2.11. Preamplifier Circuit

2.2 Debugging the Ames Analyzer

The prototype analyzer delivered to Andros, although completely assembled, had not been tested as a system and so the first task was to make the system operational.

The optical system was found to have large gas leaks which were primarily traced to the J.B. Lansing acoustic driver units. These units are, of course, not designed to be gas tight, and suffered from two major difficulties in the application:

- a. The end caps did not seal well to the driver body, nor were the electrical feedthroughs suitable for gas-tight service. A rubber sealing ring was placed between each end cap and driver body and the feedthroughs were sealed with epoxy to overcome these difficulties.
- b. The internal construction of the drivers is such as to leave some large "dead" gas spaces, and the net result is that initially the Helmholtz cavities showed a long time response to a change in gas concentration. This problem was largely cured by providing small communicating holes between the air spaces in the driver, and by removing the foam sound absorbing material packed in the end cap. In addition, all of the internal metal surfaces in the drivers which were accessible were coated with epoxy to render them less porous.

The other main problem encountered with the prototype analyzer was in the driver-oscillator circuits. Initially the circuits were found to be unstable at turn on and frequently the system would start to oscillate with high amplitude at around 5 - 6 KHZ instead of at the Helmholtz frequency near 500 Hz. This was eventually tracked down to a resonance of the pressure transducer. Many iterations and interim solutions to this problem were tried out before the circuitry was finally modified as described in Chapter III. At this stage we arrived at an interim solution where both the sample and reference oscillators would operate reasonably

stably with peak-to-peak pressure excursions in the cavities of 1.5 to 2.0 psia. It was then decided to proceed with some gas sensitivity measurements with the prototype analyzer before contemplating further modifications to the instrument.

2.3 Gas Measurements with the Prototype Analyzer

Carbon dioxide was selected as the most suitable gas to use to measure the instrumental sensitivity. CO₂ has an exceptionally strong ($S = 2500 \text{ atm}^{-1} \text{ cm}^{-2}$) absorption band at 4.35μ in the infrared, also it is a non-toxic and easily handled species.

From the start of gas measurements, it was clear that the analyzer had poor sensitivity, and that this was due to the low transmission efficiency for radiation from the infrared source. Measurements were made of the total black body power striking the detector, and the power in a wavelength interval near the 4.35μ CO₂ band. The measured transmissions are shown in Table 2.1, and were somewhat less than 10^{-4} .

TABLE 2.1
MEASURED TRANSMISSION EFFICIENCY OF THE AMES PROTOTYPE ANALYZER

Wavelength Interval	Power leaving IR Source (Watts)	Power detected by detector	Transmission
Total	4	0.32×10^{-3}	0.8×10^{-4}
4.1 - 4.7μ	0.38	0.018×10^{-3}	0.5×10^{-4}

The low transmission is due primarily to the 0.2" diameter stop placed $1 \frac{1}{4}$ " from the IR source as shown in Figure 2.1. Additional losses come from transmission through 3 lenses and 4 windows, the second stop, and the detector which does not intercept all of the final beam image. The measured attenuation was in agreement with the attenuation expected from the design of the analyzer.

Signals out of the detector at the primary modulating frequencies and at the heterodyne frequency were as expected from the black body flux incident on the detector. The CO_2 in one cell was replaced by N_2O to verify that the signal at the heterodyne frequency was due to heterodyning in the gas and not in the detector or electronics. Noise levels were also measured and agree well with the noise level quoted by the manufacturer of the detector. Heterodyne signals for various gas concentrations were measured to determine the ultimate sensitivity of the instrument. With 1.3 psi p-p pressure excursions in both cells, and with a 10 second integration time the signal-to-noise ratio was unity at 50 ppm CO_2 . By increasing the p-p pressure excursions in both cells by a factor of 3 (which we were unable to do because of problems with the driver units), the sensitivity could have been increased by roughly an order of magnitude to obtain a sensitivity for the instrument as delivered to us of 5 ppm CO_2 .

All of the electronic processing circuitry of the Ames heterodyne analyzer operated satisfactorily at the limit of sensitivity of the instrument. At this point it was concluded that the next step should be to reconfigure the optical system for higher throughput to increase the basic instrumental sensitivity.

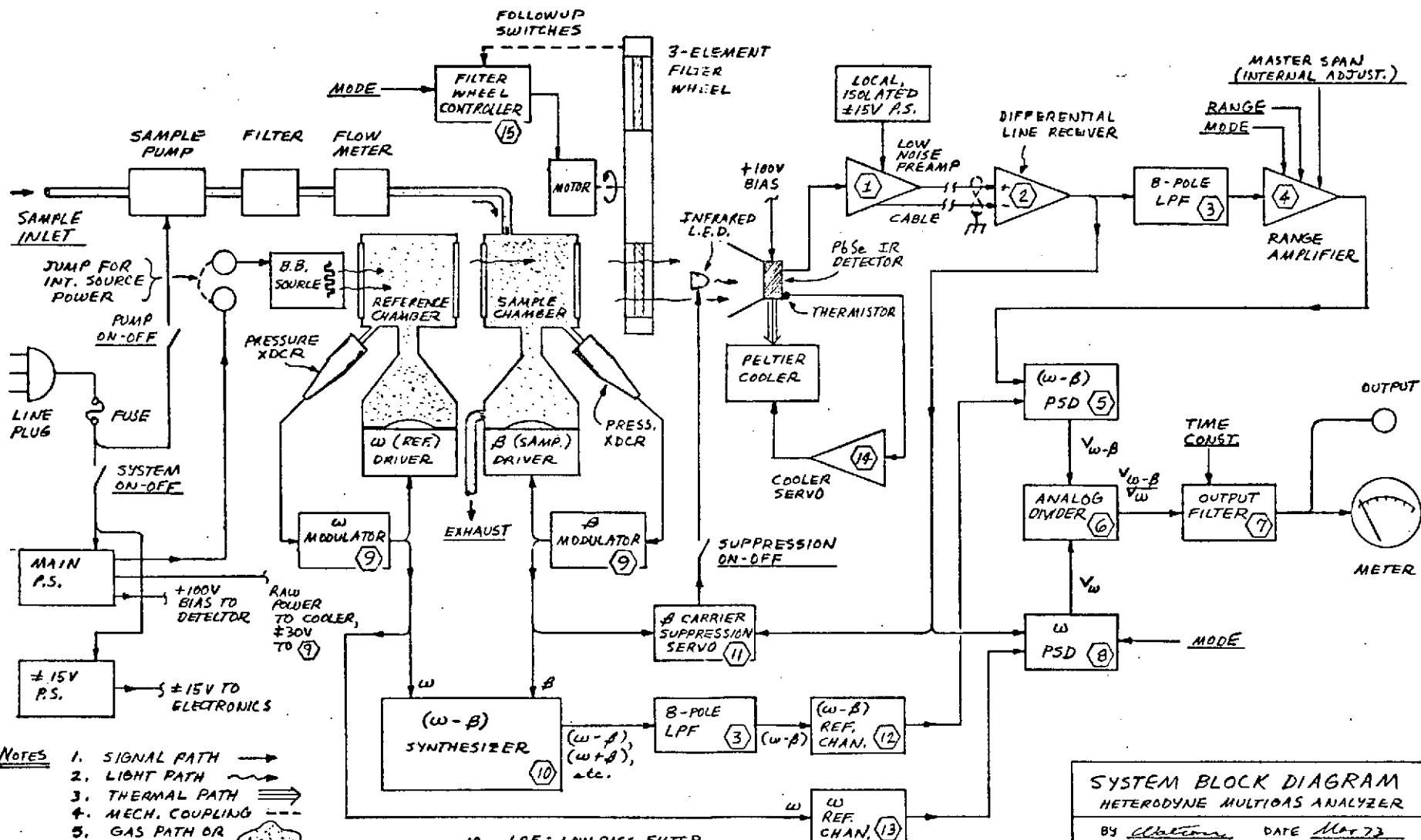
3 DESCRIPTION OF THE FINAL HARDWARE

Introduction

At the conclusion of the testing program of the Ames Prototype Heterodyne Analyzer it was clear that a redesign of the optical bench and the electronic processing circuitry would yield a "second generation" prototype instrument with substantially improved performance and flexibility.

Modifications to the optical bench were primarily directed toward improving the energy throughput as a means of substantially increasing the sensitivity of the analyzer. Referring back to Figure 2.1, the optical system modifications consisted of removing all aperture and lenses from the system and rearrangement of the remaining components to close up the spaces between the source, resonators and detector. A conical light collector, of half angle 25° , was installed on the infrared detector. In the new optical system most of the forward going radiation from the black body source was reflected from the resonator walls and efficiently collected by the light cone and focused onto the infrared detector. It can be estimated from the sensitivity measurements detailed in Section 4 that the radiation throughput was increased by a factor of 20-40 over the Ames prototype analyzer, with a similar increase in sensitivity to gaseous species in the sample cell resonator. The penalty incurred in using reflected radiation from the resonator walls (this radiation was eliminated in the Ames prototype analyzer described in Section 2) was that the optical system became somewhat more vibration sensitive, as was to be expected. This was resolved by mounting the infrared source, infrared detector and both resonators very solidly to a massive baseplate (10 lbs) so that relative motion of the components was essentially eliminated.

The following subsections, 3.1 through 3.16, give a detailed account of the processing electronics and power supplies incorporated in the final prototype analyzer.



NOTES

1. SIGNAL PATH →
2. LIGHT PATH ~~~~~
3. THERMAL PATH ≡≡≡
4. MECH. COUPLING - - -
5. GAS PATH OR VOLUME [Diagram of a chamber]
6. MODE SELECTS CO, CO₂, OR CH₄.
7. RANGE SELECTS 100, 300, 1000, OR 3000 PPM FULL SCALE. { SEE ALSO DWG SK22B AND BLOCKS (4) & (8).
8. TIME CONST. SELECTS 1, 3, 10, 30, 100 SEC;
9. (X) IDENTIFIES BLOCKS HAVING DETAIL SCHEMATICS
10. LPF = LOW PASS FILTER
11. PSD = PHASE SENSITIVE DETECTOR

SYSTEM BLOCK DIAGRAM
 HETERODYNE MULTIGAS ANALYZER
 BY *Electronics* DATE *Mar 73*
 ANDROS, INC, BERKELEY, CA
 SK 251 SH. 1 OF 1.
 REV 2 MAR 24-73

3.1 Low Noise Preamp - Block , Figure 3.1

This amplifier was but slightly altered during the course of the work. Very low noise performance is achieved as a consequence of the premium low noise junction FET used at the input, and the unique method of its operation at zero bias. However, this level of noise is well below what is required for detector-noise-limited performance. Other noise mechanisms dominate the system at the present level of development, most notably photon noise and noise on the ω and β cavity drive signals. Another noise source is the metal film load resistor for the detector. Such resistors exhibit current noise in excess of fundamental Johnson noise. We know of only three kinds of resistors that do not exhibit current noise:

- a. wire wound
- b. IRC Div of TRW series AR metal film
- c. Special glas frit.

The metal film unit was tried with inconclusive results since the system was still dominated by other noise sources and no change of bias voltage was made. These PbSe detectors will yield better S/N at higher bias; e.g., 200-400V.

The amplifier was taken off the system's main $\pm 15V$ bus and put on a local, floating, $\pm 15V$ power supply. This measure served to break a troublesome ground loop which is discussed in greater detail in Section 3.16.

3.2 Differential Line Receiver - Block , Figure 3.2

The unit gain noninverting differential line receiver was added to the system to cope with extraneous noise picked up on the long preamp output cable. This amplifier has a nominal design common-mode rejection factor of approximately -40 db_v . It serves to interface the separate common-rails of the preamp and the rest of the system. In addition, it serves as a line driver to other system points.

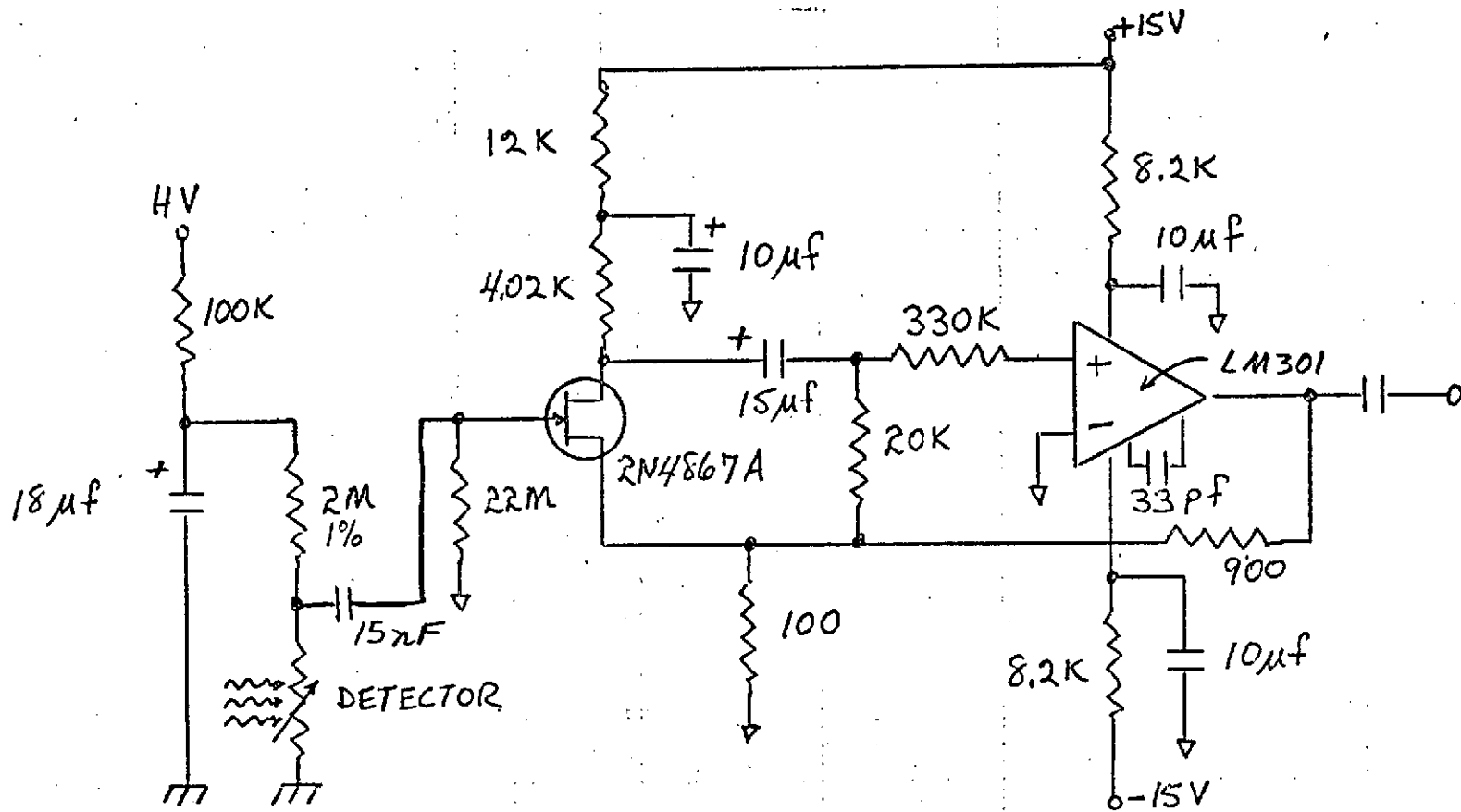


Figure 3.1. Low Noise Preamplifier - ①

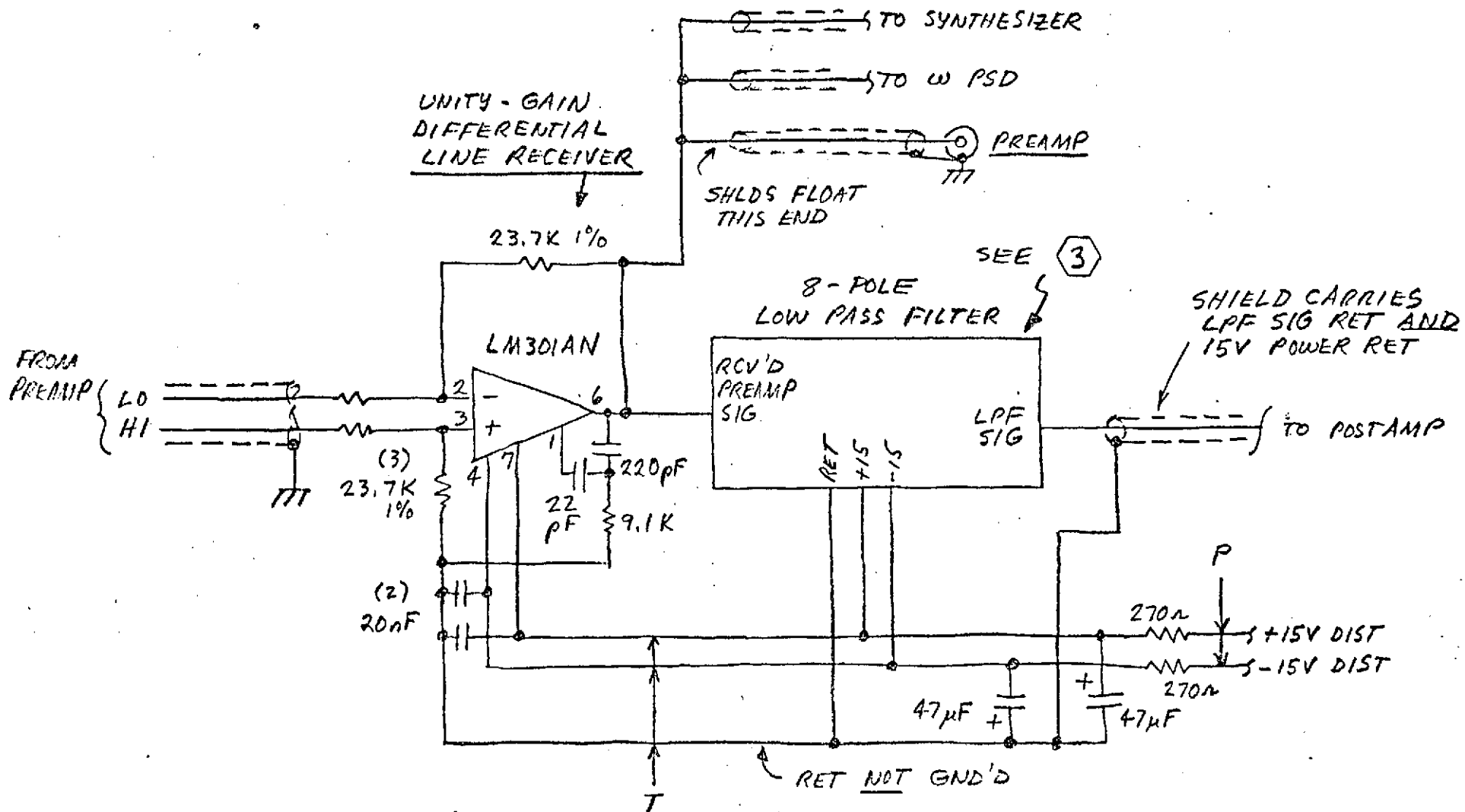


Figure 3.2. Diff. Line Receiver (w-β) Signal Channel - 2

3.3 Low-Pass Filter (LPF) - Block , Figure 3.3

The two low-pass filters used in the system are of 8-pole Butterworth configuration. These filters were not altered in the course of the program except for the addition of the line receiver (2) ahead of the LPF in the signal line from preamp (1).

3.4 Range Amplifier - Block , Figure 3.4

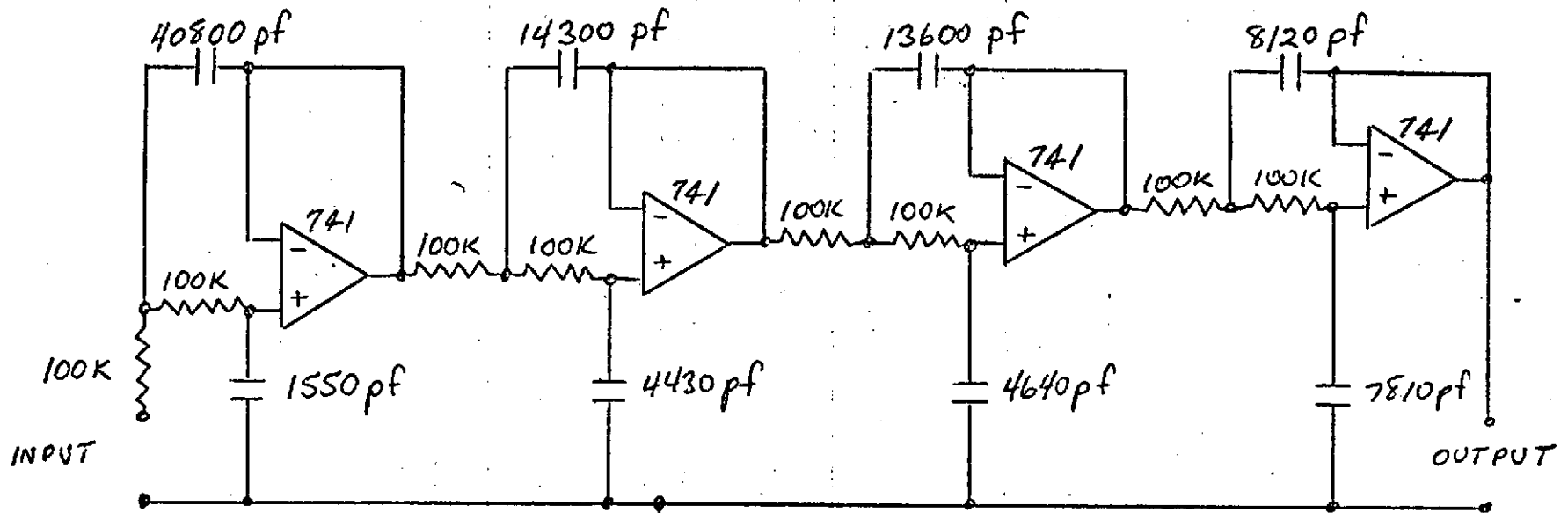
Extensive modifications to the signal channel were necessary to overcome the following difficulties:

- a. On higher sensitivities, the analog divider inputs were running very close to zero volts, forcing the divider to operate at high gain with attendant aggravated noise and drift. This caused erratic system operation and high sensitivity to temperature changes.
- b. The phase sensitive detectors were operating at high DC gain, and were unbalanced, thus producing substantial temperature sensitivity (see Section 5).

The changes placed all gain switching ahead of the divider (6), in the AC signal path. The ω denominator term in the system transfer function $\frac{V_{\omega-\beta}}{V_{\omega}}$ was maintained at -8V on all ranges and the and the $\omega-\beta$ numerator scaled 0 to -8V at full scale (FS).

The range amplifier begins with a postamplifier having a gain adjustment of 35 to 200. Since this adjustment affects all ranges equally, it is used as the Master Span control in calibrating the system.

The signal from the postamplifier is delivered to the Gas Mode Selector Amplifier. This operates at a fixed gain of about 17 in CH₄ mode. On CO or CO₂, however, electronic switches connect adjustable-gain networks so the span for CO and CO₂ can be individually trimmed. (It is necessary to first adjust Master Span in the CH₄ mode.)



100K RESISTORS 1% MET. FILM.

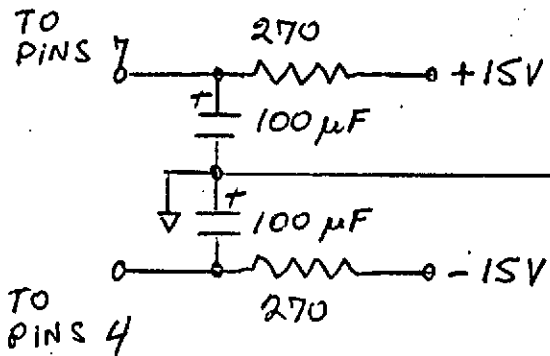


Figure 3.3. Low Pass Filter - 3

NOTE: FETS KE4393.
DIODES 1N914.

⊕ DOT
DENOTES OUTSIDE
FOIL,

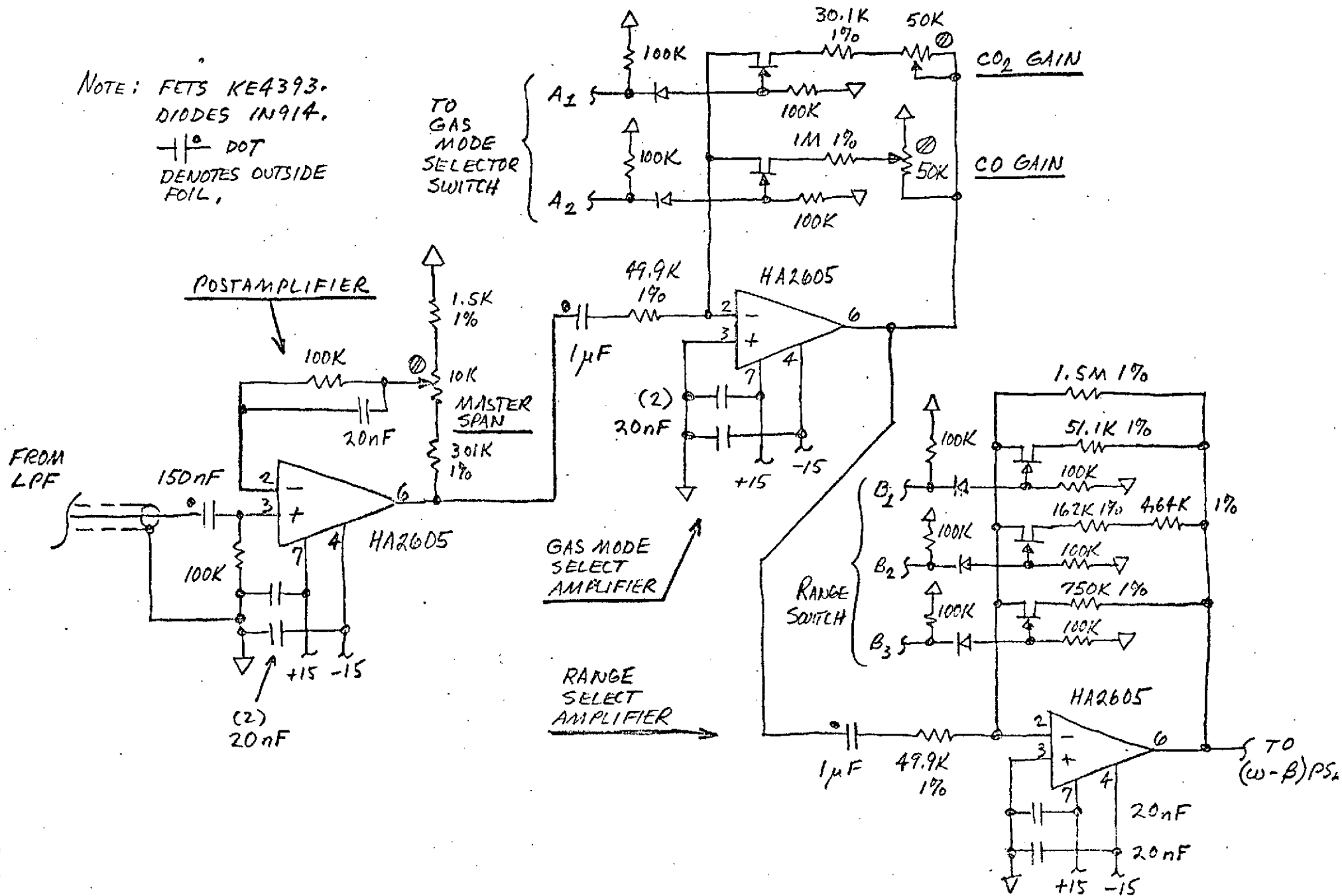


Figure 3.4a. Range Amplifier - 4

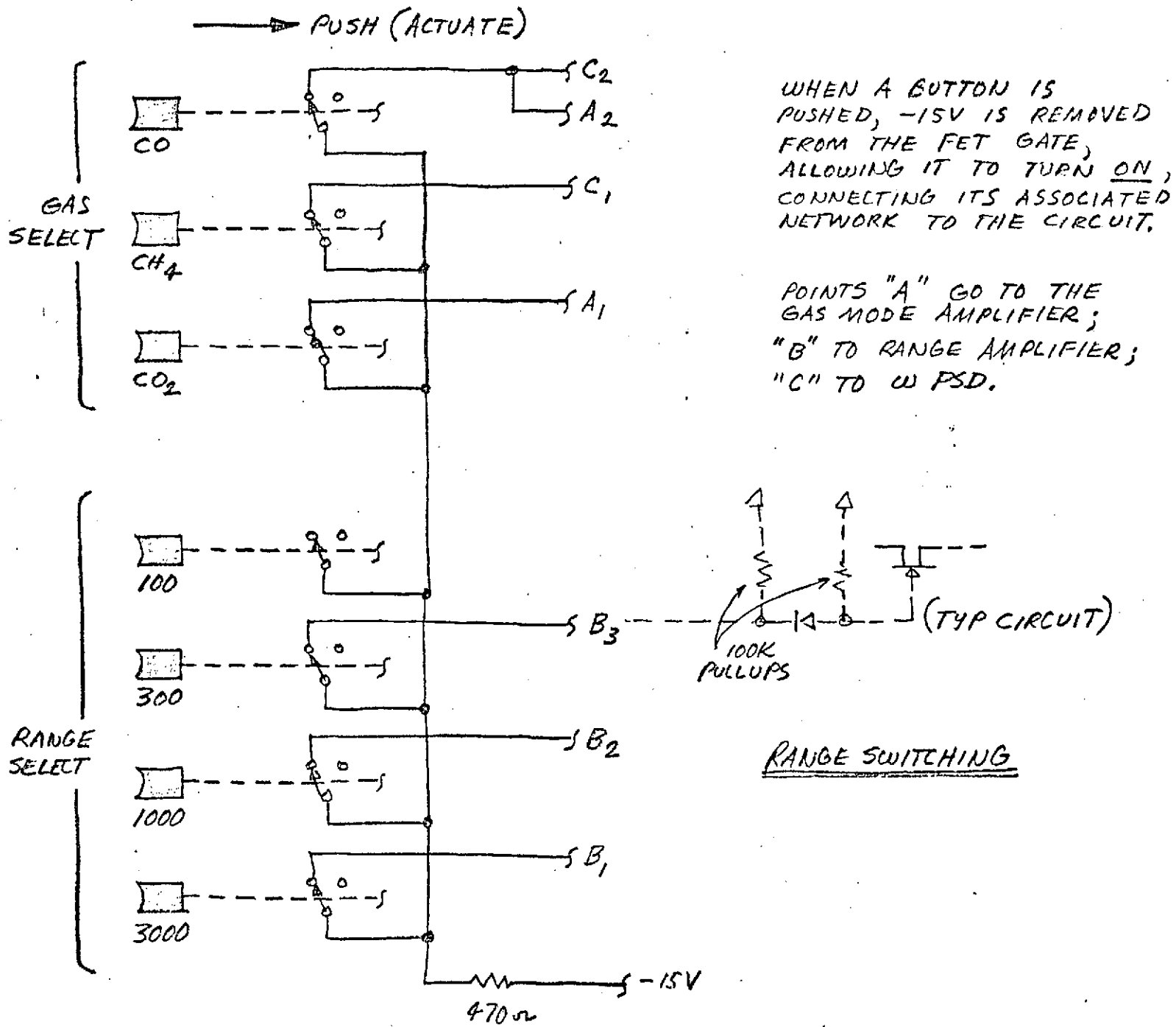


Figure 3.4b. (w-β) Signal Channel - 4


The mode-leveled signal goes next to the Range Select Amplifier where a similar switching scheme is used to change gains to suit each range.

This technique for gain-switching with FETs was chosen to avoid the problems certain to arise in carrying amplifier input leads long distances to switches; e.g., oscillations, noise, crosstalk, and contact resistance difficulties could be confidently predicted. Moreover, remote switching minimized the circuit-switch interface and permitted one switch pole per function.

For the 100 ppm range no separate adjustment is provided, so calibration of this range must be done first, in the CH₄ mode, and with the Master Span control (see above).

Gains in this system after the modification were such that 2 VPP at the input to the (ω - β) PSD corresponds to full scale.

After this modification was made, testing revealed that hum and noise in the signal was excessive on the sensitive ranges, causing amplifier saturation and swamping the PSD. This noise was later reduced (described elsewhere) but an interim "fix" involved the use of higher DC gain in the PSD and AC gain. Consequently, the gain of the postamplifier was decreased about a decade. The system was not returned to the low gain PSD amplifier configuration even though this would now be possible.

3.5 ω - β PSD - Block , Figure 3.5a (revised circuit) and
2.5 (original circuit)

The necessity to adjust system gains (as discussed in 3.3 above), and the observed temperature dependency of the PSD provoked a more careful look at this important circuit.

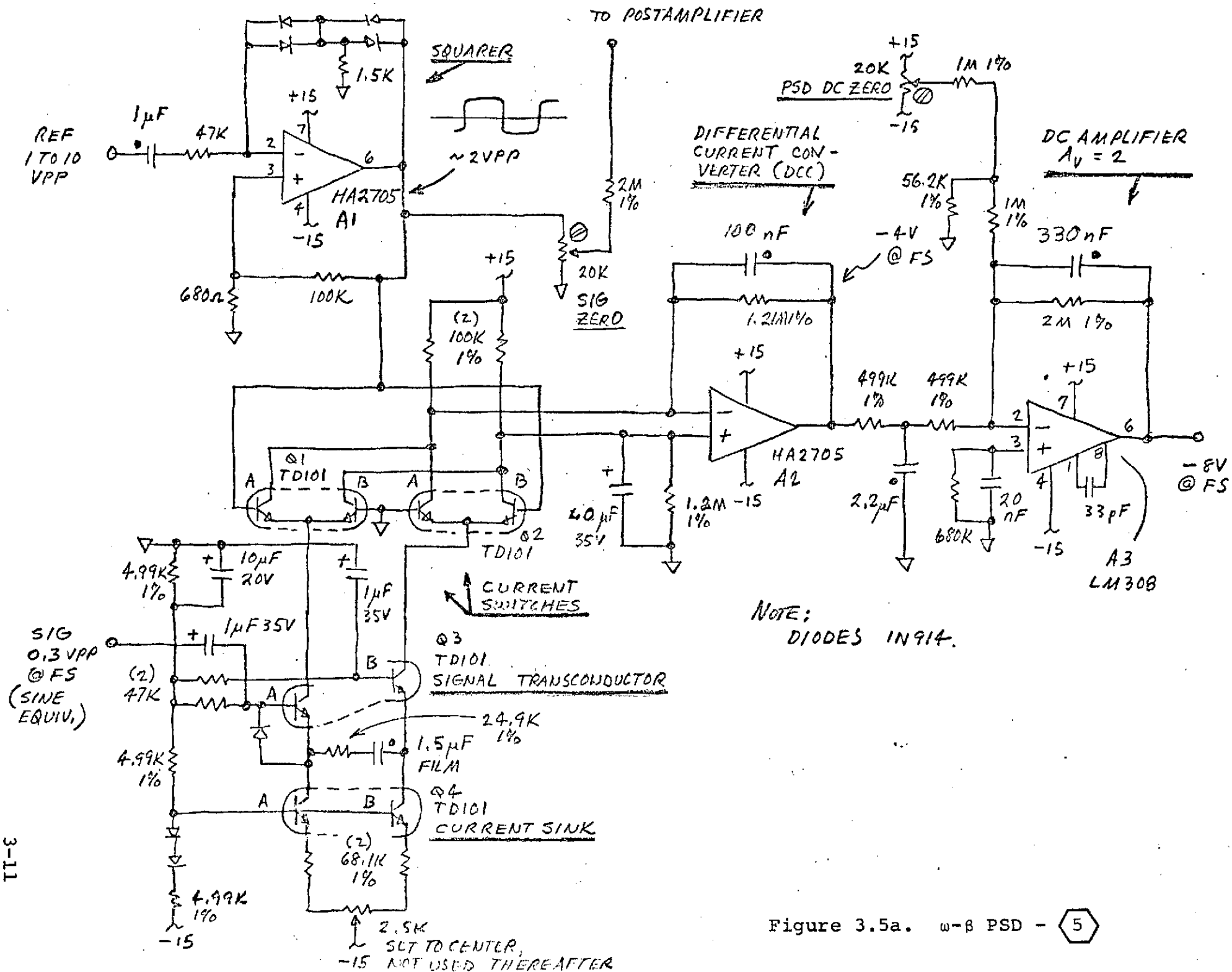
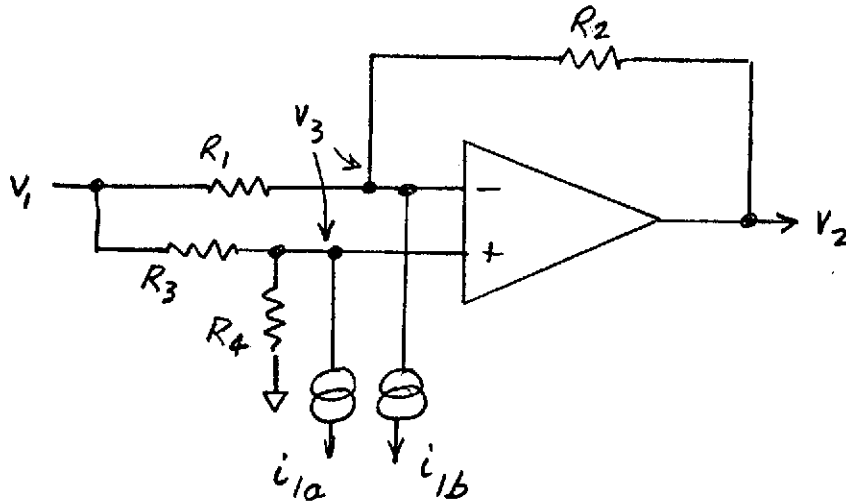


Figure 3.5a. ω - β PSD - 5

A model for this circuit is as follows:



The current sinks i_1 represent the collectors of the driving current-switch transistors. It is initially assumed that $i_{1a} = i_{1b}$, $R_1 = R_3$, $R_2 = R_4$. The output V_2 is related to V_1 (V_1 being the V_{cc} supply for the current switches) by

$$(1) V_2 = V_1 \left(\frac{R_2}{R_1} \cdot \frac{R_4}{R_3 + R_4} + \frac{R_4}{R_3 + R_4} - \frac{R_2}{R_1} \right)$$

assuming $i = 0$.

If $R_1 = R_3$ and $R_2 = R_4$, this reduces to

$$(2) V_2 = V_1 \left(\frac{R_2}{R_1} \frac{R_2}{R_1 + R_2} + \frac{R_2}{R_1 + R_2} - \frac{R_2}{R_1} \right)$$

$$= V_1 \left(\frac{R_2 R_1 + R_2^2 - R_2 (R_1 + R_2)}{R_1 (R_1 + R_2)} \right)$$

$$= 0$$

Thus the circuit is balanced, and the supply voltage V_1 is "rejected" by the CMRR of the connection. This, of course, depends on the matching of the resistors and symmetry of the amplifier.

If, say, R_1 has a temperature drift unmatched by R_3 by $m \text{ } ^\circ\text{C}^{-1}$, then a difference current

$$\begin{aligned}
 (3) \quad i_2 &= \frac{V_1}{R_1} - \frac{V_1}{R_1'} \\
 &= \frac{V_1 R_1' - V_1 R_1}{R_1 R_1'} = V_1 \left(\frac{R_1' - R_1}{R_1 R_1'} \right) \\
 &= V_1 \frac{\Delta R_1}{R_1^2} = \frac{V_1}{R_1} \frac{\Delta R_1}{R_1} \\
 &= \frac{V_1}{R_1} m; \quad m = \frac{\Delta R}{R}
 \end{aligned}$$

This current passes through R_2 to become

$$(4) \quad V_2' = i_2' R_2 = V_1 m \frac{R_2}{R_1}$$

For the original circuit this works out to

$$\begin{aligned}
 V_2' &\approx 15\text{V} \times 10^{-4}/^\circ\text{C} \times \frac{10^6 \text{ ohm}}{10^5 \text{ ohm}} \\
 &= 15\text{mV}/^\circ\text{C}
 \end{aligned}$$

On the least sensitive range and mode, assuming $V_2 = 1\text{V}$ @ FS, this is

$$(5) \quad \text{Drift} = \frac{1.5 \times 10^{-2}}{1} = 1.5\% \text{ FS}/^\circ\text{C}.$$

The most sensitive range is approximately 510 times more sensitive. The PSD FS output is thus 510 times lower and the resulting CMR-limited drift is

$$(6) \text{ Drift} = 5.1 \times 10^2 \times 1.5 \times 10^{-2} = 7.65/^\circ\text{C}$$

or 765% FS/°C!

This is untenable and accounts for the great difficulties experienced on the more sensitive ranges.

This does not include the effects of reduced divider stability at low input levels, nor the imbalance present in the current switches i_1 . Let us briefly examine the latter by re-evaluating V_2 considering the effects of i_1 .

$$(7) V_3 = \frac{V_1 R_4 - i_{1a} R_3 R_4}{R_3 + R_4}$$

$$(8) V_2 = V_3 - i_2 R_3 + i_{1b} R_2 \quad i_2 = \frac{V_1 - V_3}{R_1}$$

$$(9) V_2 = \frac{V_1 R_4 - i_{1a} R_3 R_4}{R_3 + R_4} - \left[\frac{V_1 - \frac{V_1 R_4 - i_{1a} R_3 R_4}{R_3 + R_4}}{R_1} \right] R_2 + i_{1b} R_2$$

$$(10) V_2 = \frac{V_1 (R_1 R_4 - R_2 R_3) - i_{1a} (R_1 R_3 R_4 + R_2 R_3 R_4) + i_{1b} (R_1 R_2 R_3 + R_1 R_2 R_4)}{R_1 (R_3 + R_4)}$$

$$(11) V_2 = i_{1a} - i_{1b} R_2 = \Delta i R_2.$$

It is seen that V_2 is not affected if $i_{1a} = i_{1b}$; and the inherent differencing property for unbalance current Δi is shown.

This gives the effect for any current imbalance, including those originating from the amplifier offset current. Thus, the bias current in R_1 and R_3 must be $\gg i_{\text{offset}}$, and no greater than typical $i_2' \cong \frac{V_1}{R_1} \cdot \frac{\Delta R}{R}$ from 3.3 which yields

$$(12) i_2' \cong \frac{15}{10^5} \times 10^{-4} \text{ }^\circ\text{C} = 15\text{nA}/^\circ\text{C}$$

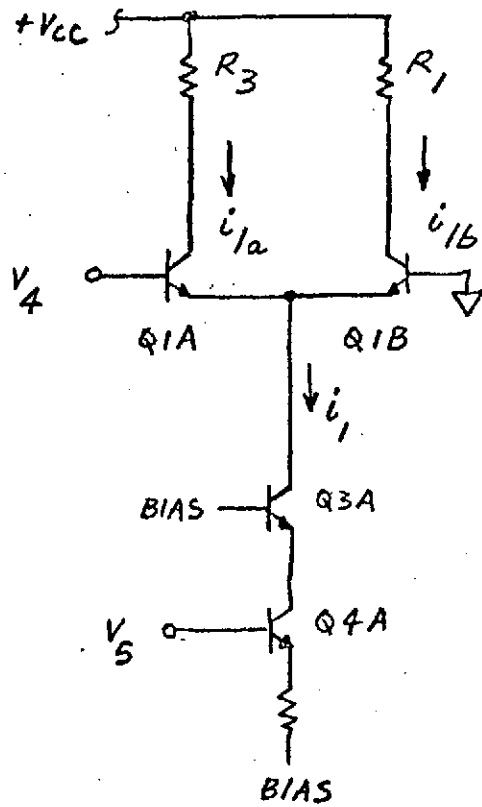
Since the opamp offset current is less than $1\text{nA}/^\circ\text{C}$, the circuit drift is heavily dominated by resistor mismatching.

The drift computed under (4), $15\text{mV}/^\circ\text{C}$, would be acceptable if full scale output was always around 10V . This leads to the rationale behind the modification which put nearly all the gain ahead of the PSD so the PSD proper could operate always at high level. By reducing the PSD DC gain by a decade, an acceptable drift level of about $0.015\% \text{ FS}/^\circ\text{C}$ is achievable.

Now let us turn to the balance of the original PSD (refer to Figure 2.5), especially the current switches and circuitry used to generate i_{1a} and i_{1b} .

The signal is injected at the base of Q4A, on the left side of the PSD. It is transferred through cascode transistor Q3A and switched into branch a or b by Q1A and B. A simplified diagram of this circuit is shown in Figure 3.5b with the accompanying waveforms. Note that branches a and b carry only half-wave rectified currents.

Now examine the right-hand half of the PSD, Q2, Q3B, and Q4B. Note that no signal is injected anywhere into the right-hand half. Consequently, the only currents pumped into branches a and b are the switched DC bias currents of the right-hand half. Of course, DC bias is also commutated by the left-hand half along with whatever signal is present. It is easily shown, however, that any DC which



Simplified schematic, left half-stack, PSD (original config.)

Waveforms of above circuit

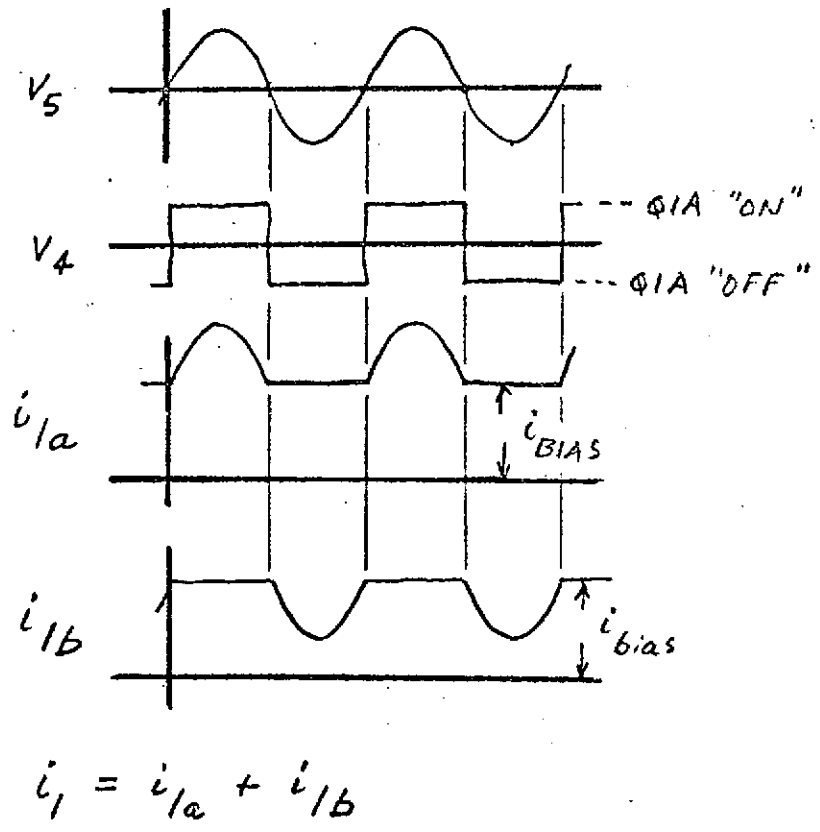


Figure 3.5b.

is chopped in exact symmetry (i.e., so the resulting square wave is entirely free of even harmonics) does not contribute to the output V_2 . It is clear that only half this circuit is doing any work. The cascode Q3 is superfluous since Q1 is also a cascode when "ON" and there is nothing to be gained by the resulting double-cascode circuit. The PSD circuitry was rearranged to overcome these problems as follows:

1. The reference squaring amplifier was diode-clamped to reduce transient noise resulting from its 30 VPP unrestrained open loop swing. A small amount of hysteresis was added to eliminate edge-chatter and enhance clean switching.
2. 1.5K resistors in the emitters of Q1, 2 were removed since it is necessary only to turn the transistors on or off, and the resistors impede that function.
3. The point of signal injection was moved to the base of Q3A.
4. Coupling to the opposite side and inversion are achieved simultaneously by the AC network between the emitters of Q3. The AC gain of the PSD is set by the resistor in this network.
5. Q4 became, conveniently, a fixed current sink carrying no signal as such, but it is this current sink which generates inversion by forcing Q3B to complement any signal current injected across from Q3A.
6. The 2.5K trimmer is totally unnecessary and has no effect on circuit operation. It was set to center and forgotten.
7. Bias was set to 75 μ A, which would assure centered operation and give a modest crest factor (slightly under 2). One wants no more unused bias than is necessary to absorb the signal swing, since asymmetric reference will act on it to cause offsets.
8. A2 and A3 were interchanged, so the faster HA2705 handled signal commutation and the slower LM308 provided DC gain and integration.

9. The zeroing network was changed to eliminate A3 as a drift source.
10. AC transconductance was decreased from approximately 10^{-3} mho to 4×10^{-5} mho to establish scaling, improve linearity, and eliminate minor temperature dependence of gain and hence span (due to the temperature term in the transistor transconductance equation) in Q4A
11. DC gain was decreased from 100 to 2 to improve stability. A gain of 2 appears to be the lowest realistically obtainable since operating A2 much beyond $\pm 5V$ would cause Q1 and Q2 to saturate.
12. Scale factor was set at -8V FS, allowing some over-ranging.

The PSD thus rebuilt yielded the predicted transfer function. Temperature sensitivity could only be qualitatively checked. Predicted temperature sensitivity of the revised PSD is

$$(13) \text{ Drift} = \frac{i_2' R_3}{4} \text{ per } ^\circ\text{C} \quad \text{Where } R_3 = 100K \text{ and full scale} = 4V \text{ at A2, and one resistor drift of } 10^{-4}/^\circ\text{C} \text{ is assumed.}$$

$$= \frac{1.5 \times 10^{-8} \text{ A} \times 10^5 \Omega}{4V} = 3.75 \times 10^{-4}/^\circ\text{C} \approx 0.04\% \text{ SF}/^\circ\text{C}.$$

This is an acceptable drift level.

It is noted that with both sides of the PSD working, the system S/N ratio is theoretically improved by $\sqrt{2}$. This was not experimentally verified because other changes were made at the same time.

As a consequence of 60hz noise problems, it was later necessary to increase the PSD DC gain by a decade. This is the configuration shown in Figure 3.5a. This would produce a drift of approximately

0.4% FS/°C which is marginally acceptable. However, we believe that still later noise improvements would permit the PSD to be returned to its low-drift state or close to it.

In final comment, it is noted that other drift mechanisms prevail that have not been considered in this limited analysis. Such factors as transistor h_{fe} , leakage, etc., must be considered if ultimate performance is needed. However, resistor mismatching is the dominant source of drift here, so that improvements of up to a decade are probably possible by using lower TCR resistors or matched film networks.

This type of PSD has the principal virtue of high frequency capability since all switching is done in the current mode. It is not, in our opinion, optimally suited to low-drift applications for the reasons made clear above. Nor is it particularly good at handling poor signal/noise ratios (i.e., high crest factors). Since high frequency capability is not a factor here, it is recommended that subsequent models employ a different type PSD which has better drift and noise handling properties.

3.6 Analog Divider - Block , Figure 3.6

The ratio operation $\frac{V_{\omega-\beta}}{V_{\omega}}$ is performed here. DC amplifiers originally present at the inputs were eliminated when the signal channel was modified, since both the ω and $\omega-\beta$ PSDs now yield outputs at high level (8V) suitable for direct application to the divider.

A scale factor (gain) adjustment was added to provide a 10V output with 8V inputs.

3.7 Output Filter - Block , Figure 3.7

In suppressed carrier systems such as this, system bandwidth is fixed by a low-pass filter following rectification. For simple uncoupled RC filters, the equivalent noise bandwidth resulting is

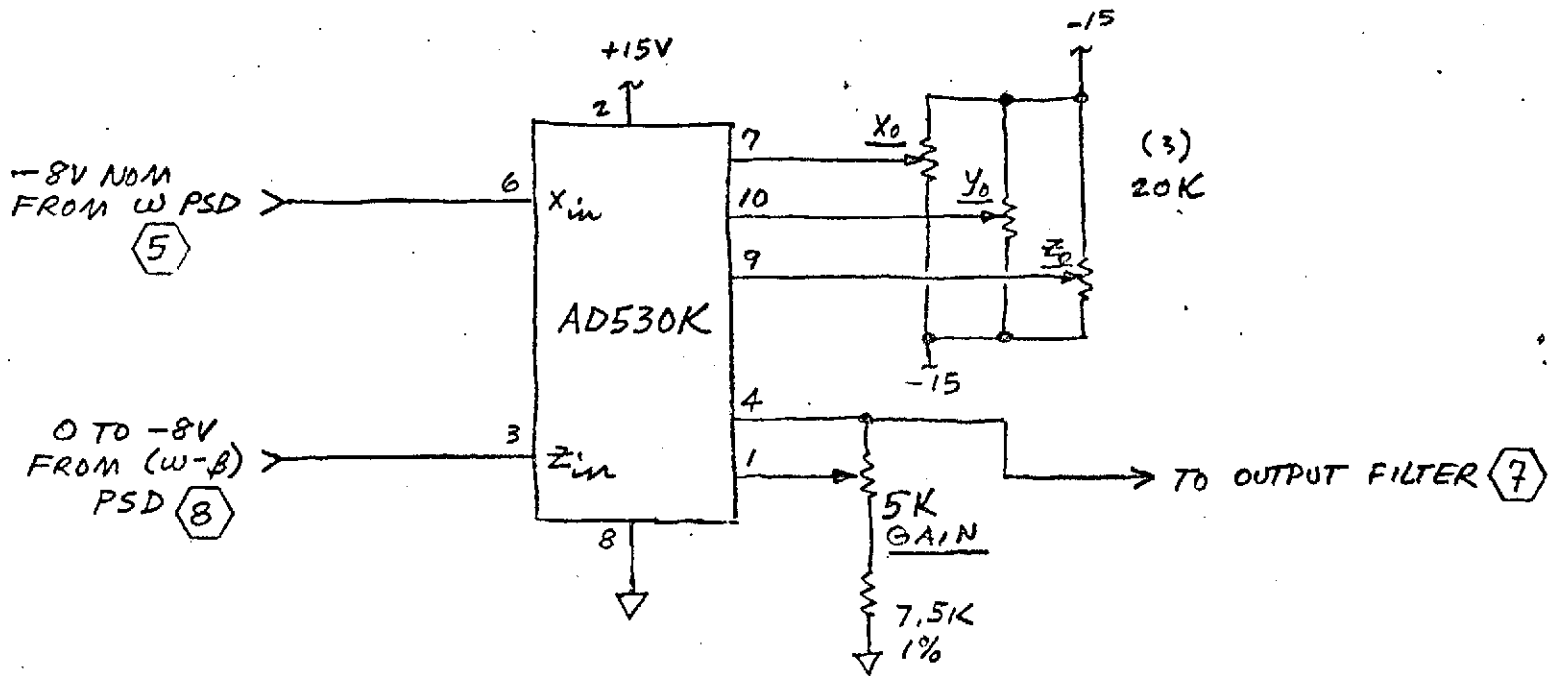


Figure 3.6. Analog Divider - (6)

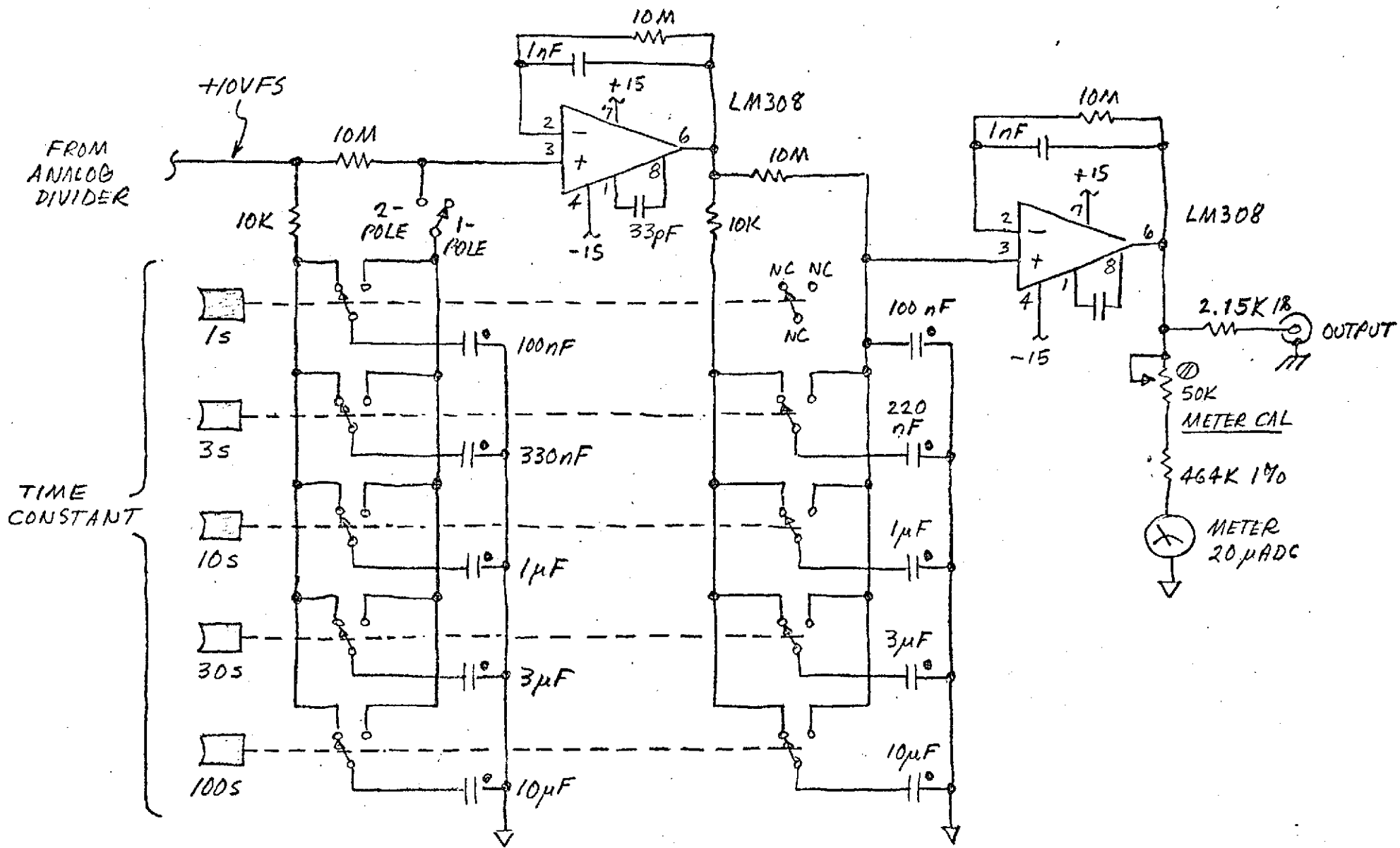


Figure 3.7. Output Filter - 7

given by

$$(1) \text{ ENBW} = \frac{1}{2NT} \quad \text{where } N = \text{the number of poles and} \\ \tau \text{ is the filter time constant.}$$

The time responses for one- and two-pole filters are

$$(2) \frac{v(t)}{v_{\text{final}}} = 1 - e^{-t/\tau} \quad (1\text{-pole})$$

$$(3) \frac{v(t)}{v_{\text{final}}} = 1 - \left(1 + \frac{t}{\tau}\right) e^{-\frac{t}{\tau}}$$

The solutions for these to the 90% response point are

$$(4) t_{90\%} = 2.303\tau \quad (1\text{-pole})$$

$$(5) t_{90\%} = 3.89\tau \quad (2\text{-pole})$$

Now, if one specifies a certain noise bandwidth, by (1), it can be obtained with a 2-pole filter of 1/2 the time constant of a 1-pole. Consequently the time to 90% will be

$$(6) 3.89\frac{\tau}{2} = \text{and the ratio of response times of 2-pole vs} \\ \text{1-pole filters having identical ENBW will be}$$

$$(7) \frac{\tau_{2\text{-pole}}}{\tau_{1\text{-pole}}} = \frac{3.89\frac{\tau}{2}}{2.303\tau} = \frac{3.89}{2 \times 2.303} = 0.844.$$

Thus a somewhat better tradeoff of speed vs noise is obtained with the 2-pole filter. It is interesting that the same total capacitance is required in either case.

The 2-pole filter has a more nearly linear rise, which is desirable from a human-factors viewpoint where long time-constants are involved. It also reduces needle-dance and produces a better appearing recorder trace, since the faster rolloff removes the higher frequency noise components more completely.

As a consequence of these virtues, the second pole was added and the entire filter relocated to follow the divider. Both PSDs preceding the divider have subordinate filters of three poles each, set somewhat faster than the fastest main time constant.

3.8 ω PSD - Block , Figure 3.8

Like the ω - β PSD described above, this section was revised to incorporate the same improvements. In addition, however, a remotely switched and trimmable gain change network was included to bring the output to -8V in all modes. This was done to keep DC gains down and the divider inputs up for maximum stability.

The ω PSD, with much better input S/N ratio than its ω - β cousin, operated properly at the low design DC gain of 2 and remained in that configuration. No further difficulty was encountered.

3.9 Modulator - Block , Figure 3.9

It is the purpose of the modulators to drive the sample and reference cavities in a self-resonant mode, rather like a crystal or tuning fork oscillator. Each pressure modulator also provides a reference signal to the synthesizer, Block 10. Each modulator consists of a pressure transducer (to sense the pressure fluctuations in the cavities) in a regenerative closed loop with the Helmholtz acoustic tank constituting the resonant element.

In original form, the modulator was configured as a "Type A" (i.e., operated to maintain the pressure transducer signal constant). As a consequence of considerable difficulty with this method, an expedient--but not necessarily optimum--fix was to convert to a "Type B" modulator, defined as one in which the pressure transducer signal merely synchronizes the power amplifier which in turn drives the voice coil at regulated constant amplitude. The Type B modulator is depicted in Figure 3.9.

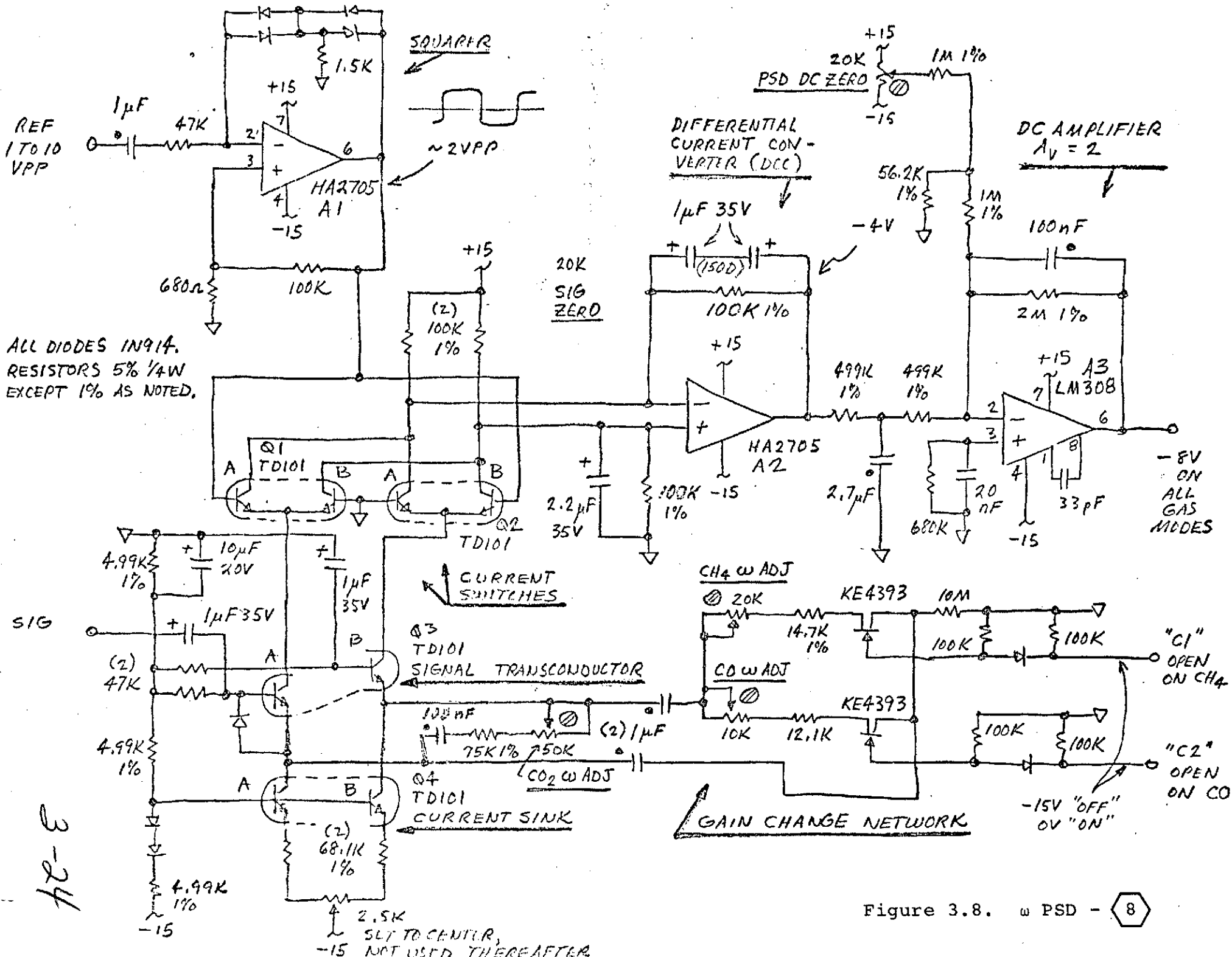
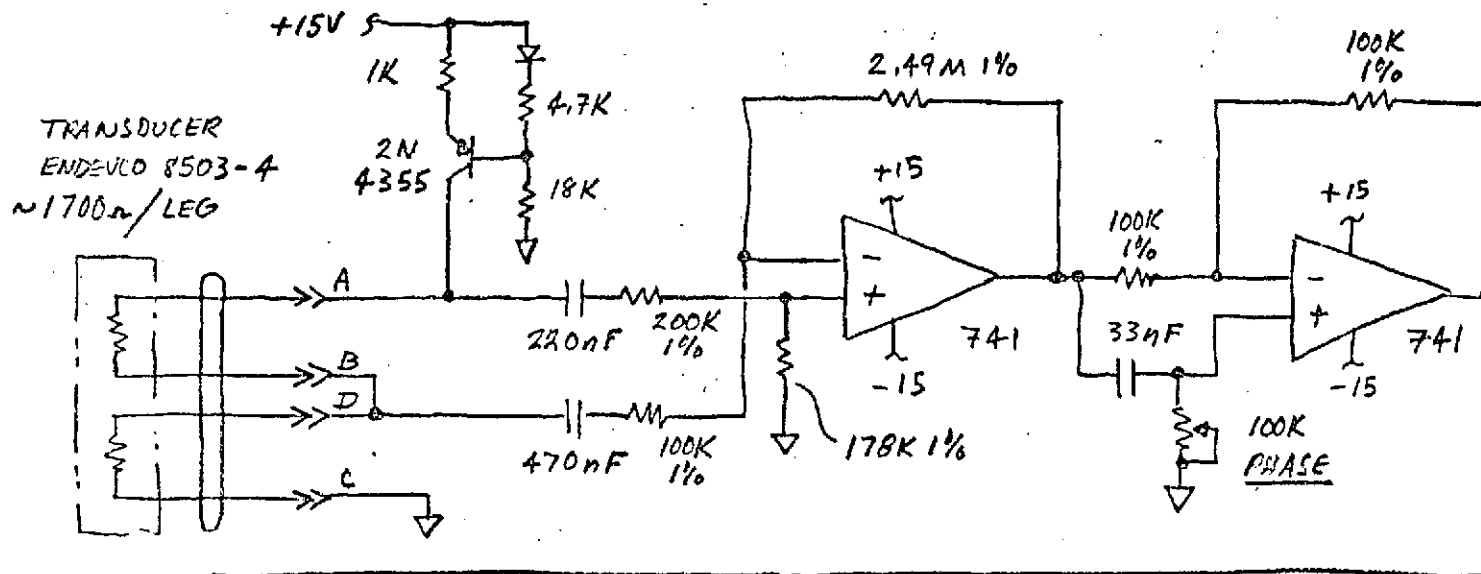


Figure 3.8. ω PSD - 8



NOTES
1. DIODES 1N914 UOS

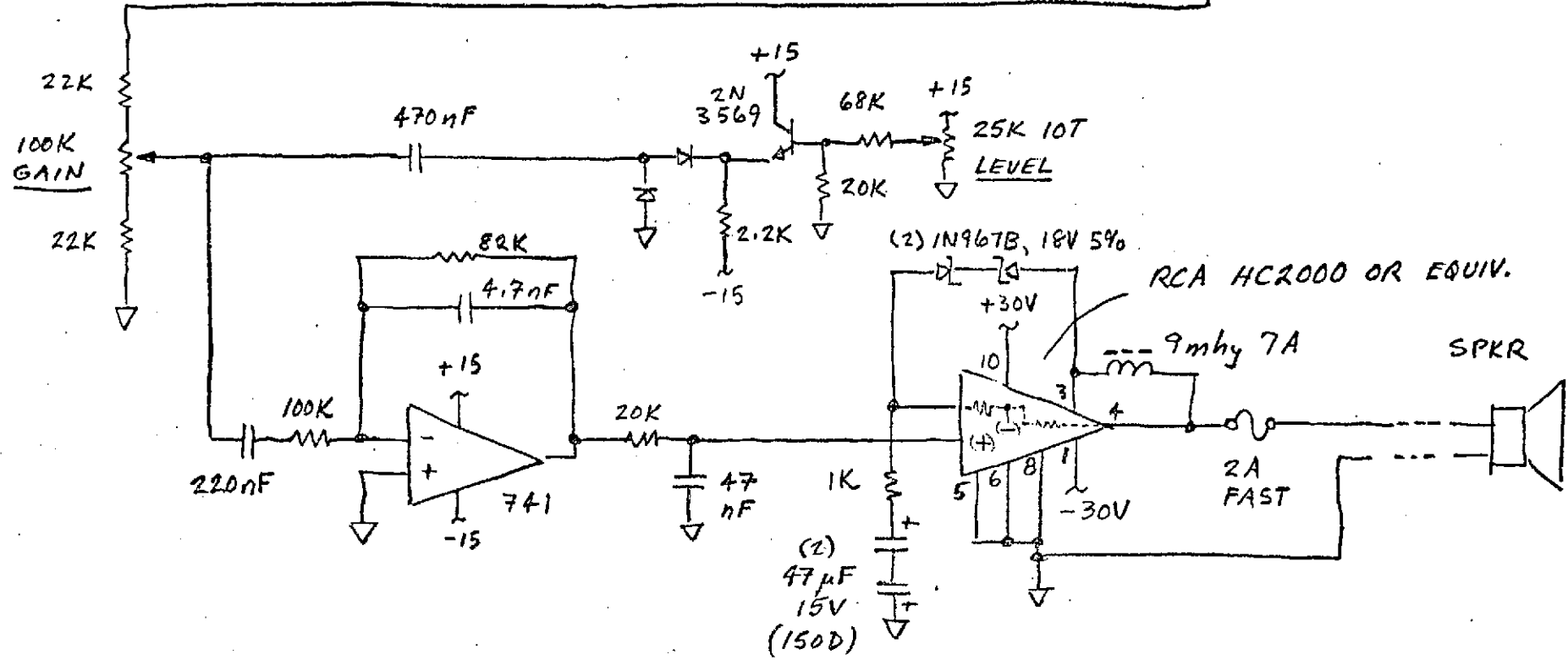


Figure 3.9. Modulator - 9

Difficulties encountered with the Type A circuit were:

1. tendency to be unstable
2. tendency to resonate at the 6Khz transducer natural frequency
3. tendency, after being set up on one gas mixture, to not work at different gas densities.

Analysis of the original configuration reveals the following:

1. There does not appear to be any zero in the transfer function. A properly located low frequency dominant pole with a damping zero somewhat higher is probably essential to loop stability.
2. The possibility of interaction between the rectifier-filter and the AGC'd amplifier due to non-optimum filtering should be investigated.
3. Control of transducer natural frequency is marginal and bears investigation.
4. The Type A system operates by applying to the voice coil an amplified replica of the transducer signal. This signal is rather noisy, however, and the likelihood that this noise, applied to the drivers, introduces added system noise must be considered.
5. Diode 1N914, as well as the zener bridge supply, appear to introduce an uncompensated temperature coefficient of drive amplitude. It remains to be seen whether this effect would be adequately cancelled by tracking of the other modulator.

On the other hand, the presently fitted Type B system:

1. may not hold the pressure excursion constant due to changes in the Helmholtz transfer function caused by temperature, density, unknown stability of the driver, etc.;
2. still introduces system noise greater than the detector noise circuit.

System noise contributed by the modulator/driver/cavity is not well understood at this time. Any noise which would affect system behavior would have to be within sideband frequencies $(\omega + \Delta f)$ and/or $(\beta + \Delta f)$ and/or direct frequency $(\omega - \beta) + \Delta f$ where Δf is the system bandwidth (see Section 7).

Attempts to measure modulator noise were unsuccessful, since the noise component intensities are very far below the fundamental. The best tool for assessing modulator noise performance is probably the heterodyne analyzer itself.

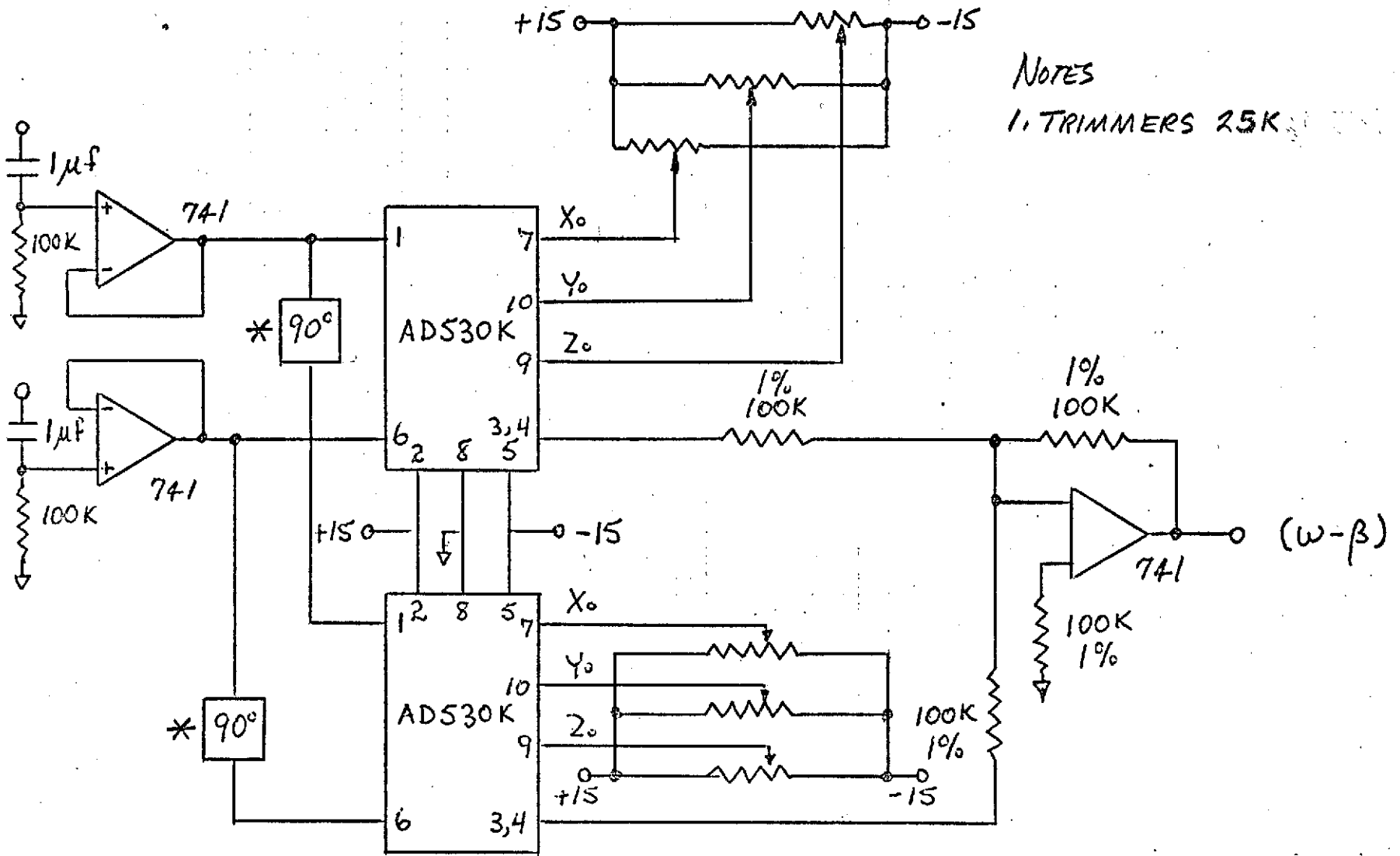
The questions of driver noise and stability are important. We do not feel that either is resolved to full satisfaction. We feel a promising design might employ an independent voltage controlled oscillator having very low phase and amplitude noise and high stability (IC devices of such characteristics are newly available), in a phase-locked and AGC'd control servo, carefully designed to minimize noise and jitter.

3.10 $\omega - \beta$ Synthesizer - Block , Figure 3.10

The synthesizer consists of two multipliers, two 90° phase shifters, and a summing amplifier to execute the following operation:

$$\begin{aligned}
 \cos(\omega - \beta) &= 1/2 [\cos(\omega - \beta) - \cos(\omega + \beta)] \\
 &+ 1/2 [\cos(\omega - \beta) + \cos(\omega + \beta)] \\
 &= \sin\omega t \sin\beta t + \sin(\omega t + \frac{\pi}{2}) \sin(\beta t + \frac{\pi}{2}) \\
 &= \sin\omega t \sin\beta t + \cos\omega t \cos\beta t.
 \end{aligned}$$

When the inputs are $\sin\omega t$ and $\sin\beta t$, the output is $\cos(\omega - \beta)$.



NOTES
 1. TRIMMERS 25K

* SEE SHT. 2

Figure 3.10a. $w-\beta$ Synthesizer - 10 (Sheet 1 of 2)

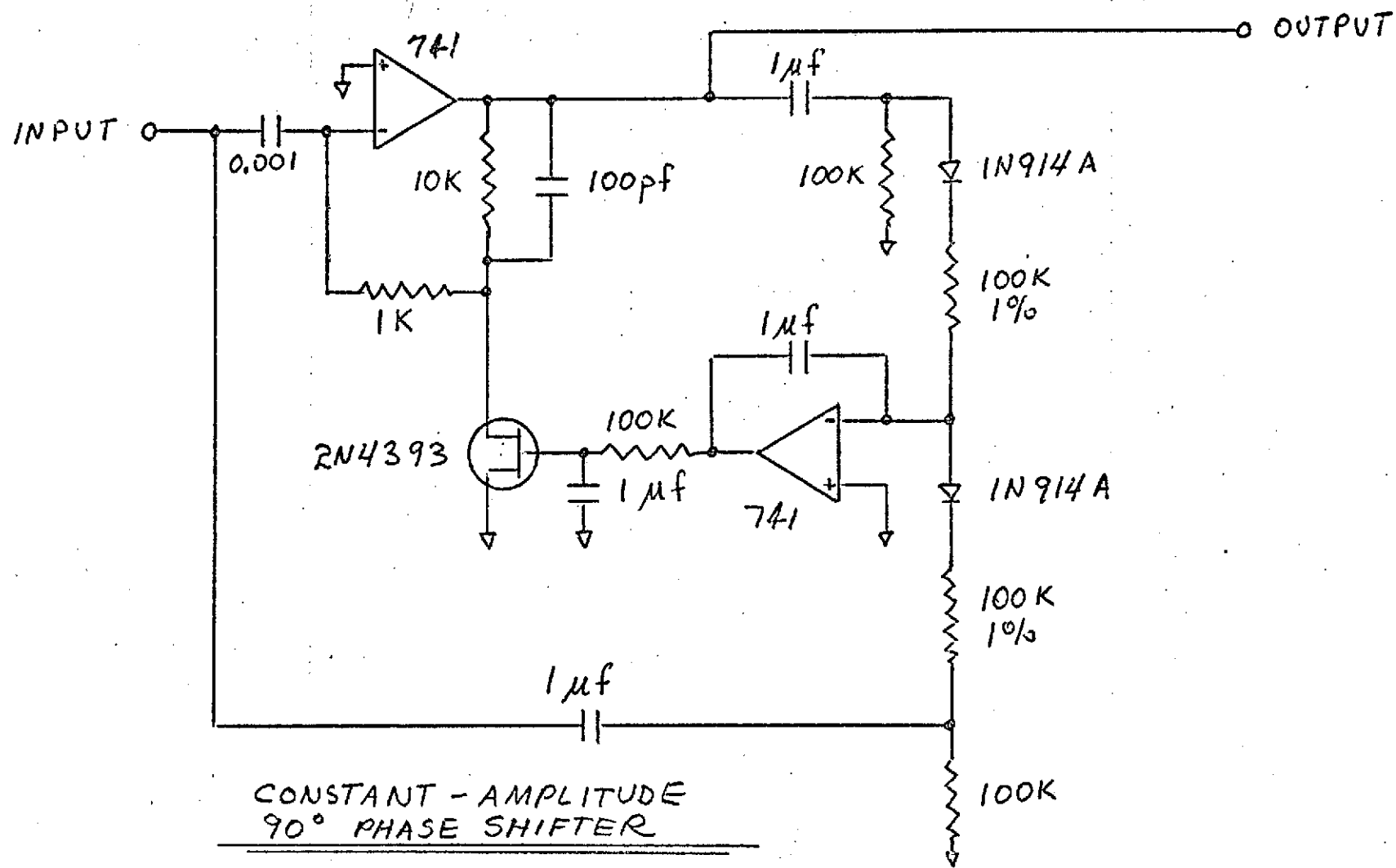


Figure 3.10b. ω - β Synthesizer - 10 (Sheet 2 of 2)

Summing the two bracketed terms theoretically removes all $(\omega+\beta)$ signal, and in practice will remove most of it. The 8-pole LPF which follows will remove any residual $(\omega+\beta)$ signal, and also aids in tracking the identically filtered signal channel to compensate for temperature effects of phase and for frequency changes.

During the course of our work, no changes were made to the synthesizer. In reflection, though, it may be feasible to greatly simplify the circuit. Since the LPF is needed just to track the signal channel and since it is also a strong eliminator of $(\omega+\beta)$, it should be perfectly possible to use just one multiplier to generate simply

$$\sin\omega t \sin\beta t = 1/2 [\cos(\omega-\beta) - \cos(\omega+\beta)]$$

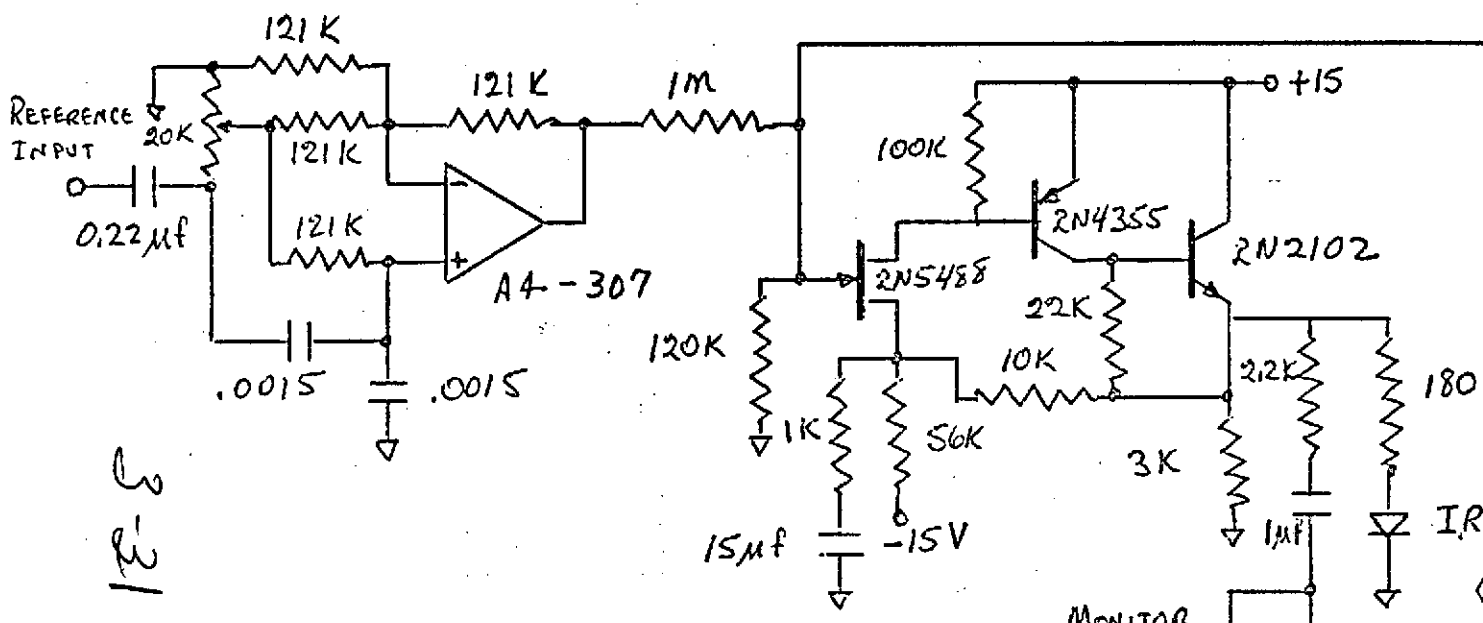
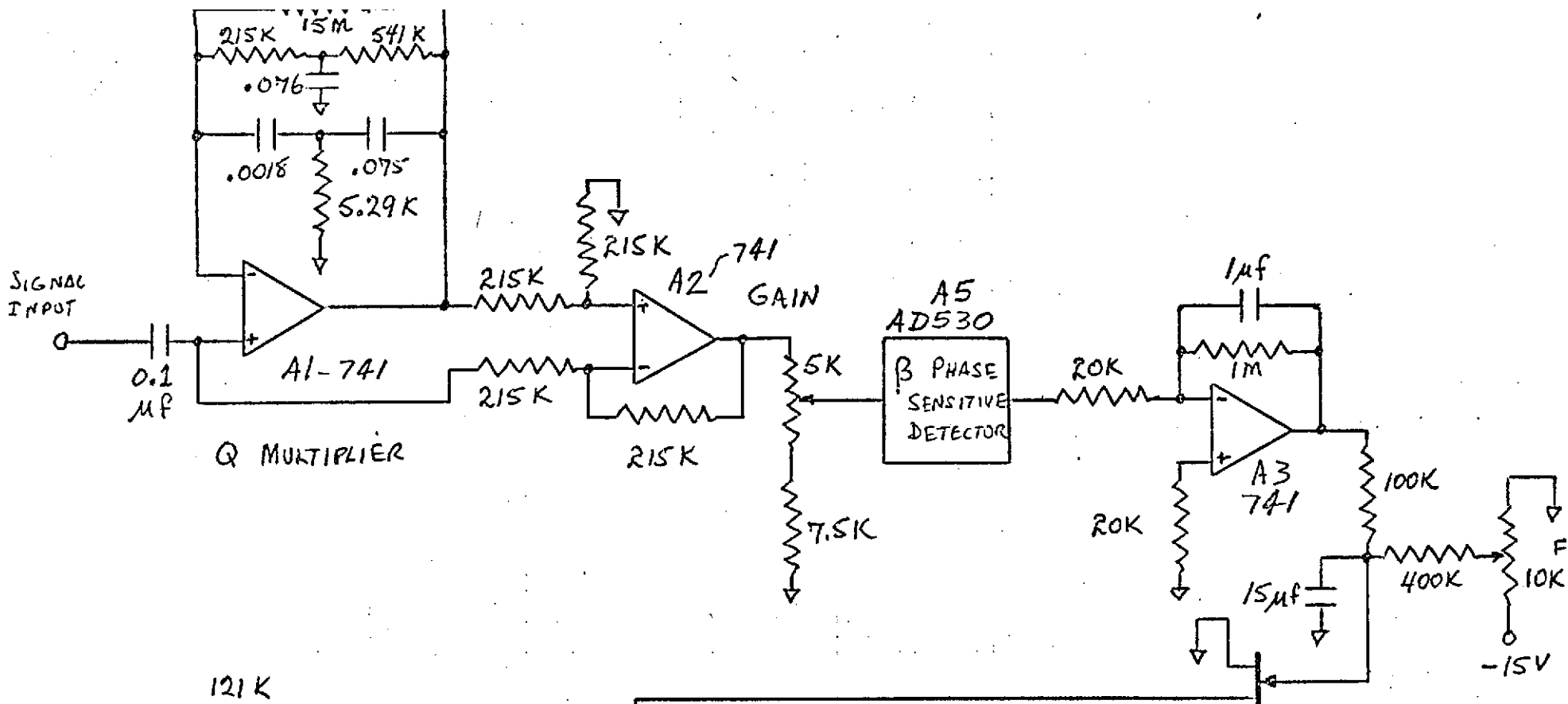
The $1/2\cos(\omega+\beta)$ term would be removed adequately by the LPF, leaving $1/2\cos(\omega-\beta)$.

This simplification would eliminate one of two multipliers, both (complex) constant-amplitude 90° phase shifters, and the summing amplifier, reducing the cost by approximately 70%. It is also possible to eliminate the input amplifiers, leaving nothing but a single multiplier.

3.11 β Carrier Suppression Servo - Block 11, Figure 3.11

The theory and results of this technique are described elsewhere in this report. Operation of this circuit is briefly described here.

The signal from the line receiver (2) is applied to bandpass amplifier A1, set to pass only β . This is then synchronously demodulated by A5, which is a multiplier which takes the product of the β signal from the preamp and the β reference from the β modulator:



NOTES

1.

IR. L.E.D. TYPE S

Ⓜ β CARRIER SUPPRESSION SERVO

SK 256



Figure 3.11. β Carrier Suppression Servo - Ⓜ

MONITOR L.E.D. MV60 or CE 5110
1N914

6
10


$$\begin{aligned}
A_1 \cos \beta t \cdot A_2 \cos t &= A_1 A_2 \cos^2 \beta t \\
&= \frac{A_1 A_2}{2} (1 + \cos 2x) \\
&= \frac{A_1 A_2}{2} + (\text{AC term})
\end{aligned}$$

The AC term is removed by integrator A3, the remaining DC term $\frac{A_1 A_2}{2}$ is compared with an adjustable zero reference. The error voltage thus generated drives a voltage controlled variable voltage divider, adjusting the signal from the β reference channel to a level that will cause the error voltage to seek null. The phase shifter permits optimization of the null. By this method, the β signal reaching the detector can be maintained at or near zero.

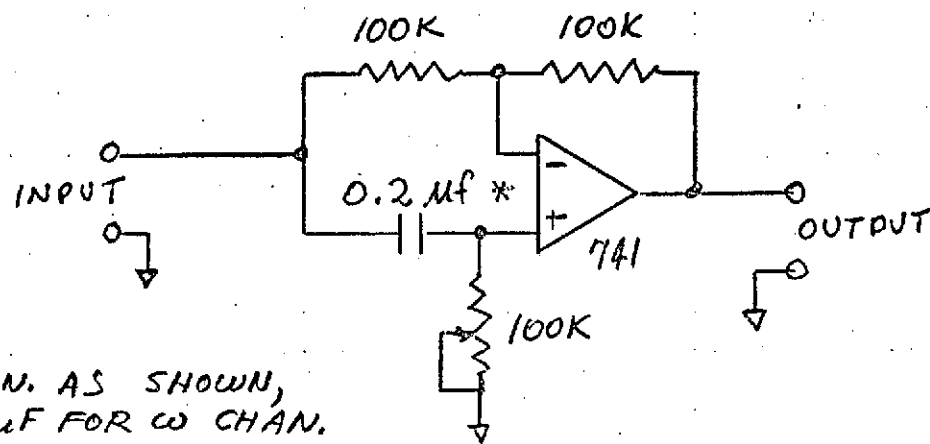
3.12 and 3.13 ω and β Reference Channel - Blocks  and , Figures 3.12 and 3.13

Strictly speaking, the "reference channel" extends from the reference output of each modulator to and including the squaring amplifier in each PSD. Since some of those elements are covered elsewhere, only the phase shifter remains to be described.

This is a conventional constant amplitude circuit which theoretically can cover 0 to 180° but, in practice, can only get to within a few degrees of these extremes. One is used in each PSD (ω - β , and ω) to align the reference with the signal for maximum PSD signal recovery.

3.14 Cooler Servo - Block , Figure 3.14

In order to enhance the PbSe detector S/N ratio, cooling is necessary. This is done by a commercially available thermoelectric (Peltier) heat pump which can reach around -30C from ambients of +50C with application of four amps at 1.2 volts.



* (ω - β) CHAN. AS SHOWN,
 0.047 μ F FOR ω CHAN.

CONSTANT-AMPLITUDE
0-180° PHASE SHIFTER

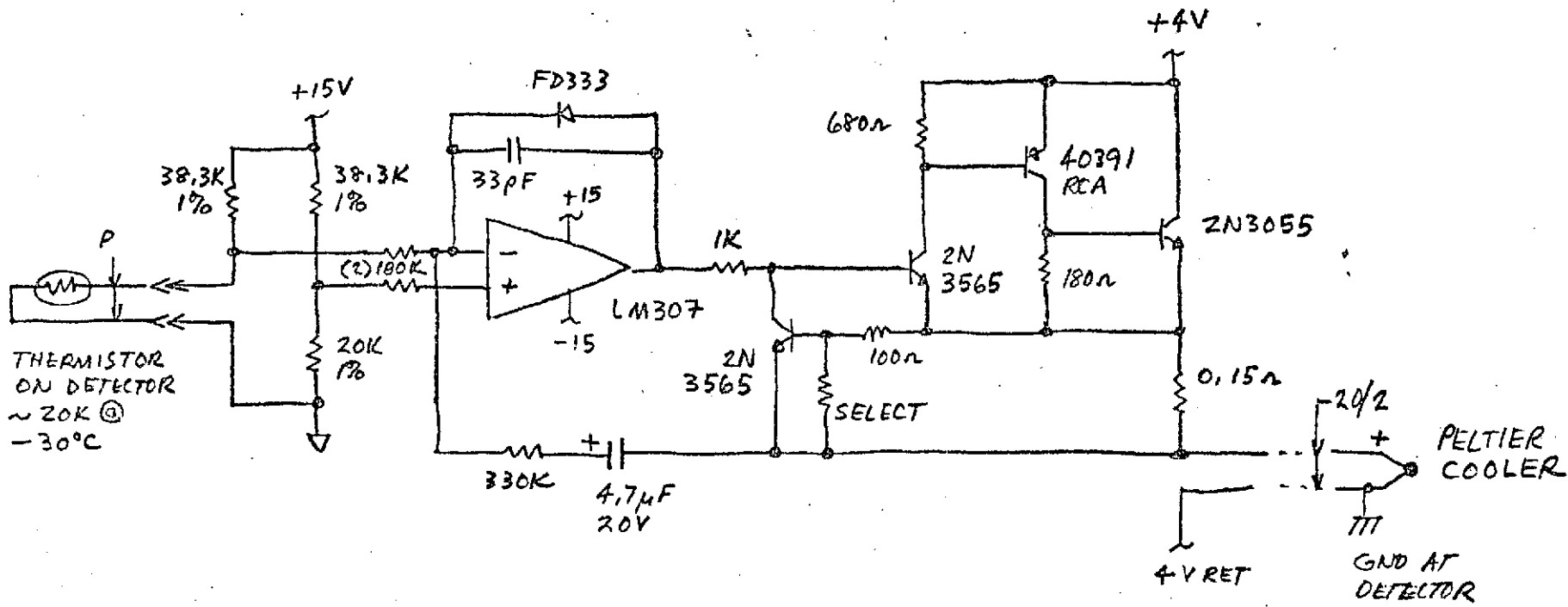


Figure 3.14. Cooler Servo - 14

While maximum S/N would result from maximum cooling, there are practical reasons that dictate regulation at some temperature higher than the minimum achievable. These reasons include elimination of ripple and of disruptively large DC changes at the detector as the temperature (unregulated) changes. Both short and long term changes in signal level also complicate span stabilization of the instrument. Finally, ripple and fluctuating signal make study of the system very difficult.

Regulation is achieved by a closed loop controller with a thermistor sensing element mounted on the cooler's cold (regulated) surface. This circuit is straightforward, employing an opamp plus current boosting transistors. An ordinary pole-zero network insures stable loop dynamics.

The original circuit was replaced with the one shown to

- a. achieve isolation from the IR source power supply,
- b. permit grounding the cooler at the detector housing, which is imperative in controlling serious line ripple in the detector signal, and
- c. isolate the cooler high current circuit from 15V return (common), also imperative to prevent troublesome return circuit difficulties.

3.15 Filter Wheel Controller - Block , Figure 3.15

Selection of gas mode is accomplished by changing the spectral region seen by the detector. This is done by bandpass interference filters, one for each gas, mounted on a moveable wheel which is positioned in response to the gase selected.

Operation is straightforward. Actuation of the gas mode switch causes the drive motor to run ahead until coincidence is indicated by followup switches, whereupon the logic commands the motor to stop.

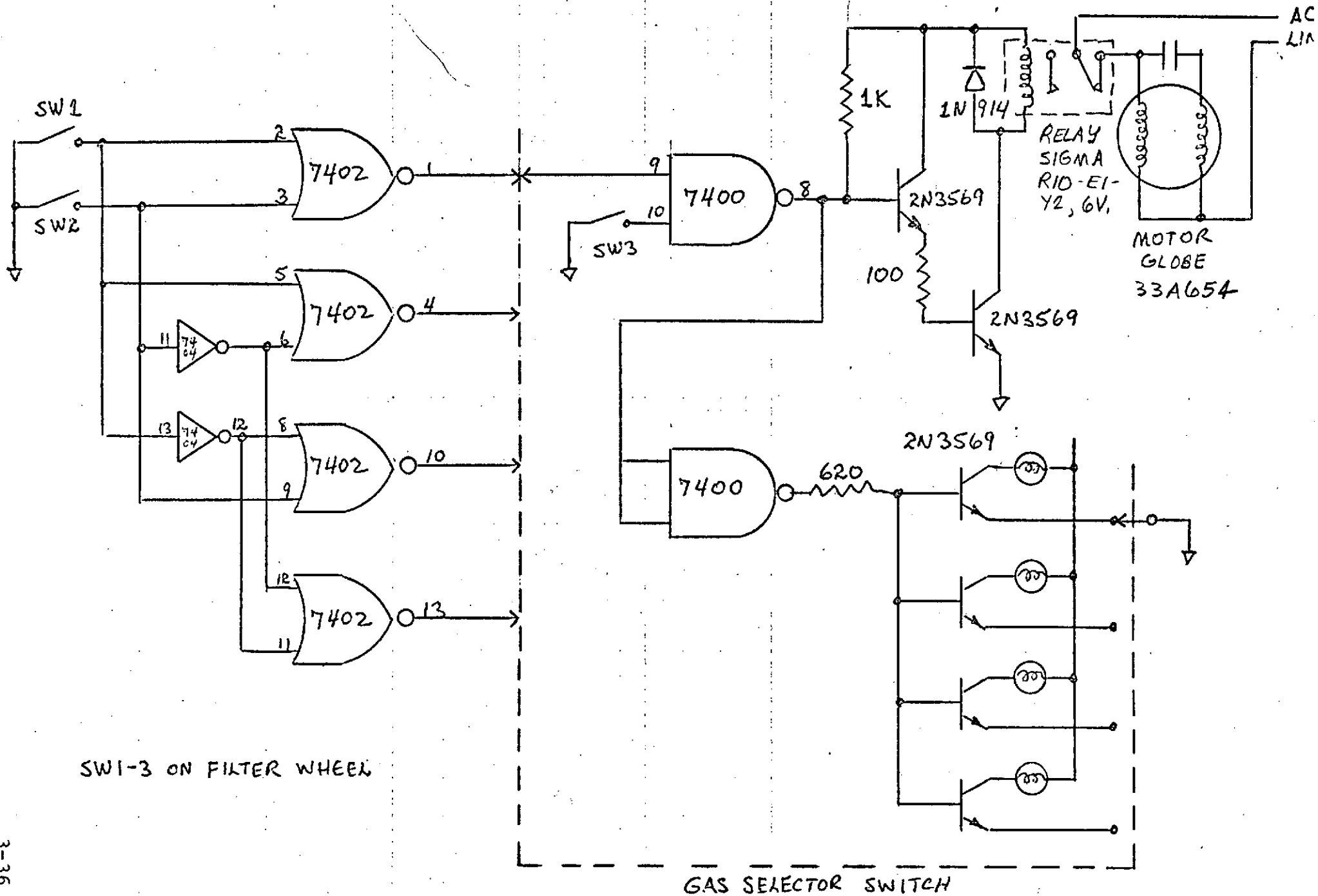


Figure 3.15. Filter Wheel Controller - 15

3.16 Power and Grounding

Part of the later effort in the program centered on cleaning up the analyzer's power and ground systems. This was mandated when we revised the range scheme, placing nearly all gain in the AC signal channel. Some of this work has been touched on in the sections above. This section will treat the matter from an overall viewpoint.

The system always had 60 hz present in the output of the preamp, corresponding in magnitude to about 50 ppm CO₂. Although quite large, this interference had not directly disturbed the system.

When the signal channel modifications were installed, however, the increased AC gain brought the 60 hz content up to such high levels that circuits became swamped by the noise. This was investigated, with the following results:

1. A ground loop involving the preamp, the preamp shield return, cooler return, and 15V return was identified and cleaned up by:
 - a. placing the preamp on a separate +15V supply and grounding that 15V Ret at the preamp front end;
 - b. bonding optical structure to the rest of the instrument structure;
 - c. inserting a differential line receiver at the receiving end of the preamp output cable;
 - d. changing the preamp output coax line to a 2-wire balanced line with shield grounded at both ends;
 - e. grounding the remaining (main) 15V Ret bus in the electronics bay (left side door).
2. With this accomplished, we had reduced the 60 hz noise by a factor of 20. Still, enough remained to be of concern, and there were "birdies" (line-synchronous spikes and ringing) through the rest of the electronics.

Since we measured different amounts and types of noise at opposite ends of the same piece of coax, it was apparent that ground problems still existed in the electronics bay:

- a. we had grounded the main 15V Ret at the line receiver. This was found unsatisfactory; this ground was lifted and the existing 15V Ret central distribution point was grounded instead.
- b. Remember that the ω - β signal at the line receiver is very small. Therefore even the slightest return-bus differentials would be significant. To eliminate all remaining traces of ground noise, we powered the line receiver and LPF together from the +15V rails, decoupled not relative to ground, as they were, but to local signal return. Then, a single coax line carried the LPF output to the postamplifier. In this case, it was desirable to use the shield to carry signal return and 15V (DC) return. Since the ground had been broken, and since that coax carried no other returns, no unwanted currents could flow in the shield that might produce noise. This connection is shown in the Block 2 schematic.

Except for this coax, whose shield was a current-carrying return, all other shields throughout the ω - β signal channel were connected to ground and carried no current. Signal return paths are along the 15V Ret dist. bus.

With this done, no 60 hz or "birdies" could be found anywhere in the signal channel, except for a negligible amount observed with the sample pump running.

4. PERFORMANCE CHARACTERISTICS OF THE MULTIGAS ANALYZER

4.1 Instrument Controls

This section describes the function of the front and back panel and internal controls of the breadboard 3-gas heterodyne analyzer, delivered as an end item to NASA.

Front Panel:

- a. PWR. Power for instrument, with exception of sample pump.
- b. PUMP. Turns sample pump on. Will come on even if power is turned off.
- c. GAS. These switches have two functions:
 1. Position filter wheel in correct position.
 2. Change gains in signal processing circuits.
- d. TIME CONSTANT. Time constant on output of system. Two-pole filter with time constants indicated, with exception of 1 sec position - it is considerably shorter than 1 sec.
- e. RANGE. Changes gain in circuitry to correspond to range indicated.
- f. INLET AND OUTLET TO SAMPLING SYSTEM. Flow rate is indicated on meter on front panel. Flow is controlled by constricting the inlet, or by adjusting valve inside instrument. See section on flow rate. Do not constrict outlet (will pressurize sample chamber causing span changes and possible damage).

Back Panel:

There are three binding posts on the back panel. The black one and the adjacent red one are connected to the infrared source. If a separate power supply is used for the source, it should be connected here. If the internal power supply is used, the two red binding posts should be connected together.

Side Panel (Internal):

Switches: Drivers - Opens circuits to acoustic drivers, thereby stopping the pressure modulation (and also all reference signals).

LED - Opens carrier suppression circuits. Normally open (off).

Potentiometers: ω drive, β drive. Controls AC voltage being applied to acoustic drivers. ω set at 200, β set at 318. See section on instrument noise.

4.2 Gas Flow Rate

In a gas analyzer, the time constant of the processing electronic circuitry and the gas flow rate to effect a complete change of sample gas combine to yield an effective instrumental response time. Figure 4.1 shows the relationship between the sample gas flow rate and the times to change the sample to $(1\frac{1}{e})$ and 90% of a step change in input concentration. The flowmeter on the instrument front panel has a scale of 100% = 3.2 lit/min. The data of Figure 4.1 may be combined with the front panel switchable electronic time constant to estimate the instrumental time response under various conditions. For making dynamic measurements, a flow rate of at least 25% of full scale is recommended. For measurements of stability, or measurements when gas must be conserved, flow rates of 5% of full scale can be used. This is enough flow to keep ambient air from diffusing back into the sample cell.

4.3 Instrument Noise and Sensitivity

There are two basic contributions to the noise of this instrument:

- a. Detector noise. A low noise detector (e.g., #9647-1) with a 1 meg load resistor has a noise level of $\sim 0.4\mu\text{V}/(\text{Hz})^{1/2}$ rms at 100 Hz. In a 10 Hz bandwidth, and

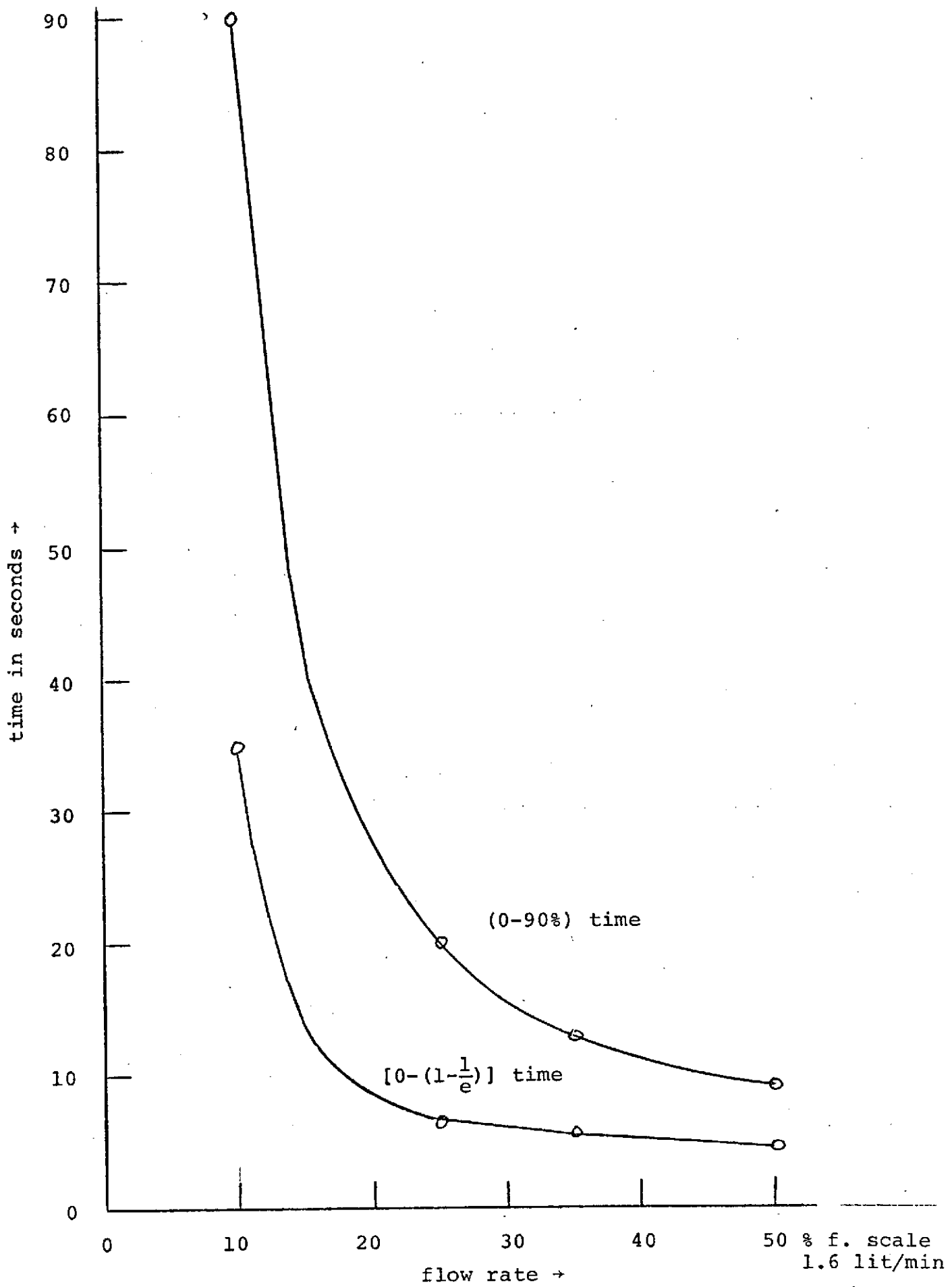


Figure 4.1. Flow rate vs flushing time.

4-3

after a gain of 10 in the preamp, this yields about $13\mu\text{V}$. At 100 Hz we obtain roughly $11\mu\text{V}$ noise in a 10 Hz bandwidth at the output of the preamp as measured with the source off. When the source is turned on, the noise level goes up, more than doubling at 100 Hz when the source is run at 7V, 4A. This behavior could be perhaps explained by photon noise (it is about the correct magnitude); however, the shape of the noise spectrum as shown in Figure 4.2 does not change when the source is on (photon noise presumably gives a flat spectrum). It appears that photon noise is not the cause. The effect has been verified in a completely different test set up (different detector, preamp, source) so it is likely that this noise behavior is inherent in the detector.

Figure 4.3 shows the noise at 100 Hz as a function of the source voltage. Also shown is the magnitude of the ω signal. As can be seen from the figure, even though the noise goes up fairly rapidly with the increasing source voltage, the signal goes up even more rapidly, and the optimum S/N occurs at fairly high source voltage.

- b. Driver noise. If there is noise at 100 Hz on either of the drivers, that noise will give corresponding pressure fluctuations at 100 Hz in the gas. If there is no absorbing gas in the resonator, for instance if it is the sample cell and it is filled with N_2 , then this noise will not be detected by the instrument. However, if there is gas in the resonator, as is the case for the reference cell, then the noise will show up as noise on the output of the detector and will contribute to instrument noise. This contribution should be largest for the gas with the largest ω signal; i.e., CO_2 .

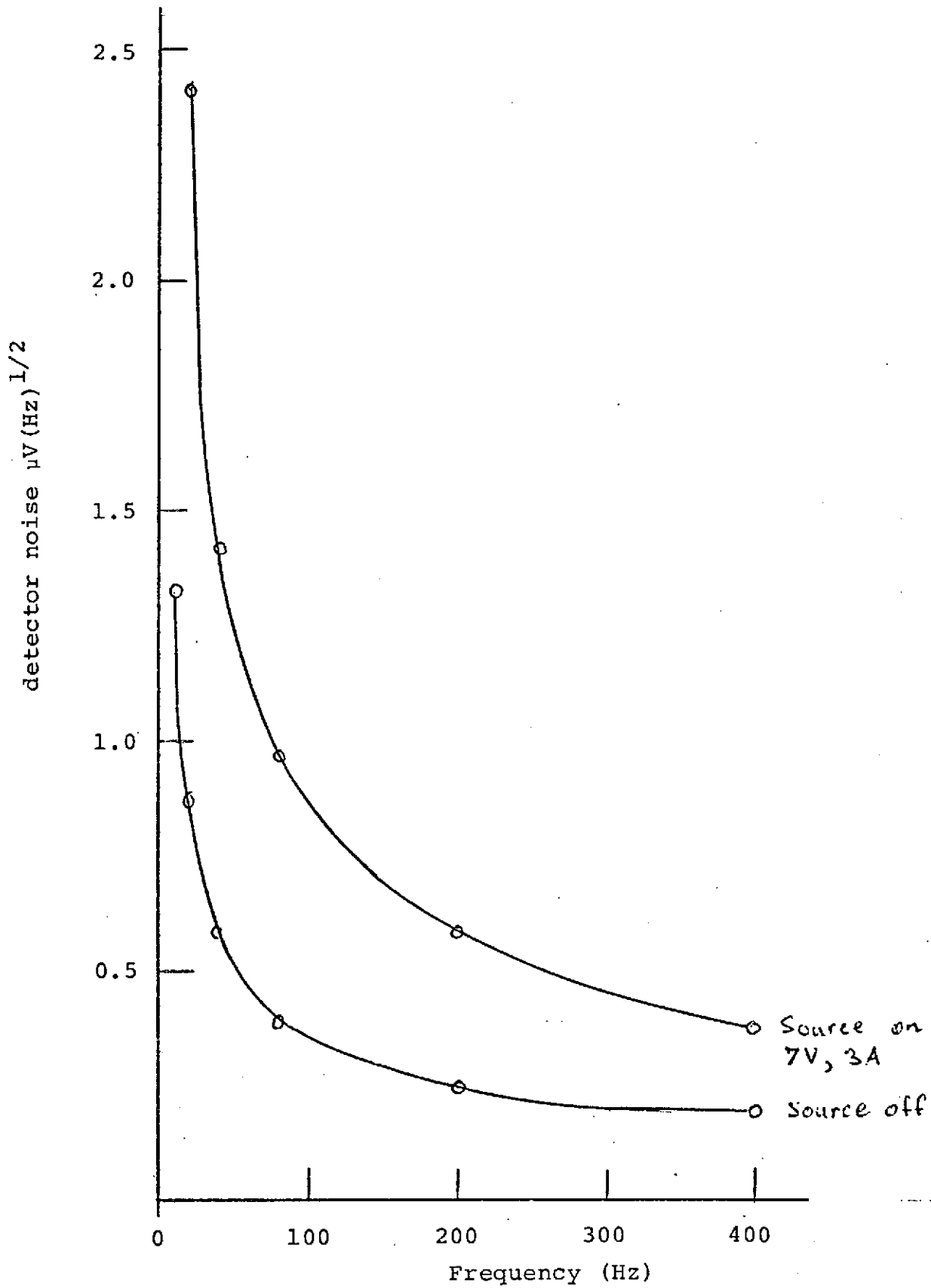


Figure 4.2. Spectral frequency distribution of detector noise for black body source on and off.

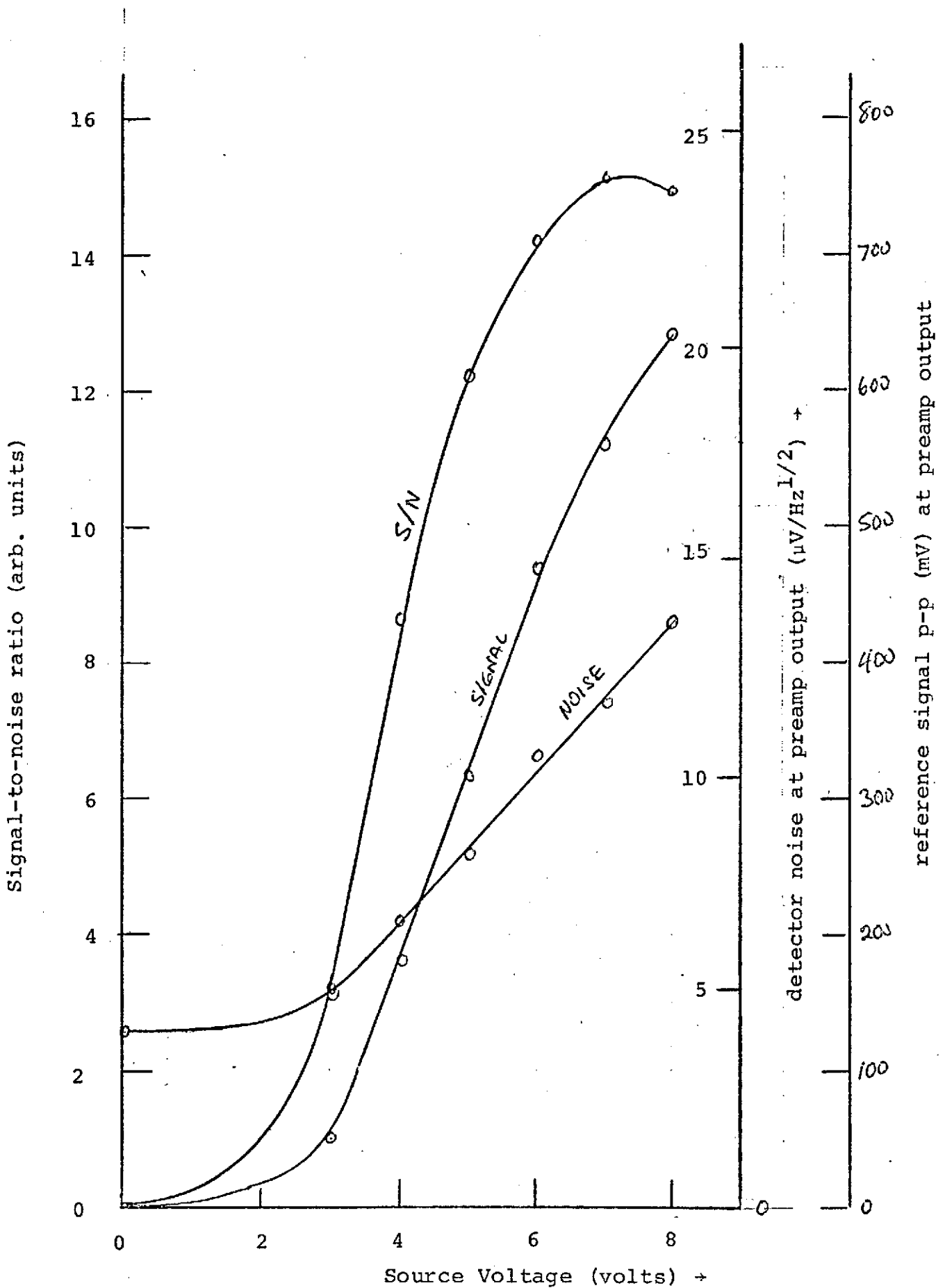


Figure 4.3. Dependence of signal and noise on source voltage.

The noise level in the driver circuit may also depend at what p-p voltage levels the system is operating. Figure 4.4 shows the measured noise for CO and CO₂ as the drive voltage on the ω driver was increased. It is apparent that the ω system is quite noisy as the drive voltage gets up to 30V p-p. This manifests itself in a small increase in the noise for CO, and a large increase in the noise for CO₂, where the ω signal is much larger. Of course, as the drive voltage is increased, the signal also goes up, so what has to be optimized is S/N. Also shown on Figure 4.4 is the S/N for CO₂ and CO (arbitrary scale). It is seen that the S/N optimizes at a much lower driver voltage for CO₂ than for CO. From these curves, and a consideration of the life expectancy of the acoustic drivers, it was decided to run the ω driver at 22V p-p. Since the instrument only sees the effect of this noise if there is of the order of 1% gas in the resonator, noise on the β system does not affect instrument performance. Therefore the β driver is run at a much higher level (36V p-p).

With a 10 sec time constant, and with N₂ in the sample cell, the rms noise for the three gases was measured.

The results:

CO₂ 0.5 ppm rms

CO 5.5 ppm rms

CH₄ 6.7 ppm rms

Conditions: $\tau = 10$ sec

Source - 7V, 4A

ω driver - 22V p-p

β driver - 36V p-p

Reference cell concentrations:

CO₂ 0.5%

CO 1.0%

CH₄ 2.5%

Remainder N₂

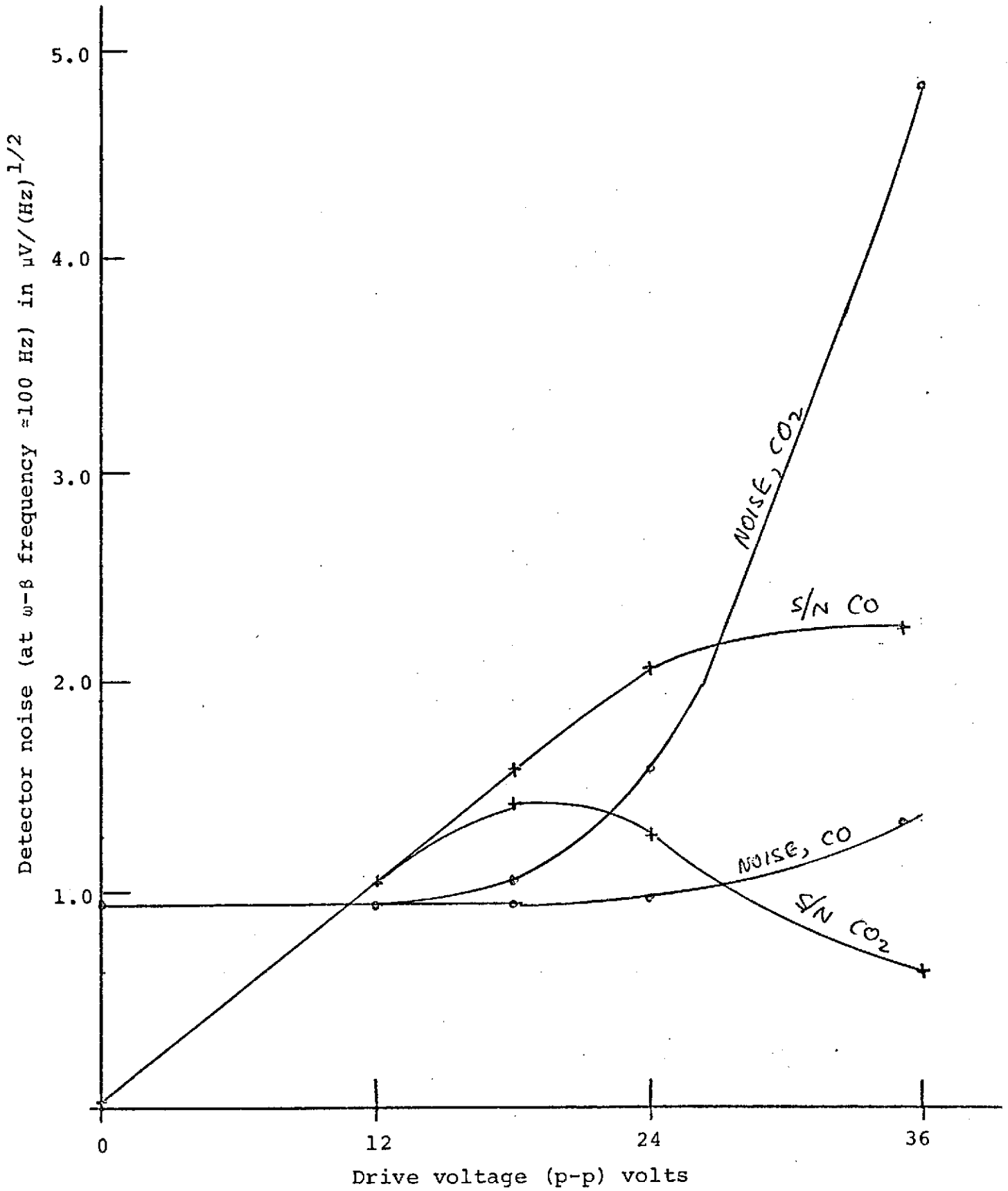


Figure 4.4. Dependence of signal and noise on driver voltage for CO and CO₂

4.4 Instrument Stability

The instrument was run continuously over a weekend and the zero and span readings for the various gases were noted once a day. The instrument was closed up, with 7V @ 4A on the source.

ZERO STABILITY. The measured zero drifts over this period are shown in Figure 4.5.

CH₄ : ± 7 ppm
CO : $< \pm 2$ ppm
CO₂ : $< \pm 1$ ppm

SPAN STABILITY. Figure 4.6 shows the span stability of the instrument. In general, the instrument exhibits a small increase in span reading after turn on, amounting to about 5%. This span change is possibly associated with the warming up of the gas in the reference cell due to heating of the whole optical assembly by the IR source. The warm-up time could possibly be shortened by running the source at lower power levels. After a day's warm-up, the instrument seems to be stable to better than 2% for all gases.

INSTRUMENT RELIABILITY. The instrument was run an average of about 6 hours a day for a month with no failures. It was not subjected to vibration or temperature testing.

4.5 Rejection Ratios

Table 4.1 gives the rejection ratios measured for the instrument. There are three general sources of cross sensitivity. In order of decreasing importance they are:

- i. Inability to completely block off the radiation at the wavelengths corresponding to bands of the interferent molecule. This is a problem because the instrument is actually trying to measure all three gases, CO,

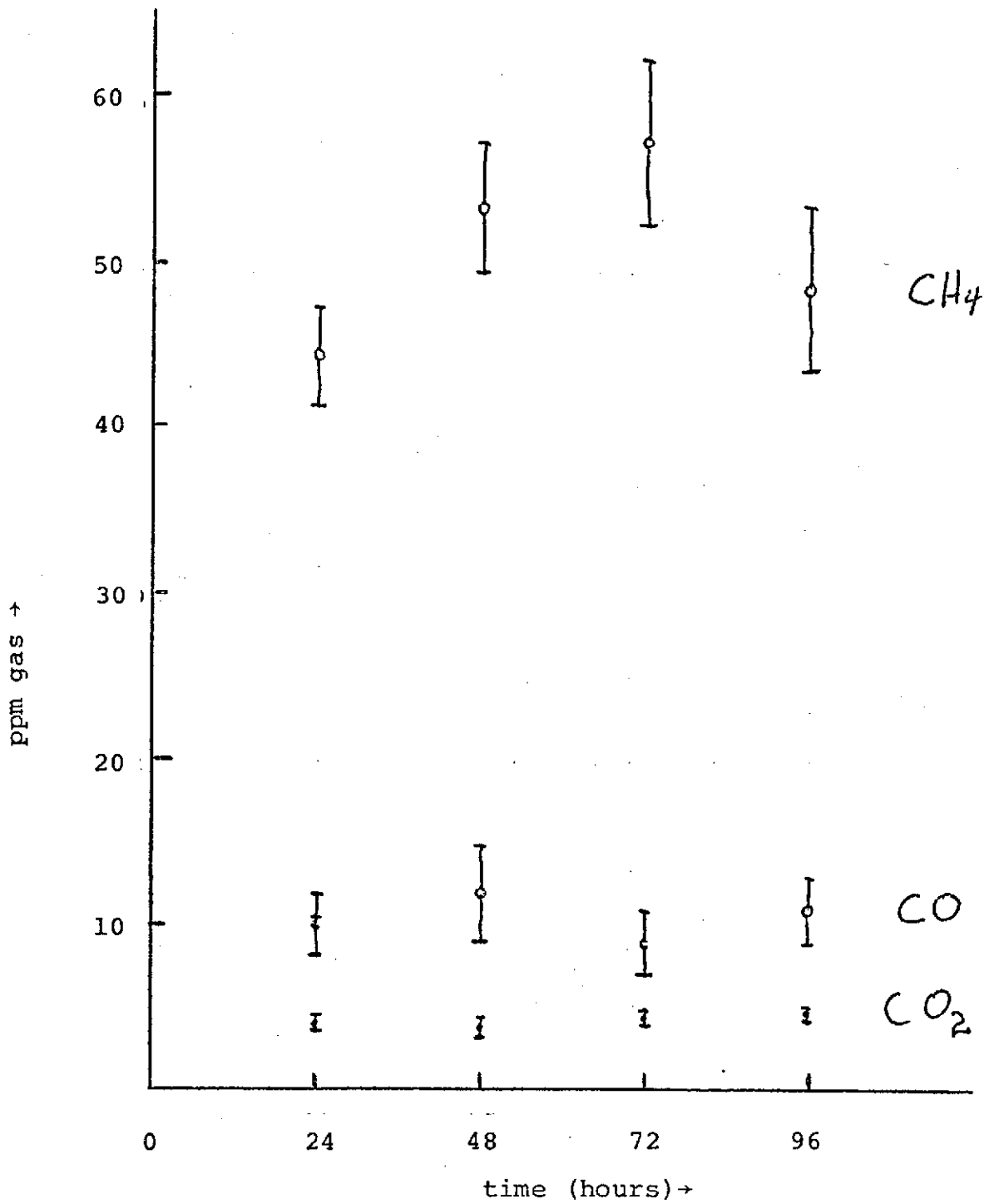


Figure 4.5. Instrument zero stability and offsets.

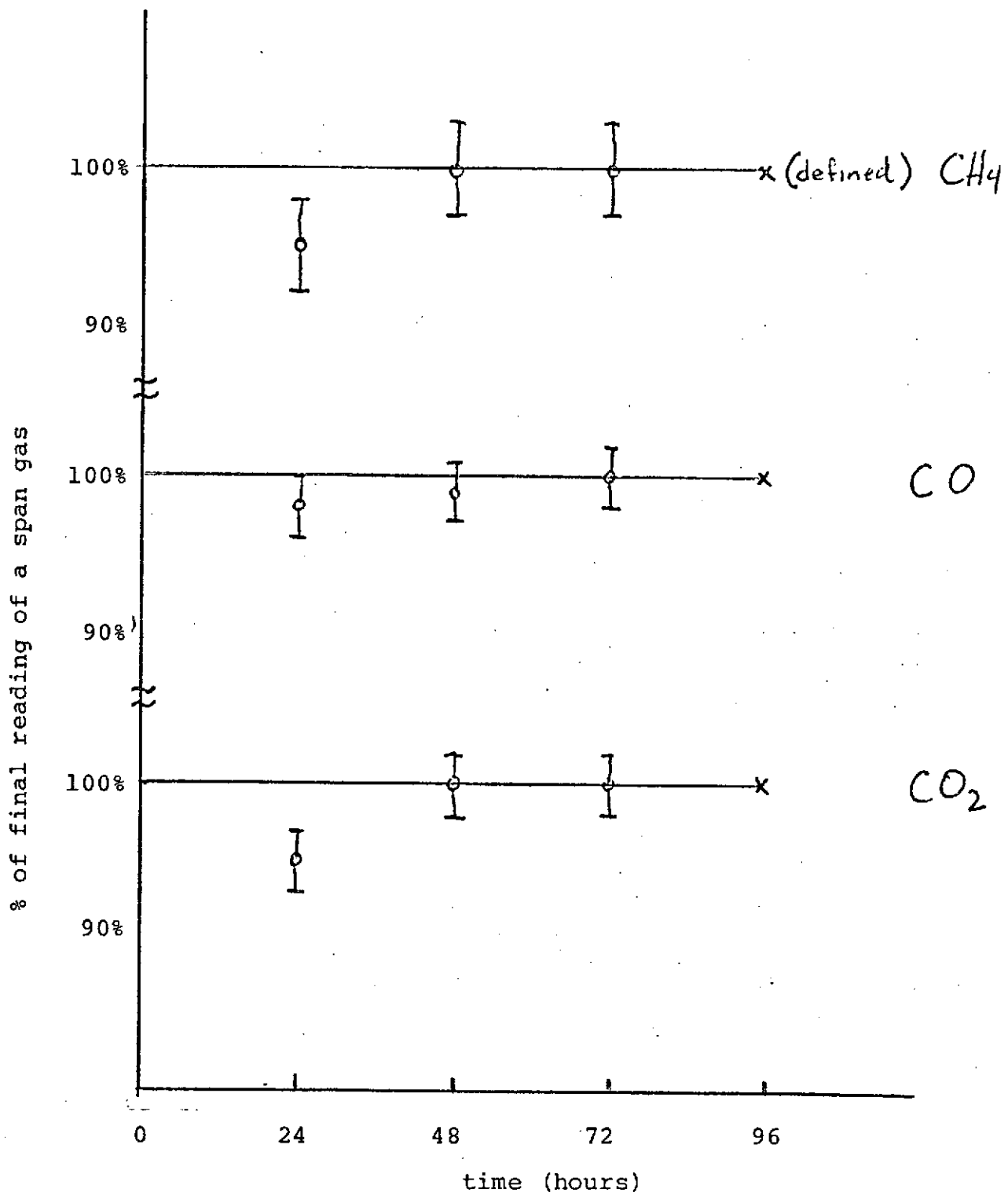


Figure 4.6. Instrument span stability.

CH₄ and CO₂, simultaneously. In order to measure only one, the light at the wavelengths of the other two has to be blocked by interference filters and negative gas filters (in the filter wheel). To the extent that some light gets through (e.g., 1:10⁴) the instrument will have a cross sensitivity to the other gases in the reference cell.

- ii. Mixing of ω (reference) and β (sample) frequencies in the detector because of detector non-linearities. This mixing produces a signal at the frequency $\omega - \beta$ and is detected by the instrument. This problem arises when there is a large amount of absorbing gas in the sample cell (to create a large β signal), but the lines of the gas do not overlap the lines of the gas to be measured. By suppressing one of the signals (i.e., β) the problem is eliminated. The carrier suppression is effected by placing a small light emitting diode in front of the detector and driving it 180° out of phase with the β signal to cancel it out. The instrument is equipped with circuitry to do this; however, since the major source of cross sensitivity is actually i), the carrier suppression circuit is switched off. If there were only a single gas in the reference cell, and improved rejection ratios were desired, then the carrier suppression circuit should be used.
- iii. An actual overlap of lines between different gases. This is not a problem at present with the possible exception of H₂O when measuring CH₄.

The rejection ratios shown in Table 4.1 are quite adequate to accurately measure gas A in the presence of moderately large quantities of gas B. Also, unlike other instruments where the amount

TABLE 4.1

REJECTION RATIOS

Gas to be Measured	Interfering gas				Equivalent Reading 100% humidity 65° F
	CO	CO ₂	CH ₄	H ₂ O	
CO	---	+ 1600	>10,000	2300-∞	3 ± 6 ppm
CO ₂	>60,000	---	+ 50,000	21,000-∞	0.5 ± 0.5 ppm
CH ₄	+ 450	- 3200	---	700-1800	22 ± 10 ppm

Gases used in tests:

CO 2% in N₂
 CO₂ 8% in N₂
 CH₄ 10% in N₂
 H₂O N₂ bubbled through H₂O at 65° F
 ≈ 2.1% H₂O in N₂

of possible interferent gas is unknown, the instrument can very simply measure the amount of interferent to see if it is a potential problem. The instrument shows no measurable response to saturated water vapor on the CO and CO₂ positions. It does give a slight positive response to H₂O when measuring CH₄.

The interference filters used to conduct the rejection ratio tests, which are built into the rotating filter wheel, have characteristics as shown in Table 4.2.

TABLE 4.2

FILTERS USED IN THE HETERODYNE ANALYZER

1.	CO	Filter #21	$\lambda_o = 4.75\mu$	} $\Delta\lambda$ (fwhm) = .16 μ
		Half maxima	λ low = 4.64 μ	
			λ high = 4.82 μ	
		1% points	λ low = 4.54 μ	
λ high = 4.93 μ				
2.	CO ₂	Filter #19	$\lambda_o = 4.30\mu$	} $\Delta\lambda$ (fwhm) = .16 μ
		Half maxima	λ low = 4.17 μ	
			λ high = 4.33 μ	
		1% Points	λ low = 4.10 μ	
λ high = 4.43 μ				
3.	CH ₄	Filter #23	$\lambda_o = 3.38\mu$	} $\Delta\lambda$ (fwhm) = .12 μ
		Half Maxima	λ low = 3.30 μ	
			λ high = 3.42 μ	
		1% Points	λ low = 3.22 μ	
λ high = 3.50 μ				

APPENDIX A

HETERODYNE METHOD FOR HIGH SPECIFICITY GAS DETECTION

Sponsored by —
American Chemical Society (ACS)
American Institute of Aeronautics and Astronautics (AIAA)
Environmental Protection Agency (EPA)
Institute of Electrical & Electronic Engineers (IEEE)
Instrument Society of America (ISA)
National Aeronautics and Space Administration (NASA)
National Oceanographic and Atmospheric Administration (NOAA)

AIAA Paper No. 71-1064

HETERODYNE METHOD FOR HIGH SPECIFICITY GAS DETECTION

by

J. DIMEFF, R. W. DONALDSON, W. D. GUNTER, JR.,

D. N. JAYNES, A. P. MARGOZZI,

and

G. J. DEBOO

NASA Ames Research Center

Moffett Field, California

and

E. A. McCLATCHIE and K. G. WILLIAMS

Arkon Scientific Laboratories

Berkeley, California

Joint Conference on Sensing of Environmental Pollutants

PALO ALTO, CALIFORNIA/NOVEMBER 8-10, 1971

First publication rights reserved by American Institute of Aeronautics and Astronautics.
1290 Avenue of the Americas, New York, N. Y. 10019. Abstracts may be published without
permission if credit is given to author and to AIAA. (Price: AIAA Member \$1.50. Nonmember \$2.00).

Note: This paper available at AIAA New York office for six months;
thereafter, photoprint copies are available at photocopy prices from
AIAA Library, 750 3rd Avenue, New York, New York 10017

A-2

HETERODYNE METHOD FOR HIGH SPECIFICITY GAS DETECTION

John Dimeff, Ralph W. Donaldson, William D. Gunter, Jr.,
Dean N. Jaynes, Angelo P. Margozzi, and Gordon J. Deboo
Ames Research Center, NASA
Moffett Field, California 94035

and

Edward A. McClatchie and Kevin G. Williams
Arkon Scientific Laboratories
930 Dwight Way
Berkeley, California 94710

Abstract

This paper describes a new technique for measuring trace quantities of gases. The technique involves the use of a reference cell (containing a known amount of the gas being sought) and a sample cell (containing an unknown amount of the same gas) wherein the gas densities are modulated. Light passing through the two cells in sequence is modulated in intensity at the vibrational-rotational lines characteristic of the absorption spectrum for the gas of interest. Since the absorption process is nonlinear, modulating the two absorption cells at two different frequencies gives rise to a heterodyning effect, which in turn introduces sum and difference frequencies in the detected signal. Measuring the ratio of the difference frequency signal, for example, to the signal introduced by the reference cell provides a normalized measure of the amount of the gas in the sample cell. The readings produced are thereby independent of source intensity, window transparency, and detector sensitivity.

Experimental evaluation of the technique suggests that it should be applicable to a wide range of gases, that it should be able to reject spurious signals due to unwanted gases, and that it should be sensitive to concentrations of the order of 10^{-8} when used with a sample cell of only 20 cm length.

Introduction

• Various elements of the scientific community are concerned with the characterization of pollutants in the atmosphere, the measurement of contaminant gases in closed life-support systems, and the sensing of physiologically significant gases for health monitoring and diagnosis of disease. The instrumentation problem in each case is fundamentally one of developing a simple instrument that is versatile in that it can be used to measure the several gases of interest; specific in that it does not introduce false readings due to the presence of unknown gases mixed with the gas of interest; simple in its operation and interpretation; and free of such instrument errors as drift, microphonics, and sensitivity shifts. This paper describes a new instrument (based on the principle of absorption-absorption, or emission-absorption heterodyning)* that potentially meets these requirements, and provides some analytical and experimental basis for comparing the new technique with current techniques.

Molecules of interest in pollution studies are typically characterized by a complex vibrational-rotational spectral absorption signature in the region of 2 to 15 μM . The typical absorption spectrum (Fig. 1) extends over a region of 0.3 μM , and includes several individual lines of the order of 2×10^{-4} μM in width, recurring at intervals of approximately 6×10^{-3} μM . The position and the detailed characteristics of these absorption lines form the specific signature that allows spectroscopic identification of the gas of interest. To obtain a measurement with a high confidence level requires that one resolve the individual lines of the spectrum, which in turn requires an instrument with a resolving power, $\lambda/d\lambda$, of the order of 3×10^4 .

Instruments for detecting gases through identification of their spectral absorption characteristics are classified as dispersive instruments or nondispersive instruments. The first category can be divided again into subcategories of those that disperse the spectrum in space (as with the grating or prism spectrograph) and those that disperse the spectrum in time or in the frequency domain (as with the scanning laser analyzer or the scanning or fourier transform interferometers). When these instruments are adapted as high specificity field instruments they typically suffer from some combination of such characteristic deficiencies as excessive size, excessive complexity in processing data, and limited range of spectral coverage. Because of these deficiencies, there has been considerable interest in nondispersive infrared analyzers (NDIR), but they have also had such serious limitations as instabilities introduced by uncontrollable differences in the absorption introduced by the reference beam and by the measuring beam, microphonics associated with the Luft detectors frequently used to obtain sensitivity and specificity, and difficulties in making a single instrument adaptable to the measurement of several gases. The instrument to be described uses an NDIR principle that seems to solve each of these problems.

Description of Principle

Successive attenuation of a beam of optical energy of wavelength λ , by two absorption cells results in a reduction of the intensity of the optical beam in accordance with Beer's law such that

*Technique covered by patent disclosure "Non-dispersive Auto Correlation Gas Analyzer" by John Dimeff, NASA Case ARC 10308-1. Available for licensing under NASA patent regulations.

$$\frac{I_\lambda}{I_{0\lambda}} = \exp - (\Delta_0 + \Delta_1 + \Delta_2) \quad (1)$$

where Δ_0, Δ_1 , and Δ_2 are the combined average attenuation, the dynamically varying attenuation introduced by the first cell, and the dynamically varying attenuation introduced by the second cell, respectively. Expansion of the exponential yields

$$\frac{I_\lambda}{I_{0\lambda}} = \left[1 - (\Delta_1 + \Delta_2) + \frac{(\Delta_1 + \Delta_2)^2}{2!} - \dots \right] e^{-\Delta_0} \quad (2)$$

$$\frac{I_\lambda}{I_{0\lambda}} = \left[1 - (\Delta_1 + \Delta_2) + \frac{1}{2} (\Delta_1^2 + \Delta_2^2 + 2\Delta_1\Delta_2) - \dots \right] e^{-\Delta_0} \quad (3)$$

It is apparent from the product term $\Delta_1 \Delta_2$ in the bracket of Eq. (3) that terms occurring at the sum and difference of the frequencies associated with Δ_1 and Δ_2 will be present, and that if Δ_1 and Δ_2 are sinusoids of amplitude a_1 and a_2 and frequencies ω_1 and ω_2 , respectively, the Fourier component of intensity fluctuation occurring at the heterodyne frequencies ($\omega_1 \pm \omega_2$) will be

$$\left(\frac{I_\lambda}{I_{0\lambda}} \right)_{\omega_1 \pm \omega_2} = \left\{ \frac{a_1 a_2}{2} \left[\cos(\omega_1 - \omega_2)t - \cos(\omega_1 + \omega_2)t \right] \right\} e^{-\Delta_0} \quad (4)$$

If the dynamic component of the intensity is introduced by modulating the density of the gas in the absorbing cells, the coefficients a_1 and a_2 , and the exponent Δ_0 can be expressed in terms of the absorption coefficient, μ , the path length of the individual absorbers, x , the mean density of the gas component used as an absorber, ρ_0 , and the density fluctuation, $\Delta\rho$, by the relationships

$$a = \mu x \Delta\rho \quad \text{and} \quad \Delta_0 = \mu_{01} x_1 \rho_{01} + \mu_{02} x_2 \rho_{02} \quad (5)$$

If, now, one were to detect the intensity with an electronic system responsive only to the component $\omega_1 - \omega_2$, the intensity fluctuation becomes

$$\left(\frac{I_\lambda}{I_{0\lambda}} \right)_{\omega_1 - \omega_2} = \left[\frac{\mu_{01} \mu_{02} x_1 x_2}{2} \Delta\rho_1 \Delta\rho_2 \cos(\omega_1 - \omega_2)t \right] e^{-\Delta_0} \quad (6)$$

While the above analysis is simplified (in that it assumes that μ remains constant during the process of modulating the density, and that the absorption occurs at a single frequency) it suggests the instrument shown conceptually in Fig. 2. The following are some of the advantages of such an instrument.

1. There is a single uninterrupted optical path, thereby eliminating the error introduced by such characteristics of systems using two alternative paths as changes in window transparencies and shutter timing.
2. The energy spectrum (at the mean density) of the interrogating energy (reference cell absorption signature) corresponds identically to the spectral absorption characteristics of the gas being sought, thereby maximizing the signal derived and the specificity of the measurements.
3. Detectors required in the instrument are solid state, thereby avoiding microphonics typical of instruments using Luft-type detectors.
4. The reference cell may be filled with several gases as long as their spectra can be separated by means of interference filters or high absorption gas filters, and independent sequential measurements of the concentration of the various gas components in the unknown sample can be made by sequentially inserting the appropriate filters.
5. The technique should be applicable to a wide variety of gases, particularly for any gases with reasonably complex absorption line structures.
6. Normalizing the output by measuring the ratio $I_{\omega_1 - \omega_2} / I_{\omega_1}$ eliminates drifts and zero shifts due to changes in source intensity, window transparency, thermal distortions of the optical path, changes in detector sensitivity, systematic changes in amplifier gains with changes in line voltage, and changes in transparency of filters used to improve the specificity of the instrument.

Alternative forms of the instrument might involve replacement of the broadband infrared source with a cell containing a fluorescing sample of the gas to be measured, and elimination of the external source and use of the sinusoidal pressure-induced fluorescence in the reference cell as a source of light to transilluminate the gas in the sample cell. While these configurations may have advantages in particular cases, the analytical and experimental information obtained to date has been collected with the configuration shown in Fig. 2. The following sections present a better description of the dynamic absorption process than is given above, and provide data on the sensitivity and cross-sensitivity of an experimental instrument.

Analysis

The absorption coefficient $K_J(\nu)$ of a particular line of the R or P branches with initial rotation quantum number, J , and final rotational quantum number, J' , can be approximated by

$$K_J(\nu) = R \frac{SfB}{\pi\delta kT} \cdot \frac{\delta^2}{(\nu - \nu_{0J})^2 + \delta^2} (J + J' + 1) \cdot J \exp \left[-\frac{BJ(J+1)}{kT} \right] \quad (7)$$

where S is the total absorption band strength for the band of interest (for CO, $S = 250 \text{ atm}^{-1} \text{ cm}^{-2}$), R is the ratio of the total gas density to the total gas density at NTP, f is the ratio of the partial pressure of the gas of interest to the total gas pressure in the cell, and ν_{0J} is the position of the line center in wavenumbers.

Because the linewidths in the two cells, δ_1 and δ_2 , vary with time and usually are not equal, it is not possible to calculate the heterodyne signal analytically. Some orientation can be gained, however, by looking at the equation developed in the introduction for absorption at a single frequency (wavelength) within a single absorption line.

Let A_1 and A_2 be defined such that

$$A_1 \equiv \mu_{01} x_1 \rho_{01} \quad \text{and} \quad A_2 \equiv \mu_{02} x_2 \rho_{02} \quad (8)$$

If the definitions of A_1 and A_2 are compared with Eqs. (5) and (6), one sees that Eq. (6) can be rewritten as

$$\left(\frac{I_\lambda}{I_{0\lambda}} \right)_{\omega_1 - \omega_2} = e^{-(A_1 + A_2) \frac{1}{2} A_1 A_2} \left(\frac{\Delta \rho_1}{\rho_{01}} \right) \cdot \left(\frac{\Delta \rho_2}{\rho_{02}} \right) \cos(\omega_1 - \omega_2) \quad (9)$$

One cannot freely choose the value of A_2 since it is proportional to the small amount of trace gas to be measured. However, since A_1 (defined as $\mu_{01} x_1 \rho_{01}$) is proportional to the length of cell 1, the strength of the absorption band at this wavelength and the partial pressure of the absorber gas in the reference cell (cell 1), A_1 can be selected to optimize the performance. Taking the derivative of Eq. (6) with respect to A_1 and setting that derivative equal to zero, one finds that for maximum signal, the partial pressure of absorbing gas in cell 1 should be that pressure necessary to make $A_1 \sim 1$, i.e., the average reduction of the light in cell 1 is e^{-1} . Less absorption would reduce the modulation signal due to chamber 1 while more absorption would reduce the amount of light reaching chamber 2 to be modulated there. The amount of light needed can be roughly estimated by considering that, for typical gases such as

CO and for path lengths of several centimeters in cell 1, the partial pressure required to make $A_1 \approx 1$ near the center of the stronger lines amounts to a few torr.

A second factor to be considered is the effect of emissions from the gas of interest. The spontaneous emission from the (thermally populated) upper level of the vibration-rotation band of interest is also a function of temperature. This emission could cause a spurious signal 180° out of phase with the absorption signal, but only when the much larger absorption signal is present. The effect of the emission signal, then, is to slightly reduce the sensitivity of the system. The relative magnitude of the signals is seen by realizing that the radiation from an optically thin gas at a temperature of 300°K is being compared with the radiation from an incandescent black-body source at several thousand degrees. For all practical purposes, then, the self-emission from the gas can be ignored.

The third and most complex factor to evaluate is related to the elimination of the simplifying assumptions made in the previous sections. While the analysis has assumed the absorption occurs at discrete lines, in air at NTP these lines have linewidths of the order of 0.1 cm^{-1} . The bulk of this width is due to Lorentz or collision broadening. Most of the collisions experienced by the trace molecules will be with air molecules rather than with like molecules or those of other trace gases. The rate of collisions will be roughly proportional to the total gas density and the average molecular velocity, itself proportional to the square root of the temperature. The width of the line is proportional to this collision rate so that one can write for δ , the halfwidth at halfheight,

$$\delta = \delta_0 \left(\frac{\rho}{\rho_0} \right) \left(\frac{T}{T_0} \right)^{1/2} \quad (10)$$

If the density of the gas is sinusoidally varied about a mean value then temperature, population of the various rotational states, linewidths, absorption, and spontaneous emission will also vary. In each cell the temperatures will be determined by the characteristics of the major constituents present (probably helium or other inert gas in the reference cell, air in the sample cell).

Using familiar gas equations,

$$PV = RT$$

$$PV^\gamma = \text{constant}$$

$$T = \frac{PV}{R} = T_0 \left(\frac{V}{V_0} \right)^{1-\gamma} = T_0 \left(\frac{\rho}{\rho_0} \right)^{\gamma-1}$$

Combining Eq. (10) and Eq. (13) yields

$$\delta = \delta_0 \left(\frac{\rho}{\rho_0} \right)^{\frac{\gamma+1}{2}}$$

The distribution of population among rotational states is approximately given by

$$N_J = \frac{NB}{kT} (2J + 1) \exp \left[\frac{-BJ(J + 1)}{kT} \right] \quad (15)$$

where N is the total population of all the rotational states. Since N_J is a function of temperature, it is, like linewidth, also a function of density.

The heterodyning process in the gas is complex. The optimum rejection of spurious signals is obtained when the absorption spectrum introduced by the reference cell exactly matches the absorption spectrum of the gas sought after in the sample cell. Yet each line absorbed varies in its shape and in its peak height due to the temperature and density variations at the frequency of the density modulation; the relative peak intensities of the various absorption lines in the spectrum vary as a result of the temperature variations; and the temperature and density dependent signatures of the reference and sample cells vary at different frequencies and through different amplitudes. Not unexpectedly, the solution of the heterodyning interaction is theoretically intractable. A computer analysis is in process, however, and will be used to provide more exact analytical results for several gases of interest.

Experimental Evaluation

The experimental apparatus used to investigate the heterodyne detection method of NDIR gas analysis is shown in Fig. 2. Infrared radiation from a blackbody source was passed through a pair of pressure modulated cells, an interference filter, and a light collector to a PbSe photoconductive infrared detector. An interference filter was used to restrict the infrared radiation seen by the detector to the region of the absorption band of the gas of interest. The reference and sample cells, which contained gas mixtures at a total pressure of 1 atm, were pressure modulated by means of University Sound I.D. 60 acoustic drivers at angular frequencies of $\omega_1 = 3000$ and $\omega_2 = 4800$, respectively. Under resonant conditions, the total pressure modulation in the cells obtainable with this technique was up to 30% of an atmosphere. The signal from the PbSe detector was amplified and passed through a high pass filter (with a roll-off of 48 dB per octave from $\omega = 5400$) to a Quantech Wave Analyzer that measured the signal at the heterodyne frequency of $\omega_1 + \omega_2 = 7800$ with a bandpass width of 1 Hz. The geometrical arrangement of blackbody source, light collector, and detector ensured that infrared energy reflected from the chopper and sample cell walls had very little chance of reaching the detector. This feature was very beneficial in that when both cells were filled with an infrared neutral gas such as dry N_2 the background detector signals obtained at ω_1 , ω_2 and $\omega_1 + \omega_2$ were negligibly small compared to those obtained when infrared active gases in the cells were unencumbered by background effects from cell wall reflections.

Threshold sensitivities of the heterodyne technique for the gases CO_2 , CO , and N_2O have been measured for 2 cm-long reference and sample cells, and have been found to be 0.2, 4, and 0.4 ppm for each gas, respectively. In addition, lower limits to the cross

sensitivity of each of these gases for the other two gases have been established. It has been verified that large improvements in the rejection ratio can be gained with the use of gas negative filters, for those examples of gases having strong overlap in their absorption bands (in this case, CO and N_2O).

A summary of the results is given in Figure 6.

The experimental conditions under which these results have been obtained are:

1. Sample and chopper cells 2 cm long
2. Total pressure excursions of 20% atm and 30% atm in the sample and chopper cells, respectively
3. Operation of the blackbody source at a power level of 2 W (corresponding to less than a quarter of the maximum at which it can be operated)
4. An integrating time constant of 10 sec.

A serious limitation of the present apparatus is the nonlinearity of the thermoelectrically cooled PbSe detector and its preamplifier. For example this nonlinearity results in a large heterodyne signal when the sample and chopper cells are filled with CO_2 and N_2O , respectively, since these gases produce large modulation of the infrared radiation. For the detector and electronics used, this corresponds to an apparent rejection ratio of 500:1, when in fact the absorption spectra of these two gases near 4.3 μM have only a very small overlap and the rejection ratio must be quite large. This emphasizes the need for linearity in the detector and electronics if an instrument is to be insensitive to the presence of large quantities of gases having absorption bands within the passband of the interference filter.

A related problem is the large decrease in responsivity of the present detector as the light flux is increased. For example, by raising the temperature of the blackbody source above that currently used, the radiation intensity can be raised fourfold. With the present detector biasing arrangement, however, the responsivity drops by a factor of about four, and the detector becomes considerably more nonlinear. Hence, the present measurements have been performed at a reduced incident flux level of 1 W/cm².

One can expect, therefore, that a factor of four improvement in gas sensitivity is possible with the present arrangement by designing the detector circuitry to retain its responsivity at high incident light flux levels. A further gain by a factor of about two in gas sensitivity can readily be obtained by rearranging the geometry of the gas cells to yield a higher pressure excursion in the chopper cell, and an additional factor of five can be obtained by providing a longer absorption path for the same pressure variation in the sample cell. These yield a potential gain of a factor of 40 in threshold sensitivity.

It can be seen from the results summarized in Figure 6 and the improvements to the present apparatus noted above that the understanding of the problems associated

with the heterodyne technique at present indicates that sensitivity of the order of 0.01 ppm for gases with strong infrared absorption bands such as CO_2 , N_2O , SO_2 , and NO_2 should be obtainable. For the weaker infrared absorbers such as CO , NO , and H_2S detection of 0.1 ppm should be feasible.

"Field" Instrument

Based on the success of the preliminary analytical and experimental work, an instrument was designed to serve the dual purposes of facilitating further experiments and of providing a prototype of a field instrument. Three basic changes were considered desirable and have been incorporated in the new instrument (Fig. 3 and 4). First, the optical system was modified to accommodate a longer pathlength in the sample cell (thereby providing greater sensitivity for trace concentrations) and to provide space for several static absorption cells to contain gases used as filters (thereby allowing the reduction of the undesirable sensitivity to unwanted gases in special cases); second, the techniques used to provide density modulation were improved to allow a greater fractional modulation, to provide a controlled level of modulation and to provide "self-tuning" of the driver to the acoustic resonance of the Helmholtz resonators (thereby reducing changes in instrument performance with temperature); and third, the electronics were modified to provide phase-sensitive detection, locking the detection frequency to the (variable) difference between the drive frequencies of the reference and sample cell modulations (thereby avoiding "beat frequency" effects resulting from drifts in the relative frequencies of the spectrum analyzer and the Helmholtz modulator).

Increasing the optical pathlength of the instrument by simply stretching the optical system used in the experimental setup of Fig. 2 suffers from the disadvantage that the amount of light reaching the detector is reduced, causing the signal to be reduced accordingly. Since this is clearly undesirable, the optical system was modified to include relay lenses (Fig. 5).

The optical train is made up of a number of discrete components, with alignment of the sections assured by a matching land-groove system machined into the faces of the elements. The faces have a 5 cm-square cross section with bolts at each corner. Each section is gas tight and may be filled with an inert gas if desired. O-ring seals are used throughout. Sapphire windows are used to seal the reference and sample cells. The entire optical train is designed to afford maximum interchangeability and versatility while still remaining rigid.

The system is designed to prevent any of the detected radiation from being reflected from the container walls, to form an out-of-focus image of the diffuse light sources at the plane of the detector, and to insure that the image overfills the sensitive area of the detector. Slight variations in the optical geometry induced by vibrations of the system thereby cause a slight shifting of the source image relative to the detector. Since, however, the source is an extended area source, and the image is out of focus, the effect on the intensity of the detected light should be very small.

The changes required to effect the desired mechanical modifications in the Helmholtz resonator involved the sealing of volumes and port dimensions, redesign of the matching section that couples the resonator to the audio driver, and modification of the electronics to allow closed-loop operation controlled by the measured pressure in the resonator. The mechanical changes are fairly straightforward and need not be detailed here.

The electronic systems for energizing the Helmholtz chambers are shown in Fig. 8, along with the detection circuits. Each Helmholtz circuit contains a resonator, a power amplifier, an acoustic driver, a pressure sensor, and amplitude control circuitry connected in a positive feedback loop to cause sustained oscillations at the resonant frequency of the Helmholtz chamber. The difference between the amplitude of oscillation and a predetermined level produces an error signal that controls the resistance of an FET in an AGC loop to maintain a constant amplitude. Any of three levels of oscillation may be selected with a front panel switch.

The detection system in the new instrument consists of a thermoelectrically-cooled lead selenide detector, a low noise preamplifier, two phase-sensitive detectors (PSDs) to recover the $(\omega_1 - \omega_2)$ and ω_1 signals, and a divider to provide the normalized output $I_{\omega_1 - \omega_2} / I_{\omega_1}$ to drive the output meter. The detector is cooled by a Peltier device with a thermistor in a feedback loop to hold the temperature at -22°C with less than 0.1°C variation.

The reference signals for the PSDs are obtained directly from transducers measuring the pressure in the Helmholtz resonators, but obtaining the $(\omega_1 - \omega_2)$ reference requires additional circuitry. Defining the ω_1 and ω_2 signals as $\sin \omega_1 t$ and $\sin \omega_2 t$, $-\cos \omega_1 t$ and $-\cos \omega_2 t$ are derived from unity gain, frequency independent, 90° phase shift networks. $\sin \omega_1 t$ is multiplied by $\sin \omega_2 t$ and $-\cos \omega_1 t$ is multiplied by $-\cos \omega_2 t$ to give:

$$\sin \omega_1 t \sin \omega_2 t = \frac{1}{2} [\cos(\omega_1 - \omega_2)t - \cos(\omega_1 + \omega_2)t] \quad (16)$$

and

$$(-\cos \omega_1 t)(-\cos \omega_2 t) = \frac{1}{2} [\cos(\omega_1 - \omega_2)t + \cos(\omega_1 + \omega_2)t] \quad (17)$$

Equations (16) and (17) are added to obtain a signal, $\cos(\omega_1 - \omega_2)t$, which is used as a reference for the $(\omega_1 - \omega_2)$ PSD.

Because of nonlinearity in the multipliers used to perform the functions of Eqs. (16) and (17), the $\cos(\omega_1 - \omega_2)t$ reference signal is fed through a 48 dB/octave, 200 Hz, low-pass filter to remove frequencies other than $\cos(\omega_1 - \omega_2)t$. The complex signal from the preamplifier is fed through an identical filter prior to feeding its PSD to retain correct phasing of the $(\omega_1 - \omega_2)$ signal should ω_1 or ω_2 change with temperature or time or in case the filter following the multiplier change phase with temperature. The outputs of the PSDs are dc signals proportional to the I_{ω_1} and $I_{(\omega_1 - \omega_2)}$ signals in

the detector. These dc signals are smoothed with a 3-sec time constant and fed to an analog divider whose output drives a meter to indicate $I_{\omega_1 - \omega_2} / I_{\omega_1}$.

Figures 8 through 16 are detailed circuit diagrams of the individual blocks on Fig. 7.

Conclusions

The effectiveness of the Heterodyne-NDIR technique for measuring trace quantities of gases has been demonstrated by laboratory tests using an absorption cell length of only 2 cm. Increased absorption cell length and other improvements incorporated in a prototype

field instrument should provide the ability to detect the presence of any gas with a molecular vibrational-rotational spectrum with sensitivities in some cases as high as five to 10 parts per billion. Rejection of spurious readings introduced by interfering gases is better than that of many instruments and may be significantly improved by reducing detector nonlinearity by electronic means or by use of negative gas filters in the optical path.

The Heterodyne-NDIR detection method appears to have great promise and general applicability in trace gas analysis, and in developed form it should prove to be a major new tool for gas analysis.

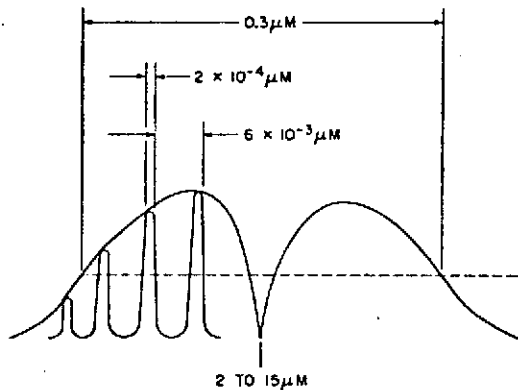


FIGURE 1. TYPICAL VIBRATIONAL ROTATIONAL BAND

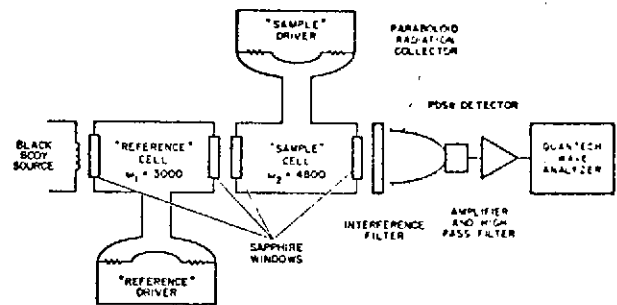


FIGURE 2. EXPERIMENTAL ARRANGEMENT

Reproduced from best available copy.

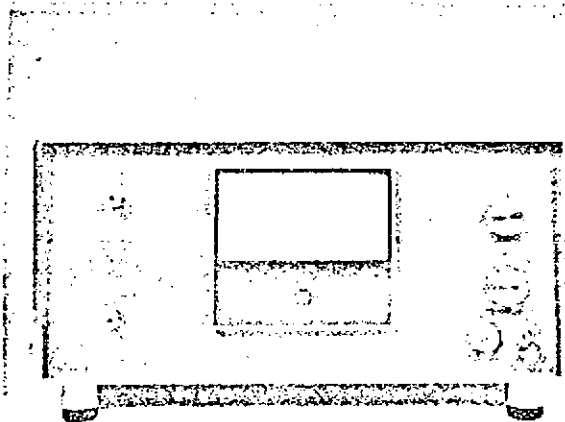


FIGURE 3. FIELD INSTRUMENT - EXTERNAL VIEW

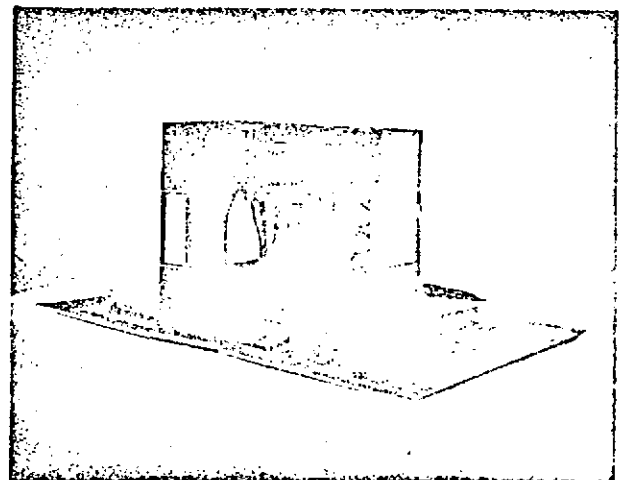


FIGURE 4. FIELD INSTRUMENT - INTERIOR VIEW

A 6

C-2

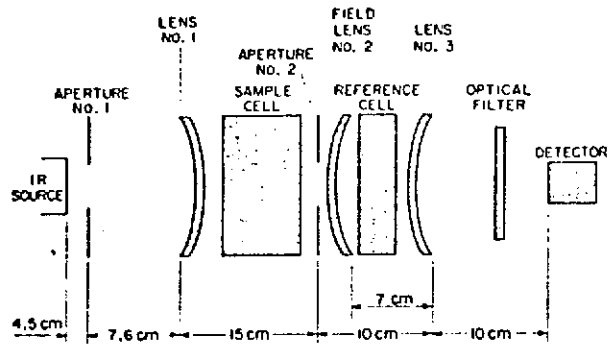


FIGURE 5. OPTICAL SYSTEM

GAS	THRESHOLD SENSITIVITY	GAS FILTER	REJECTION RATIOS (LOWER LIMIT)	
			CO	N ₂ O
CO ₂	0.2 ppm	1 atm cm OF CO	>500:1*	>1500:1*
	0.2 ppm	1 atm cm OF N ₂ O	PROBABLY > 15,000:1	>15,000:1
CO	4 ppm	1 atm cm OF N ₂ O	15:1 FOR u = 0.1	CO ₂
	7 ppm		2.5:1 FOR u = 0.002	
	4 ppm	1 atm cm OF CO ₂	70:1 FOR u = 0.1	>5000:1*
N ₂ O	0.4 ppm	1 atm cm OF CO	50:1* FOR u = 0.006	CO
	0.4 ppm		>500:1* FOR u = 0.006	CO ₂
	0.4 ppm		1 atm cm OF CO ₂	>5000:1*

*1 atm cm OF GAS
 *THESE VALUES ACTUALLY REPRESENT DETERMINING OF THE RADIATION IN THE DETECTOR AND PREAMPLIFIER DUE TO THEIR NON-LINEARITY.
 **THRESHOLD SENSITIVITY IS HERE DEFINED AS THE NUMBER OF PPM OF GAS WHICH PRODUCES A METEORING SIGNAL EQUAL TO THE RMS VALUE OF THE VARIATION OF THE DETECTOR/PREAMPLIFIER'S NOISE AT THE METEORING FREQUENCY.
 ***NOTE THAT THE FILTER USED IN THESE MEASUREMENTS TRANSMITS ONLY ONE BRANCH OF N₂O.

FIGURE 6. SUMMARY OF EXPERIMENTAL DATA

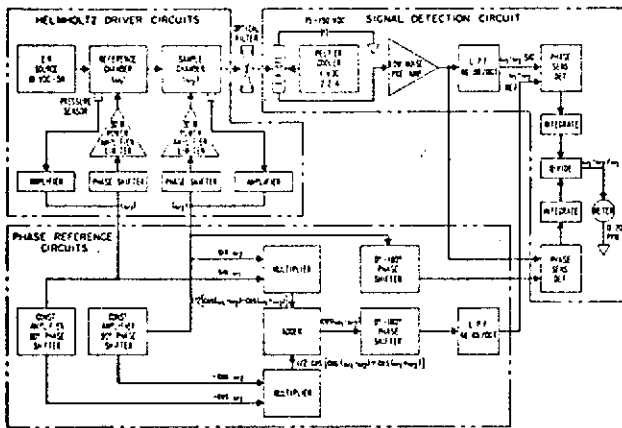


FIGURE 7. SYSTEM BLOCK DIAGRAM

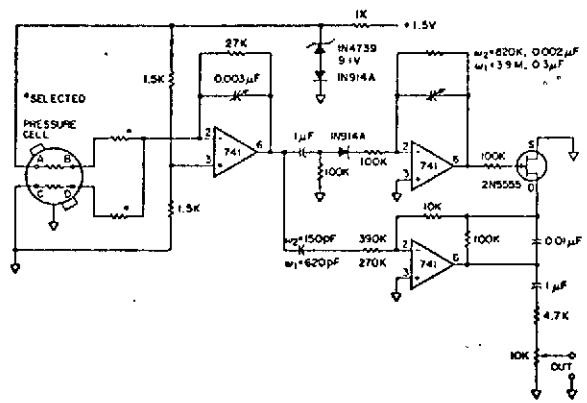


FIGURE 8. PRESSURE AMPLITUDE CONTROL

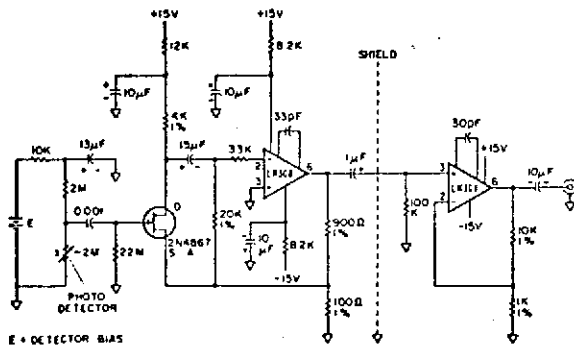


FIGURE 9. PREAMPLIFIER

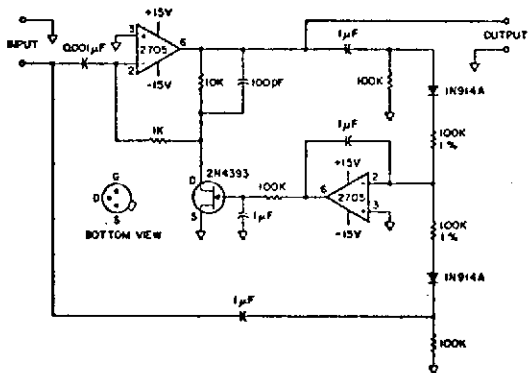


FIGURE 10. CONSTANT AMPLITUDE 90° PHASE SHIFT

A?

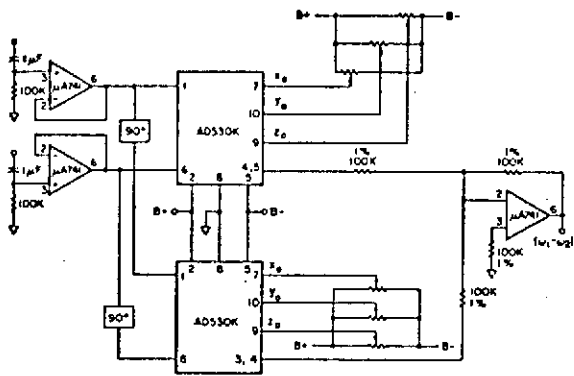


FIGURE 11. REFERENCE SIGNAL GENERATOR
($\omega_1 - \omega_2$)

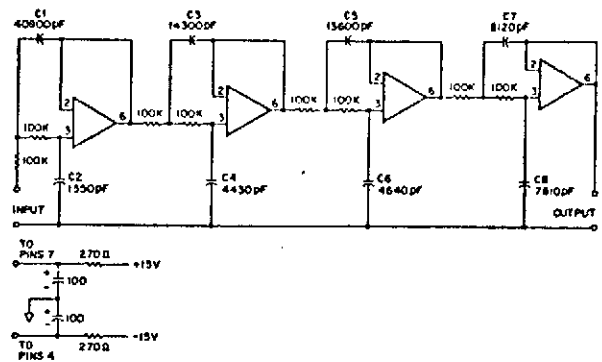


FIGURE 12. LOW PASS FILTER

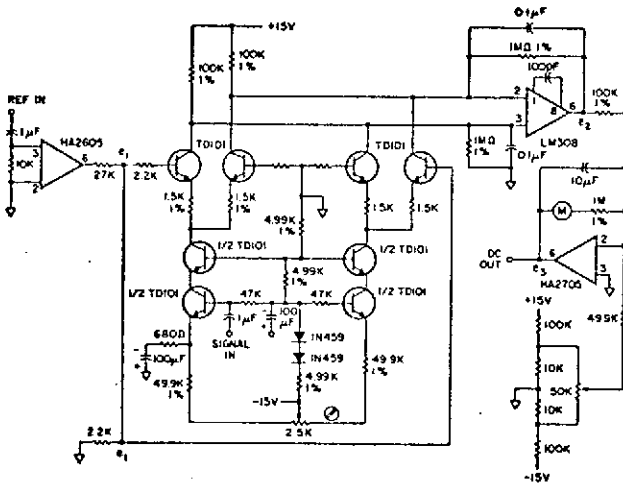


FIGURE 13. PHASE SENSITIVE DETECTOR

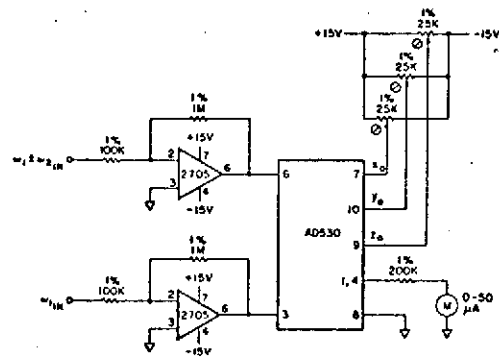


FIGURE 14. OUTPUT DIVIDER

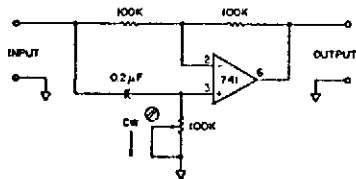


FIGURE 15. 0-180° CONSTANT AMPLITUDE
PHASE SHIFTER

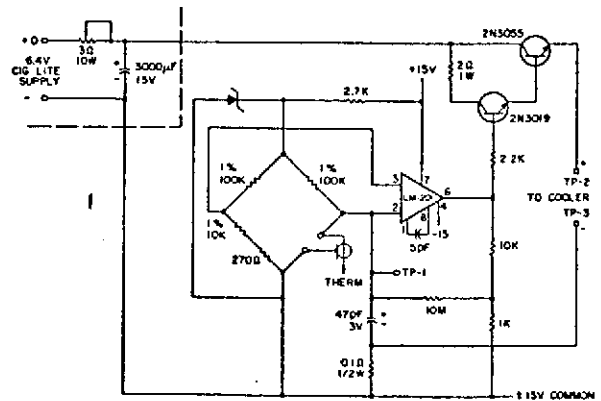


FIGURE 16. THERMOELECTRIC COOLER
CONTROL CIRCUIT

A₈

APPENDIX B

MINIATURE HELMHOLTZ RESONATOR STUDY

APPENDIX B

MINIATURE HELMHOLTZ RESONATOR STUDY

INTRODUCTION

The objective of this phase of the program was to develop Helmholtz resonator systems of reduced size, compared to the large and heavy resonators fitted to the 3-gas heterodyne demonstration instrument. The basic plan was as follows:

1. Investigate fundamental Helmholtz theory.
2. Build and test models to check compliance to basic Helmholtz theory.
3. Build and test resonators similar in concept to existing art, but with some parameter variable.
4. Use knowledge thus gained to build a first-generation miniature device.
5. Iteratively develop as required to converge on the objective, to the extent permitted by budget constraints.

BASIC HELMHOLTZ THEORY

The classical Helmholtz resonator consists of a thin-shelled sphere (Figure 1) with a circular aperture. Such a cavity exhibits a natural resonance of wavelength λ when excited. This natural resonance is given by

$$(1)^1 \quad \lambda = 2 R \left(\frac{2 R}{3a} \right)^{1/2} \left(\frac{1 - 0.14324a}{R + 0.08455 \frac{a}{R^2}} \right)^{1/2}$$

where a and R are as shown in Figure 1.

¹ Harold Levine, J. of Acoustical Society of Amer., Vol. 23 No. 3, May, 1951, p. 307-311.

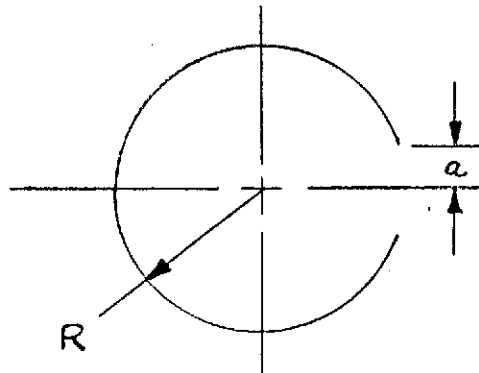


Figure 1

The second term in parentheses is a correction factor for turbulence effects and non-infinite particle velocity at the aperture edge. With $R = 1.5$ inch and $a = 0.25$ inch, this correction is -3.6%.

The Levine Theory assumes that the length of the aperture is zero. A more realistic and general relationship which allows for aperture length is (Refer also to Figure 2)

$$(2)^2 \quad f_o = \frac{c}{2\pi} \left[\frac{A}{V(1 + \delta)} \right]^{1/2}$$

where A is the aperture area,
l the aperture length,
V the cavity volume,
 δ the aperture "mass end correction",
given by (3) and (4) below, and
c the velocity of sound.

² Condon, Handbook of Physics, 2nd edition, p. 3-125 etc.

$$(3)^2 \quad \delta_o = \frac{16a}{3\pi}$$

where a is the aperture radius. This formula assumes the aperture radius is small relative to cavity dimensions.

$$(4)^2 \quad \delta \approx 0.96A^{1/2} \text{ for arbitrary aperture.}$$

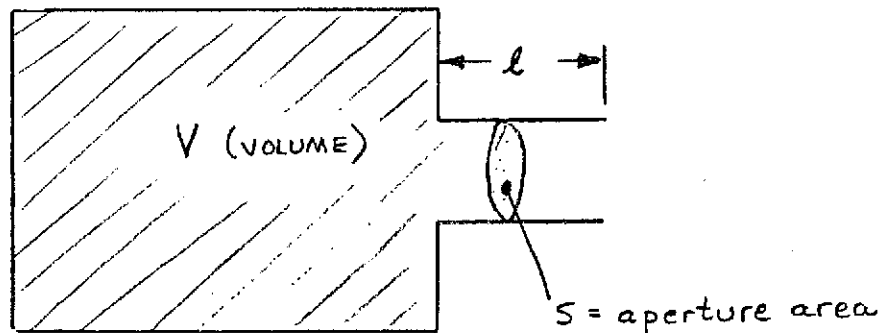


Figure 2

The basic (ideal) form of equation (2) is

$$(5)^3 \quad f_o = \frac{c}{2\pi} \frac{A}{Vl}^{1/2}$$

(5) has the same form as that for the natural frequency of an electric LC tank circuit:

$$(6) \quad f = \frac{1}{2\pi} \frac{1}{LC}^{1/2}$$

The lumped-constant parameters L and C can be interpreted as analogous to acoustical properties:

$$(7)^3 \quad C \propto \frac{V}{\gamma P} \quad \text{where } \gamma \text{ is the ratio of specific heats and } P \text{ is the absolute pressure}$$

$$(8)^3 \quad L \propto \frac{\rho l}{A} \quad \text{where } \rho \text{ is the gas density.}$$

³ Reportedly from one of the books by P.M. Morse, title unknown

With the aid of the well-known relationship for the velocity of sound,

$$(9) \quad \rho C^2 = \gamma P,$$

relations (6) through (8) may be manipulated to yield (5). (2) is the same as (5) with an aperture correction added.

R & D PROGRAM

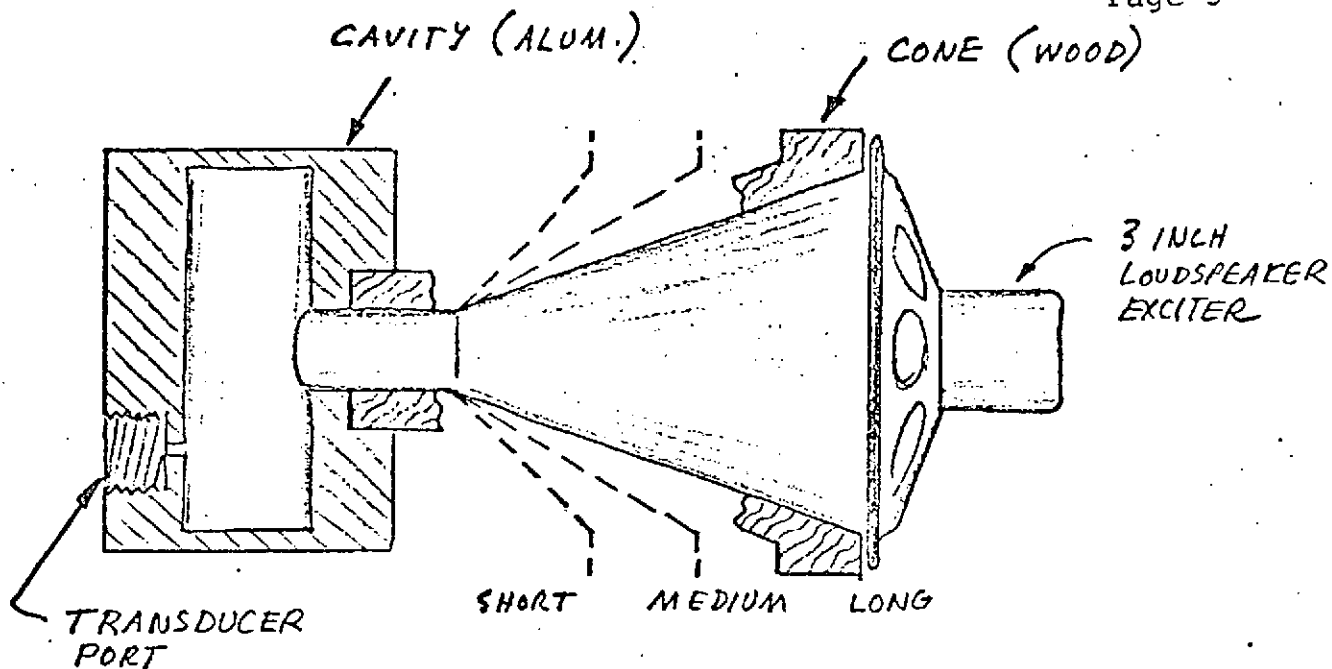
Our first experimental effort sought to find the nature and extent of performance differences produced by varying one of the geometric parameters of the cone-neck-cavity configuration as used in the heterodyne demonstration model. In particular, the length (and hence angle) of the cone section was varied. This apparatus is depicted by Figure 3. Excitation was by a small cone-type loudspeaker, open at the rear. The speaker, cone, and cavity were held together with a strap arrangement.

Tests of this and most other apparatus were conducted with the setup of Figure 4.

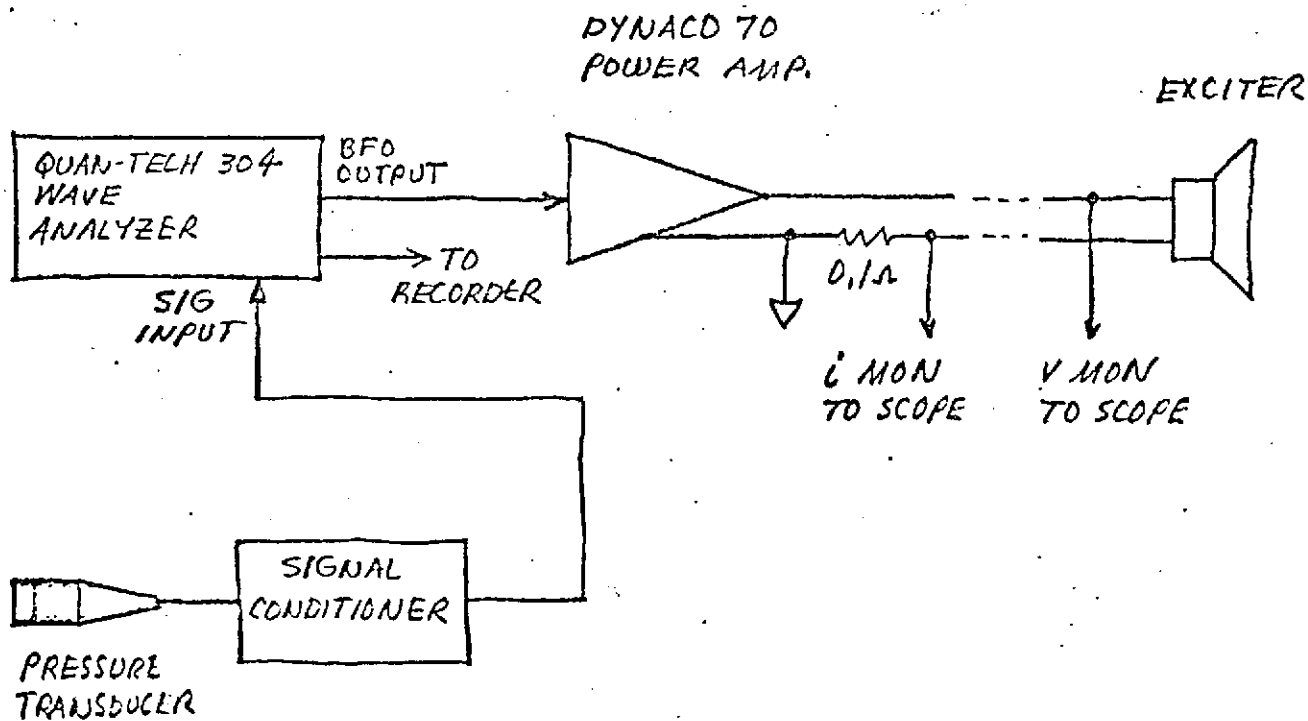
The variable-cone apparatus yielded poor and inconclusive results. In all cases, there were two resonances, both weak. Attempts to mathematically predict the resonant points were frustrated by the ill-defined boundaries between lumped-constant regions--if, indeed, such regions existed at all--and by uncertainty as to what was happening in the system or how to model it.

Further attempts to evaluate these cones were abandoned and refuge was sought in the construction of an apparatus that more closely approached a lumped-constant ideal. This is shown in Figure 5.

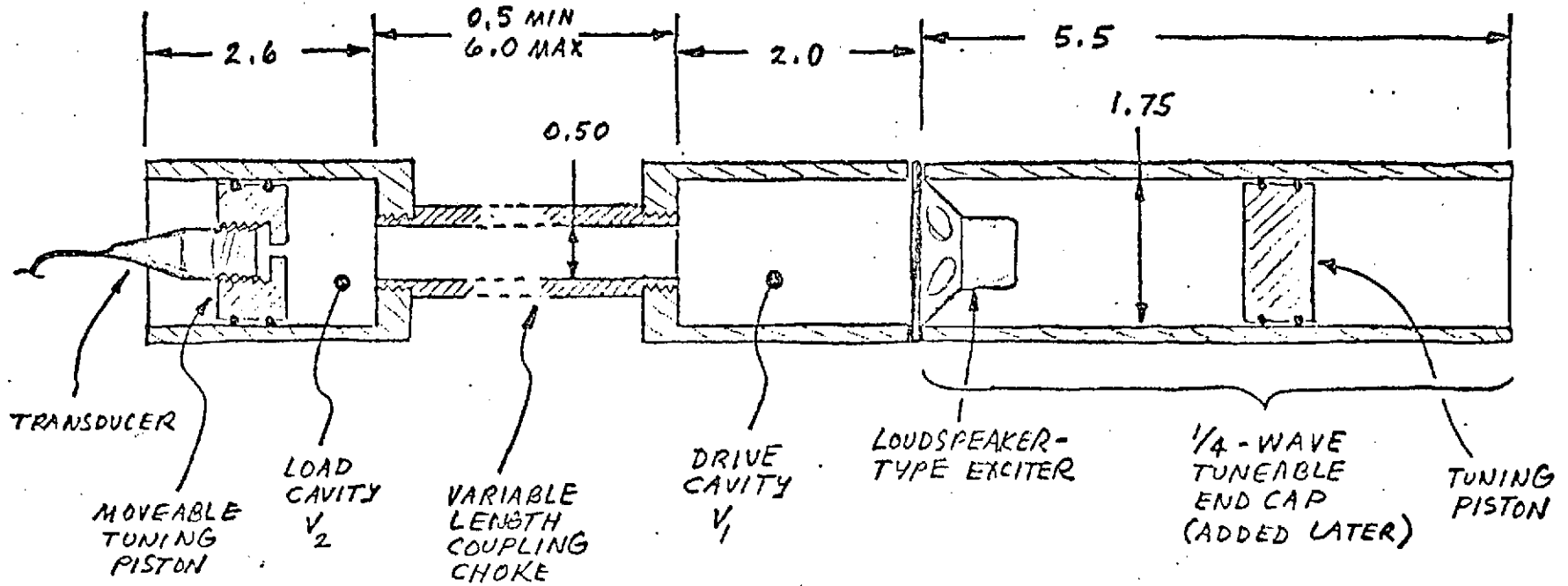
The first test with the Figure 5 setup was done using just the drive cavity and choke as shown in Figure 6. The 1/4-wave cap



- FIG 3 -
VARIABLE CONE APPARATUS



- FIG 4 -
TYPICAL TEST SETUP



- NOTES: 1. PISTONS SEALED WITH O-RINGS & VACUUM GREASE
 2. CAVITIES CONSTRUCTED OF LUCITE STOCK; CHOKE IS ALUMINUM
 3. DIMENSIONS ARE INCHES

- FIG 5 -
 LUMPED-CONSTANT APPARATUS

was not yet fitted. Design of the apparatus permitted easy disassembly of parts and variation of choke length via threaded joints, couplings, and adapters.

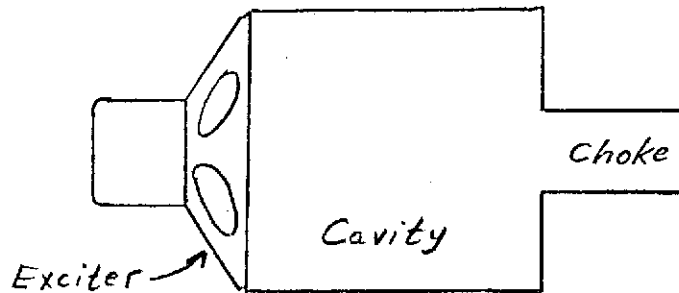


Figure 6

Formulas (2) and (4) were used to compute the frequency of response. The results are tabulated in Table 1 below. Frequency f_1 is the stronger resonance, f_2 the weaker.

TABLE 1

- Notes: 1. All dimensions in inches.
2. All pressure excursions 0.1 psia-pp.

<u>Line</u>	<u>A</u>	<u>l</u>	<u>V</u>	<u>f_o</u> (computed)	<u>f_1</u> (strong)	<u>f_2</u> (weak)
1	0.31	0.25	4.98	627	948	--
2	0.196	0.50	4.98	433	831	428
3	0.196	1.1	4.98	336	778	367
4	0.196	2.75	4.98	233	723	--
5	0.196	4.63	4.98	185	704	--
6	--	closed	4.98	--	702	--

Presence of the strong resonance f_1 at frequencies much higher than predicted is not explained. The closed test (line 6, Table 1) gave 702 Hz although standing-wave behavior would indicate 1571 Hz for a quarter-wave of 2.1 inches.

The next test was performed in the configuration of Figure 5 but without the 1/4-wave cap. These data are tabulated in Table 2.

Before commenting on these results, some explanation is in order for the term v' in Table 2.

When the apparatus shown in Figure 6 was conceived, it was erroneously believed the two cavities had to be the same volume. Indeed, the piston's function was to precisely equalize the volumes. It was thus surprising that a resonance could be found no matter where the piston was set, and it immediately became clear that we had the acoustic equivalent of an electrical pi-network, modeled as in Figure 7.

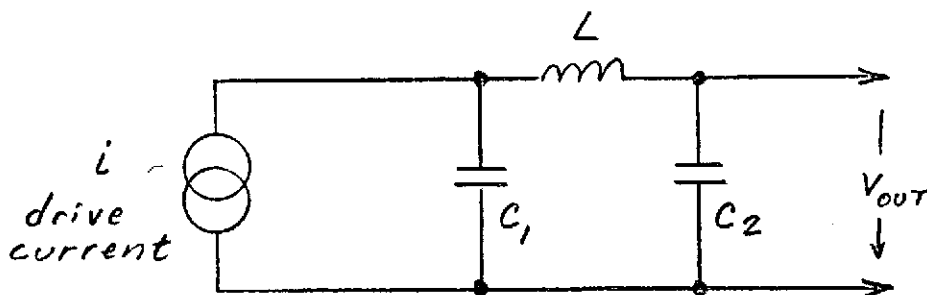


Figure 7. Electrical Model of Resonator

The transfer function of this network is, in Laplace terminology,

$$(10) \quad \frac{V_2(s)}{i_o(s)} = \frac{C_2}{s^2 [(C_1 + C_2) + s^2 LC_1 C_2]}$$

TABLE 2

A = 0.196, in all cases

Line	<u>l</u>	Load Cavity Length	<u>v'</u>	f_o (computed)	f_1 (measured)	$\frac{f_1}{f_o}$	<u>Q</u>	Voltage <u>V_{PP}</u>	Current <u>mA PP</u>	psi <u>p-p</u>
1	0.5	2.0	2.45	612	594	1.032	5.6	--	29	--
2	0.5	1.0	1.62	752	645	1.166	--	--	--	--
3	0.5	0.5	0.969	972	671	1.45	--	--	--	--
4	2.75	2.0	2.45	333	368	1.105	9.2	--	55	0.044
5	2.75	1.0	1.62	409	455	1.112	10.8	--	50	0.088
6	2.75	0.5	0.969	529	551	1.042	7.8	--	--	0.112
7	2.75	0.62	1.147	486	526	1.082	10.5	--	40	0.112
8	2.75	0.75	1.324	453	502	1.108	11.1	--	--	0.110
9	2.75	0.88	1.487	427	479	1.12	10.9	--	--	0.100
10	2.75	0.75	1.324	453	499	1.102	8.3	5.7	450	1.00
11	4.62	0.75	1.324	359	380	1.058	12.1	1.15	135	0.100
12	4.62	0.75	1.324	359	380	1.058	9.04	14.0	1500	1.00

B
9

The roots of this correspond to the natural frequencies:

$$(11a) \quad s_1 = s_2 = 0$$

$$(11b) \quad s_{3,4} = \pm j \left(\frac{C_1 + C_2}{LC_1 C_2} \right)^{1/2}, \text{ or}$$

$$(11c) \quad f_o = \frac{1}{2\pi} \left(\frac{C_1 + C_2}{LC_1 C_2} \right)^{1/2}$$

The acoustic analogs for the C's and L's are given in (7) and (8), respectively.

Inspection of (11c) shows it to be similar to the familiar LC resonance equation

$$(12) \quad f_o = \frac{1}{2\pi} \left(\frac{1}{LC} \right)^{1/2}$$

wherein

$$(13) \quad C = \frac{C_1 C_2}{C_1 + C_2}.$$

This, of course, is just the net value of two series capacitors. Consequently, we see that the two acoustic cavities must act as though they were one, of volume

$$(14) \quad v' = \frac{V_1 V_2}{V_1 + V_2}.$$

This is the V' used in Table 2.

Analysis of the data of Table 2 reveals the following:

1. All calculated frequencies are too low, the error ranging from 3.2% to 45%, depending on the configuration.

2. The error becomes lower as the choke becomes longer.
3. Compliance to the "series" cavity criteria of (14) is excellent insofar as the ratios of frequencies are concerned.
4. Q's improved with longer chokes. This could be explained either by
 - a. assuming the ratio of the imaginary to real parts of the choke impedance improves as length increases (on the basis of fixed end losses) and/or
 - b. assuming the resulting lower frequencies per se involve lower losses.
5. At constant exciter drive level, the pressure obtained increased as the load cavity was decreased.
6. Q tended to be poorer at higher pressure levels.
7. There was a complete absence of doubly resonant behavior at all configurations in Table 2.

The most significant outcome from this experiment was realization of the method of using the ratio between the drive and load cavity volumes as a pressure amplifying or impedance matching mechanism. Of course, the use of pi-networks for analogous purposes in electric circuits, especially in radio circuits, is a well-established technique.

Limitations of this apparatus include marginal cone travel and power handling ability of the exciter, and the extravagant emissions of acoustical energy to the rear. To overcome the former, one could design a special cone exciter and/or adjust the cavity ratios for optimum matching. To overcome the latter, one could use a closed compression-driver (limited to frequencies above 1 Khz) or enclose the exciter rear with sound inerting or a 1/4-wave cap. With smaller geometry hardware, a compression-driver may be satisfactory, but note that it cannot be properly loaded so will not yield its efficiency potential.

CONCLUSIONS AND RECOMMENDATIONS

1. Two-cavity resonators were demonstrated, with reasonable conformance to theory, to represent a viable configuration in lumped-constant resonators of reduced bulk and mass.
2. The use of double cavities to match impedances or amplify pressure has been shown theoretically and experimentally.
3. The 1/4-wave cap is a possible method of controlling noise emission and simultaneously reducing drive power and enhancing Q.
4. Efficacy of cone-shaped cavities or necks is not established. Our feeling at this time is that best performance will be realized with spheroidal, oblately spheroidal or ellipsoidal cavities coupled via short necks joined by properly faired intersections.
5. Exciter self-resonance effects, free-air and in situ, are important and should be further evaluated.
6. Optimum type exciter is not firmly established but a high compliance, long-throw piston-type device is indicated as preferable to compression driver, although the latter might excel at smaller geometrics.
7. Streaming and turbulence are important at high amplitude, but much more investigation is necessary.
8. Substantial further miniaturization appears entirely feasible, provided that considerations such as exciter resonance and loss mechanisms are properly dealt with; i.e., we see no fundamental barriers. Shape optimization will obviously be of paramount importance in very small systems.